MRO Delay Line

Results of the Risk Reduction Experiments

Roger Boysen, David Buscher, Martin Fisher, Chris Haniff, Bodie Seneta, Peter Warner, Donald Wilson & John Young

Revision 1.0, July 15, 2005

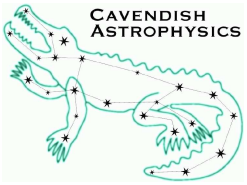

Cavendish Laboratory
Madingley Road
Cambridge CB3 0HE
UK

Contents

1 Introduction and derived requirements **1**

1.1 Background . . . 1

1.2 Scope . . . 2

1.3 Vacuum system derived requirements . . . 2

1.3.1 Dispersion . . . 2

1.3.2 Wavefront errors . . . 3

1.3.3 Thermal conductivity . . . 5

1.4 Catseye optical analysis . . . 5

1.4.1 Design overview . . . 5

1.4.2 Relevant requirements . . . 5

1.4.3 Effect of catseye defocus . . . 6

1.5 Effects of catseye rotation and translation . . . 7

1.5.1 Effect of tilting the secondary mirror . . . 7

1.5.2 Summary error budget . . . 8

2 [002-01] Pipe Coupling Scheme **9**

2.1 Aim . . . 9

2.2 Method . . . 9

2.3 Tests . . . 10

2.3.1 Ease of assembly . . . 10

2.3.2 Mechanical alignment of the trolley wheel tracks . . . 10

2.3.3 Vacuum Integrity . . . 11

2.3.4 Electrical Continuity . . . 12

2.4 Conclusions . . . 12

3 [002-02] Pipe Support **13**
3.1 Aim . . . 13
3.2 Support Design . . . 13
3.2.1 Support Installation . . . 16
3.3 Vibration modelling and tests . . . 16
3.3.1 FEA model . . . 16
3.3.2 Vibration test method . . . 16
3.3.3 Vibration test results . . . 18
3.3.4 Effect of moving trolley on pipe vibration . . . 20
3.4 Extension of model to 200 m . . . 21
3.5 Conclusions . . . 23

4 [002-03] Carriage Trajectory **25**
4.1 Aim . . . 25
4.2 Method . . . 25
4.2.1 Description of apparatus . . . 25
4.2.2 Experimental Procedure . . . 28
4.3 Definition of Success . . . 29
4.4 Results . . . 29
4.4.1 Calibration . . . 29
4.4.2 Manual Cart Movement . . . 29
4.5 Discussion . . . 30
4.5.1 Cart Trajectory . . . 30
4.5.2 Cart Tilt . . . 31
4.5.3 Comparison with Mechanical Data . . . 31
4.5.4 Shear Sensor Performance . . . 32
4.6 Conclusion . . . 34

5 [002-04] Control and Communication **35**
5.1 Aim . . . 35
5.2 Method . . . 35
5.2.1 Description of apparatus . . . 35
5.3 Experimental Procedure and Results . . . 36
5.3.1 Servo Loop Test . . . 36
5.3.2 Cart Control . . . 39
5.3.3 Pipe attenuation . . . 39
5.4 Discussion . . . 41

6 [002-05] Power Transmission 43

6.1 Aim . . . 43
6.2 Method . . . 43
6.3 Tests . . . 44
6.3.1 Mechanical . . . 44
6.3.2 Electrical . . . 44
6.4 Limitations . . . 45
6.5 Extrapolation . . . 45
6.6 Conclusions . . . 45
6.7 Comments . . . 47
6.7.1 Pick-up transformer . . . 47
6.7.2 Wire tension . . . 47
6.7.3 Slewing power . . . 47

7 [002-06] Trolley Steering 49

7.1 Aim . . . 49
7.2 Definitions and useful constants . . . 49
7.3 Method . . . 49
7.4 Results . . . 50
7.4.1 General observations . . . 50
7.4.2 Repeatability in clocking . . . 50
7.4.3 Response to a clocking offset . . . 50
7.4.4 Response to a weight imbalance . . . 50
7.4.5 Response to a driving force imbalance . . . 50
7.4.6 Response to a misaligned wheel . . . 51
7.4.7 Tests with heavier trolley and higher CofG . . . 51
7.5 Discussion . . . 51

8 [002-07] OPD Disturbance Tests 53

8.1 Aim . . . 53
8.2 Overall Method . . . 53
8.3 Modelling of COAST trolley . . . 54
8.3.1 COAST System . . . 54
8.3.2 The COAST model . . . 55
8.3.3 Model behaviour . . . 56

8.4 Acceleration and Metrology Measurements . . . 57
8.4.1 Data recording . . . 57
8.4.2 Delay line table . . . 58
8.4.3 Arrangement for main OPD test . . . 58
8.4.4 Data processing . . . 59
8.5 COAST Results . . . 59
8.5.1 Delay line table . . . 59
8.5.2 COAST trolley results . . . 60
8.5.3 Conclusions . . . 60
8.6 Modelling of proposed MROI trolley . . . 61
8.6.1 The MROI Model . . . 61
8.6.2 Model behaviour . . . 61
8.7 Tests of Embryo Trolley in Test Rig . . . 62
8.7.1 Test arrangement . . . 62
8.7.2 Vibration modes of embryo trolley . . . 62
8.7.3 Isolation tests . . . 64
8.7.4 Measurement of disturbance spectra . . . 65
8.7.5 Effect of slewing trolley on pipe vibration . . . 65
8.8 MROI OPD Results . . . 66
8.8.1 Comparison with COAST vibration measurements . . . 66
8.8.2 Results from MROI model . . . 66
8.9 Effect of a gap between pipes . . . 67
8.9.1 Effect at tracking velocities . . . 67
8.9.2 Effect at slewing velocity . . . 68
8.10 Effect of misaligned wheel . . . 68

9 [002-08] Metrology 71
9.1 Aim . . . 71
9.2 Method . . . 71
9.2.1 Laser stability . . . 72
9.3 Definition of Success . . . 72
9.4 Results . . . 72
9.4.1 Metrology power error budget . . . 72
9.4.2 Diffraction calculations . . . 72

9.4.3 Shear stability calculation 74
9.4.4 Metrology error due to shear correction servo 74
9.4.5 Laser stability 75
9.5 Discussion 75
9.5.1 Fallback Options 76

10 Conclusions **77**

List of Figures

1.1 Concept sketch of trolley design in pipe 1
1.2 Optical diagram of MROI catseye 6

2.1 Sketch and photo of pipe joint 10
2.2 Optical shear measurements made while running the cart over two pipe joints. 11

3.1 Side view of the test rig showing the pipes, flexure mountings and pipe cradles. 14
3.2 Schematic end view of the pipe supports, showing the flexures. 15
3.3 Photo of the test rig from the north end showing the longitudinal restraint. 15
3.4 FEA model of test rig. 17
3.5 Locations for accelerometers and excitation on test rig. 17
3.6 Axial vibration response to an axial impulse applied at leg3 of the test rig. 18
3.7 Response to a vertical impulse applied to the centre span of pipe 2. 19

4.1 Top view of the trajectory experiment hardware. 26
4.2 Photographs showing the corner cube mounting. 27
4.3 An example of a laser spot imaged by the shear camera. 27
4.4 Measured beam shear deviation as a function of time during a manual cart pullthrough. 30
4.5 Measured beam shear deviation from a best-fit line as a function of distance during a manual cart pullthrough. 31
4.6 Pitch and yaw of a cart with 1.8m wheelbase 32
4.7 Machine-shop measurements of pipe deviation and comparison with shear data. 33

5.1 Diagram of COAST trolley servo loop. 36
5.2 Fringe power spectra with and without the RF link. 37
5.3 COAST trolley servo loop errors and derived power spectra, from metrology data. . . . 38
5.4 Noise power plot of RF receiver discriminator output. 39
5.5 Arrangement of aerials on both end plate and plate attached to cart. 40

6.1 Schematic of trial inductive power system for COAST trolley. 43
6.2 Photograph of COAST trolley with inductive power transfer pick-up fitted. 44
6.3 Metrology data from the COAST trolley powered normally and inductively while it was tracking at about 1.4mm/s. 46

8.1 COAST array layout, showing delay line trolleys. 54
8.2 Schematic of COAST trolley. 55
8.3 Top-level simulink model of COAST trolley. 56
8.4 COAST trolley transfer functions predicted by Simulink model. 58
8.5 MROI trolley axial simulation. 61
8.6 Prospective MROI trolley transfer functions. 62
8.7 Photograph of embryo trolley in test rig. 63
8.8 Response of trolley to a vertical impulse at one end. 64
8.9 Vertical response of trolley to a vertical impulse to the pipe. 65
8.10 Comparison of COAST and embryo trolley axial acceleration PSD. 66

9.1 Schematic layout of the optical metrology using the Zygo laser system. 73
9.2 Schematic optical diagram showing the use of wedges to displace the metrology beam on the catseye secondary. 75
9.3 Allan deviation measurements for the Zygo laser. 76

Chapter 1

Introduction and derived requirements

1.1 Background

The Cavendish Laboratory of the University of Cambridge is designing and prototyping delay lines for the Magdalena Ridge Observatory Interferometer (MROI). The concept for the delay lines was reviewed and approved in November 2004. As a brief reminder, the basic concept is for a catseye retroreflector on a wheeled trolley running in a vacuum pipe, with servo feedback from a laser metrology system. The overall idea is therefore similar to many existing and tested delay lines, but there are a number of innovative features which were introduced in order to meet the top-level requirements, the most stringent being those relating to high throughput and wavefront quality (defined broadly to include all visibility-reducing effects such as dispersion). The innovative features can be summarised as:

1. The entire 380m of optical path delay in each telescope beam is introduced by using a single-pass traverse of the delay-line vacuum pipes.
2. The delay line trolleys run directly on the inner surface of the vacuum pipe, and not on pre-installed rails.
3. The trolley uses low-bandwidth tilting of the cat's-eye secondary mirror to compensate for pupil shear variations introduced by imperfections in the pipe straightness.

The basic trolley design is shown in Figure 1.1. It was decided that it would be prudent to perform a series of experimental tests of the areas of the concept which had the potential for introducing significant technical risk to the project. The experiments were originally proposed in the document "Risk Reduction

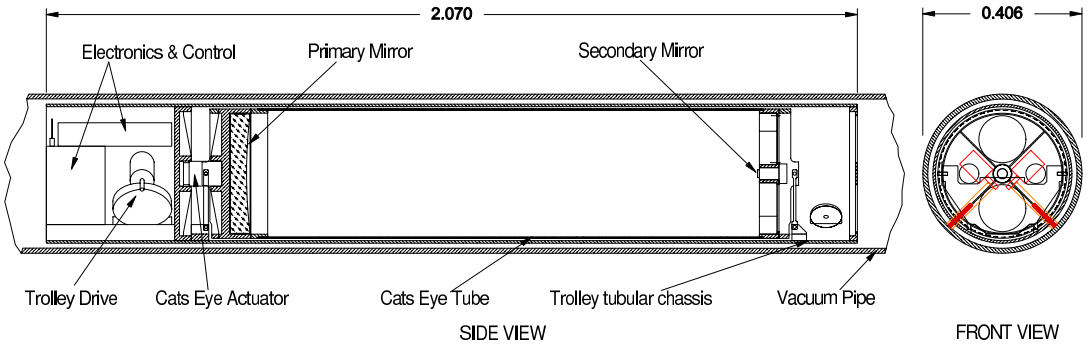

Figure 1.1: Concept sketch of the MROI trolley design inside the vacuum pipe.

Experiments Review", Revision 1.0 (November 8th, 2004), hereafter referred to as "RRER". It should be emphasised that these experiments were designed not to actually meet all the delay line requirements by the end of the experimental phase, but to demonstrate that the technical risks associated with getting the proposed concept to meet all the requirements would be both low and manageable, and hence minimize the overall risk that an entirely new delay line concept would be needed.

1.2 Scope

This document presents the results of the experiments proposed in the RRER. The results of individual experiments are given in subsequent chapters of this report.

The top-level requirements for the delay lines were presented in the RRER (see section 3 of that document) and approved as part of the November 2004 review of that document. In this chapter, we show how some of these functional requirements can be broken down to specific implementation requirements which are then tested in the experiments in later chapters. In particular we show how the dispersion and wavefront error requirements translate into vacuum requirements, and how the wavefront error requirements translate into alignment requirements of the catseye and requirements on the straightness of the pipe in which the trolley runs.

Some overall conclusions are presented in Chapter 10, addressing the question of whether any of the originally proposed concepts would need to be substantially changed in the light of the experimental results, and any potential cost implications of such changes.

1.3 Vacuum system derived requirements

We here determine what level of vacuum is required in the delay line in order to meet the overall requirements. When there is any residual air in the delay line system, there are three main effects of imporance to the operation of the delay line:

1. There is dispersion caused by the unequal air paths travelled by the starlight beams through different delay lines.
2. There are wavefront errors caused by refractive-index changes in the air caused by local heating effects.
3. The remaining air may have significant thermal conductivity and so can be used to cool any heat-dissipating components on the delay line carriage.

We look at each of these effects in turn below.

1.3.1 Dispersion

The requirement in the Risk Reduction Experiments Review document was stated as: "the differential optical dispersion between beams propagating through any two delay lines shall be such that there is less than 0.175 radians of differential optical phase change across any bandpass with a fractional bandwidth of 5%, anywhere within the R,I, J, H and K astronomical photometric bands.". This requirement needs to be modified because the range of bands over which the 5% bandpass requirement is important can be relaxed: in the R and I bands, high-efficiency photon-counting detectors are available (EMCCDs), and therefore there is no signal-to-noise penalty for using narrower spectral bands. Optical-wavelength

beam-combiner spectrographs with a minimum resolving power of R=200 are therefore easily feasible. In the infrared J, H, and K bands, there is a read-noise penalty for higher spectral dispersion and so the originally stated resolving power of R=20 (i.e. 5% bandpasses) is a reasonable minimum value. Thus the requirement is restated as: "the differential optical dispersion between beams propagating through any two delay lines shall be such that there is less than 0.175 radians of differential optical phase change across any bandpass with a fractional bandwidth of 5% anywhere within the J, H and K astronomical photometric bands and across any bandpass with a fractional bandwidth of 0.5% anywhere within the astronomical R and I bands."

The phase change across any bandpass can be reduced by applying an extra delay, the so-called group delay, which minimises the gradient of the phase change with wavelength. Table 1.1 shows the calculated dispersion effects of 1m of differential air path at 1 bar pressure. It is assumed in this table that only one group delay correction can be applied to a given photometric bandpass, and this correction is chosen to minimise the phase gradient at the centre of the bandpass. It can be seen from this table that the group delay centres for different optical bandpasses are different by distances of order microns, which would need to be compensated for by having extra differential optical path length adjustments in different beam combiners operating in different passbands. More serious is the phase change across the bandpasses, which for these purposes are most important at the edge of the J band (centred on 1.25μm) — at shorter wavelengths the narrower (0.5%) bandpasses make the dispersion effects less of a problem. In the J band the phase change across a 5% bandpass for 1m of air is 0.148 radians. In order to meet the requirement of 0.175 radians of phase change for 400m of optical path, this path needs to contain less than 3 parts in 1000 of air, i.e. a maximum pressure of 3 millibars is allowed. To allow an engineering margin of safety, the design goal for the delay line vacuum system has been set to 1 millibar.

1.3.2 Wavefront errors

As in normal air, atmospheric "seeing" can occur in vacuum pipes with residual air, if pockets of hot and cold air occur in the optical beam. The most likely cause of large temperature differentials in the air is heating from the trolley itself.

As shown later, the trolley temperature may be of order 20° C higher than the vacuum pipe wall, say 30°C in with a pipe wall temperature of 10°C. We can imagine that, as the trolley slews down the delay lines, it may shed random "blobs" of heated air at 30°C, each of order 20cm in diameter. The differential optical path introduced by one such blob of air at a pressure of 1 millibar is 3.84nm. If the pipe is filled with such random blobs, there will be 1000 such blobs in the outward optical path and 1000 in the return path, for a pipe of length 200m. If the blobs are randomly mixed with blobs at 10°C, then the RMS optical pathlength perturbation will be of order $\sqrt{1000} \times 3.84 = 121$nm, which exceeds the delay line wavefront error budget.

However, the above scenario requires that the heated air blobs survive for a long time. In fact the thermal time constant of the blobs will be small in a low-pressure environment. The time constant of a sinusoidal temperature perturbation of wavelength λ is given by

$$\tau = \frac{1}{K}\left(\frac{\lambda}{2\pi}\right)^2$$

where K is the thermal diffusivity given by.

$$K = \frac{k}{C\rho}$$

Photometric band	Wavelength (μm)	Group delay offset (μm)	Phase offset (radians)
R	0.63	10.88	1.1324
R	0.66	9.62	0.2489
R	0.70	8.56	0.0000
R	0.73	7.65	0.1954
R	0.77	6.87	0.7014
I	0.81	6.10	0.5188
I	0.85	5.37	0.1141
I	0.90	4.74	0.0000
I	0.95	4.20	0.0898
I	0.99	3.74	0.3224
J	1.12	2.67	0.1899
J	1.19	2.30	0.0418
J	1.25	1.98	0.0000
J	1.31	1.71	0.0329
J	1.38	1.47	0.1183
H	1.48	1.12	0.0818
H	1.57	0.91	0.0180
H	1.65	0.73	0.0000
H	1.73	0.58	0.0142
H	1.81	0.44	0.0510
K	1.98	0.22	0.0343
K	2.09	0.10	0.0076
K	2.20	0.00	0.0000
K	2.31	-0.09	0.0060
K	2.42	-0.16	0.0214

Table 1.1: Dispersive effects for 1m of dry air at 1013 mbar pressure and 20°C temperature, tabulated for wavelengths corresponding to the edges of sets of 4 spectral channels with 5% bandpasses, centred very roughly on the R, I, J, H, and K photometric bands. Group delay offsets are relative to that required to compensate for the phase gradient at a wavelength of 2.2μm, whereas the phase offsets are relative to the centre of the relevant photometric band, and calculated assuming perfect group delay compensation at the centre of each band.

with *k* being the conductivity, *C* being the specific heat capacity and ρ the density. The thermal diffusivity of air increases with decreasing air pressure because the conductivity remains roughly constant (providing the mean free path is smaller than the smallest dimensions being considered), as does the specific heat, but the density falls. Substituting $\lambda = 40$cm (i.e. the largest sinusoidal perturbation sustainable in a 40cm pipe) and a thermal difussivity appropriate for air at 1 millibar, we arrive at a time constant of 0.213 seconds.

The time taken for the trolley to move by 20cm at 1m/s slewing speed is 0.2 seconds, so even moving at its maximum speed, the trolley cannot create more than 1 blob of heated air before the previous blob has dissipated. Thus the air is unable to sustain temperature perturbations for long enough to fill the pipe

with differentially heated blobs of air. In reality the effective size of the dominant thermal perturbations will be smaller than 20cm, perhaps the size of the gap between the trolley and the pipe wall (1cm), and so will dissipate even more rapidly than indicated above (note that the thermal time-constant scales as the square of the spatial scale of the perturbation). Thus the maximum wavefront perturbation due to differentially heated air in the pipe can safely be assumed to be negligible.

1.3.3 Thermal conductivity

A positive aspect of the residual air in the pipe will be its thermal conductivity, allowing the trolley to dissipate heat by conduction through the air to the pipe walls. The thermal conductivity of air remains approximately constant with decreasing pressure until the mean free path of the molecules becomes larger than the typical distance over which the heat is to be transferred. For a cylindrical trolley running inside a cylindrical pipe, where the gap between the trolley and the pipe wall is of order 1cm, then the pressure at which the mean free path becomes comparable to the gap is approximately 0.03 millibar. Air at 1 millibar therefore has the same thermal conductivity as room pressure air, i.e. about $0.02\mathrm{Wm}^{-1}\mathrm{K}^{-1}$. For a trolley 2m long and 35cm in diameter, i.e. with a total surface area of $2\mathrm{m}^2$, then the trolley surface can sink heat to the pipe wall at a rate of about $4\mathrm{WK}^{-1}$. Therefore to dissipate a peak power of perhaps 50W, the trolley temperature needs to be about 12.5°C higher than the pipe. We adopt a design value for the temperature differential between the trolley and the pipe of 20°C, to allow for the thermal resistance of the trolley and between the trolley/pipes and the air.

1.4 Catseye optical analysis

Here we determine any fixed and varying aberrations introduced by the optical design of the trolley, concentrating on the novel aspect of the optical design, namely the correction of the beam shear introduced by pipe imperfections.

1.4.1 Design overview

The basic optical design for the MROI delay lines comprises a parabolic primary mirror with a planar secondary mirror mounted at its focus. In this design (see Fig. 1.2 for a cartoon of the arrangement) an incident collimated beam will be focused onto the secondary and return, remaining collimated, back along the original direction it came from displaced by a fixed separation, S. For the proposed MROI trolleys, $S = 160\,\mathrm{mm}$, the focal length of the primary (f), is 1200 m and the input and output beam diameters (D) are 95 mm.

In the following sections we quantify the requirements placed on the optical performance of the MROI delay lines from the top-level science requirements, and present the results of a ZEMAX analysis of the carriage optical design so as to assess the difficulties associated with meeting these requirements.

1.4.2 Relevant requirements

The Risk Reduction Experiments Review document allocates a total static wavefront error of 60nm to the delay lines (including the delay line windows). Static tilt errors will have no effect on the interferometric fringe visibility because these will be taken out in the nightly alignment of the interferometer, so in practice this means higher-order wavefront errors.

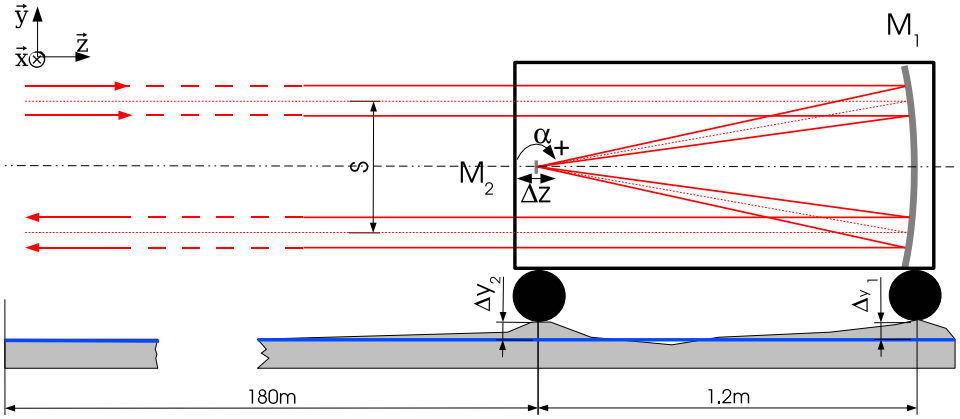

Figure 1.2: A cartoon showing the optical set up proposed for the MROI delay line carriages with the input beam travelling from left to right and exiting at the lower level to the left.In this schematic figure the wheels of the carriage are show located underneath the primary ($M1$) and secondary ($M2$) mirrors which are separated by 1.2 metres. Imperfections of the inner pipe surface, on which the delay line carriage wheels run, are characterised by the quantities Δy_1 and Δy_2, which represent the heights/depths of any excursions of the real pipe surface from a flat "perfect" pipe.

Defocus (μm)	RMS high-order aberration (nm)	Wavefront tilt (arcseconds)
10	4.5	0.23
20	9.0	0.46
30	13.5	0.69
40	18.0	0.92

Table 1.2: Wavefront aberration and induced tilt as a function of secondary defocus.

There was no requirement set on dynamic tilt errors induced by the delay line because these were thought to be negligible due to the retroreflecting nature of the catseye, but in fact these are the dominant aberrations induced by various dynamic misalignments which may be present, as shown below. A requirement of a dynamic tilt error which introduces no more than 1% change in fringe visibility at a wavelength of 1.65μm is therefore proposed. Assuming that the tilt errors in different delay lines are uncorrelated, this translates to a requirement of an RMS dynamic tilt error of no more than 0.216 arcseconds (i.e. 1.05μrad) in each delay line.

The total dynamic change in pupil shear allowed over the stroke of the delay line is 1mm RMS. Note that the above dynamic angular error will cause a beam shear of only 0.2mm over a 200m path, i.e. small compated to the allowable beam shear.

1.4.3 Effect of catseye defocus

If the distance between the catseye primary and secondary mirror is not exactly equal to the primary mirror focal length, this will introduce a defocus to the catseye. Its effect on the starlight beam will be both to introduce a defocus aberration in the beam and also to introduce a change in the tilt of the outgoing beam, i.e. the catseye will not be a perfect retroreflector. The resulting tilt and higher-order aberrations were calculated using the ZEMAX program for various errors in the primary secondary despace and are shown in Table 1.2.

It can be seen from the table that the high-order aberrations are within the allowed error budget for

Rotation (millirad)	RMS high-order aberration (nm)	Wavefront tilt (arcseconds)
3.33	2.8	0.14
5.0	6.8	0.33

Table 1.3: Wavefront aberration and induced tilt as a function of rotation about catseye vertex.

defocus values of order 40μm. On the other hand, the dynamic tilt error budget is exceeded if the despace *changes* by more than about 10μm after the interferometer is aligned. By way of comparison, a 1 metre long bar of Aluminum will expand by 23 μm for a 1 degree Centigrade rise in temperature, whereas a low-expansion carbon-fibre tube 1 metre long will *contract* by 0.1 μm.

1.5 Effects of catseye rotation and translation

Imperfections in the pipe will cause the catseye to be tilted and translated as the trolley moves along the pipe. Any combination of translation and rotation of the catseye as a solid body can be decomposed into a translation of the whole catseye plus a rotation about a single point, here chosen to be the the intersection of the optical axis of the primary mirror and the front surface of the secondary mirror - we hereafter denote this as the "catseye vertex". In all cases, the translations and rotations are denoted relative to the nominal location and rotation of the catseye, i.e. the optical axis of the catseye parallel to the optical axis of the incoming beam and exactly 80mm below its centre.

ZEMAX modelling shows that a pure translation of the catseye with respect to its nominal position gives the expected effect, namely a translation transverse to the optical axis by an amount x gives rise to a shear in the outgoing beam by an amount $2x$, but does not introduce any beam tilt or any higher-order aberrations.

Rotation of the catseye about the catseye vertex causes no additional beam shear, but does introduce both higher-order aberrations and beam tilt as shown in Table 1.3. It can be seen that rotation of the catseye by more than about 4 milliradians will exceed the allowable tilt error. For a delay-line carriage with a wheelbase of 1.8 m, this rotation corresponds to raising the front wheel 7.2 mm above the back wheel or vice-versa.

1.5.1 Effect of tilting the secondary mirror

One of the primary design innovations of the trolley design is the decision to actively tilt the catseye secondary mirror in order to counteract the shear introduced by transverse translations of the trolley due to non-straight pipes. ZEMAX calculations confirm the analytic result that tilting the secondary mirror by an angle θ about the point of intersection of the optical axis with the front face of the secondary causes a change in shear of the outgoing beam of $2f\theta$, but causes no tilt or higher-order aberrations. Therefore arbitrary translations of the catseye can be accomodated, limited only by the clear aperture of the catseye. The clear aperture has been specified to allow a $\pm$5mm translation of the incoming beam with respect to the catseye, which can be compensated for by a $\pm$4.2 milliradian rotation of the secondary.

It should be noted that rotation of the secondary about some point which is not on the optical axis will cause the intersection of the mirror face with the optical axis to translate along the optical axis, i.e. introducing a defocus. For a 4.2 milliradian tilt about a point 1mm from the optical axis, the induced change in the primary-secondary despace will be 4.2μm.

Item	Amount	High-order wavefront aberration (nm)	Dynamic wavefront tilt (arcsec)	Note
Exit window figure error		16		Includes deformation due to mounting
Primary mirror figure		26		Based on delivered surface figure of prototype mirror, for two passes
Primary mirror support figure error		14		Two passes
Secondary mirror figure		0		Beam only illuminates a few microns of the surface
Secondary mirror static defocus	20μm	9		
Secondary mirror focus change	5μm	3	0.12	
Secondary mirror pivot point misalignment	1mm	2	0.10	Parasitic defocus caused by 4.2 mrad mirror tilt
Catseye pitch or yaw due to pipe non-straightness	$\pm$3.33 mrad	3	0.14	
Total (in quadrature)		35	0.21	

Table 1.4: Delivered wavefront quality error budget.

1.5.2 Summary error budget

On the assumption that the occurence of the aberrations and tilts from all of the above effects will be uncorrelated, we will assume that they add in quadrature, and arrive at the error budget shown in Table 1.4. It can be seen that the high-order aberrations are well under budget (60nm was budgeted): this is because of the need to keep the dynamic tilt values within budget. A lower-quality primary mirror could be used to save costs.

Chapter 2

[002-01] Pipe Coupling Scheme

Principal risks:

That the coupling mechanism used to join of sections of delay line pipe may not maintain a suitable level of vacuum integrity.

That the coupling mechanism used to join sections of delay line pipe may lead to gaps and bumps at the pipe interfaces that cause the delay-line carriage trajectory to be impacted sufficiently so as to effect the delay-compensation performance of the carriage, principally through the loss of the metrology signal.

2.1 Aim

To demonstrate that commercially available pipe can be joined well enough to provide adequately smooth tracks for the delay-line carriage without requiring expensive machining of the pipe ends, and that the joints are easy to assesmble in situ.

To show that commercial seals on the outside of the joints will provide satisfactory vacuum integrity without major work on the outside of the pipes.

To show that the proposed joints have satisfactory electrical properties for the inductive power tranmission system. This was not included in the experiments suggested in our original list.

2.2 Method

Two 12’ lengths of 16’ O.D. $\times$ 1/2” extruded aluminium pipe were purchased, and each cut into one 10’ and one 2’ length after being measured for straightness and roundness.

All 6 ends to be used in the jointing experiment were squared off on a large CNC miller, but no other machining was carried out.

The other ends of the two short pieces were turned in a lathe to provide a flat end face and a circular mouth so that end plates with spigots carrying “O” rings could be fitted to seal them.

The ends to be used for the jointing tests were then jig-drilled by hand for the alignment dowels, and brackets welded on to the sides and top and bottom of each pipe near the end for the drawbolts used to assemble the joints. Figure 2.1 shows the concept and the resulting assembly.

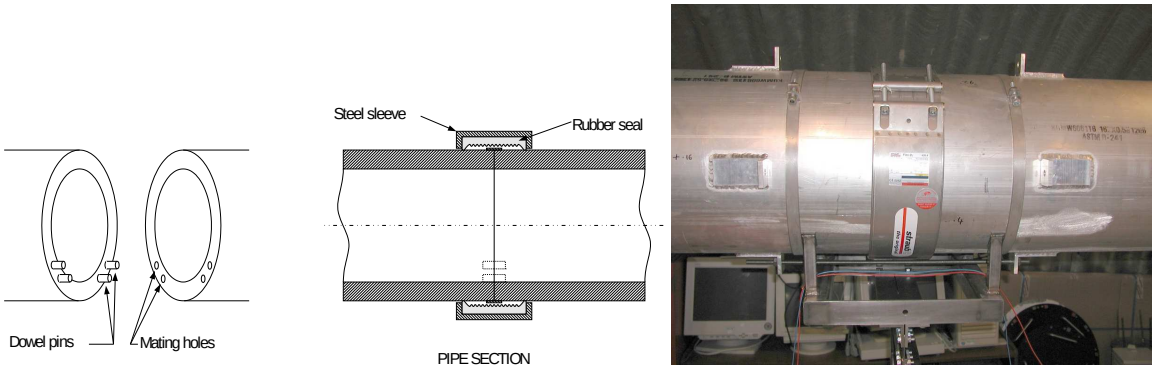

Figure 2.1: Sketch of the pipe coupling scheme (left) and photo of the assembled joint (right). In the photo there is a drawbolt in the lower flanges only.

The jig used is located from the inside of the pipe where the trolley wheels will run, so ensuring proper alignment of these tracks when assembled.

The pipe sections were then installed on the pipe supports (see Chapter 3) which had already been installed in the COAST building. No special equipment was used except a small hydraulic "engine-crane" as used for removing and installing motor vehicle engines, which was used to lift the pipe sections.

The combined assembly of jointed pipe sections and their supports was used for many of the experiments described in this document. This assembly is described in later chapters as the "test rig". A diagram and photograph of the test rig can be found in Chapter 3.

2.3 Tests

2.3.1 Ease of assembly

All the assembly was carried out by two people in well under one day using only hand tools, the joints being pulled together by the drawbolts with no problem. Hydraulic pullers would have reduced the effort required but seemed an unnecessary complication at this stage.

No problems were encountered with the alignment of the pipe sections in the cradles on the supports.

2.3.2 Mechanical alignment of the trolley wheel tracks

The smoothness of the wheel tracks was assessed in two ways, firstly by running the embryo trolley over the joints at various speeds and measuring the spectrum of the resulting accelerations (see Chapter 8), and also by looking for any steps in the trajectory measurements.

As reported in Section 8.9, the acceleration measurements obtained by running the trolley over joints were indistinguishable from those made in other parts of the pipe. The relevant trajectory measurements are presented in Figure 2.2 in this chapter, and these also indicate that the joints have no adverse effect.

Although the pipe ends were meant to be square cut, a small amount of de-burring had been carried out to make them safe to handle. This means that there is in effect a small gap (~ 0.5 mm) between the pipe ends at the surface even when the pipes are touching. To test how serious this might be, a definite real gap was introduced into one of the joints by inserting a shim between the pipes and repeating some of the measurements

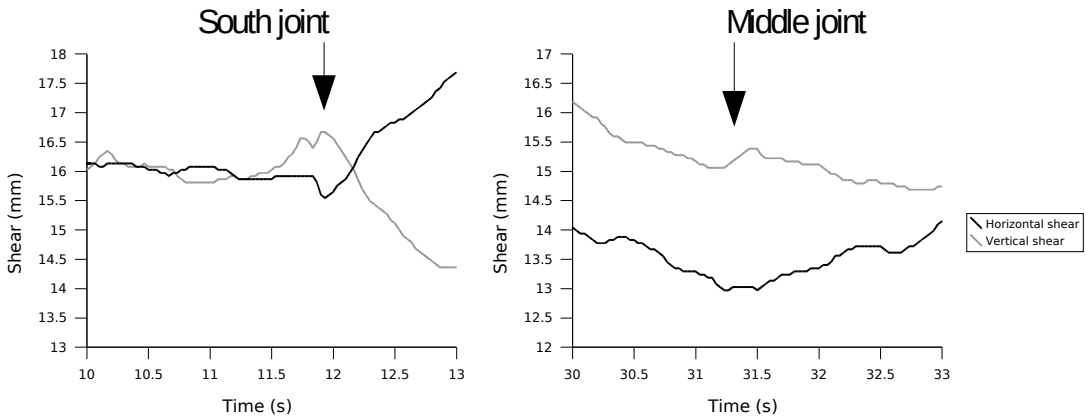

Figure 2.2: Optical shear measurements made while running the cart over two of the pipe joints at a velocity of about 0.15 m/s. The joints have little effect on the shear other than being the transition points between the gradients of adjacent pipes. This data is a subset of data plotted in full in Figure 4.4 in the discussion of optical shear tests (Chapter 4).

Table 2.1: Dial gauge measurements of steps at two pipe joints. The left-hand three columns contain measurements at the West wheel track and slightly to each side of it, and the right-hand three columns contain the corresponding measurements near the track of the other wheel.

	Step at joint going south (mm)						
	1 cm W	W.Track	1 cm E	Pipe bottom	1 cm W	E.Track	1 cm E
N Joint	-0.10	-0.03	+0.80	+1.0	+0.02	0.00	-0.16
S Joint	+0.40	+0.35	+0.40	-0.50	-0.15	+0.05	+0.30

It should be noted that it is our intention in the real pipe joints to introduce a small spacing shim (0.2 to 0.5 mm) at the bottom of the pipe so that the ends of the pipe sections only touch at one place. This is to allow some flexibility in the joint, and relax the tolerance on the squareness of the pipe ends. Obviously we need to know what size of gap can be tolerated for this purpose.

The northernmost joint was opened and the trolley run over gaps up to 3.7 mm with the results shown in Section 8.9. Gaps of 2.1 mm or smaller were difficult to detect in the accelerometer data, and even the 3.7 mm gap only gave rise to 11.8 nm RMS OPD error at a velocity of 2.2 mm/s.

Secondly a dial gauge was attached to the trolley and moved slowly over the north and south joints both along the intended track of the wheels and about 1 cm off to each side. In addition a measurement was made at the bottom of the pipe for comparison. The results are presented in Table 2.1.

Apart from the S.W. track the steps at the intended wheel tracks are much less than those 1 cm to each side, and quite acceptable, while the lack of match between the shape of the pipe ends is clearly visible. The slightly less good alignment of the S.W. track is due to the guide blocks on the dowel drilling jig covering too wide an area of the pipe. The blocks were made wide intentionally to avoid bruising the pipe, but they should properly have been made to match the wheel profile.

This clearly shows that the method of drilling the dowel holes is able to compensate at the wheel tracks for pipe ends that are out of round or different diameters.

2.3.3 Vacuum Integrity

The vacuum seals were installed on the pipes during the assembly process, initially with no grease, and with no preparation of the pipe surfaces, though these were quite badly scored in places either by

handling or during manufacture. The “O” rings on the endplates were greased as they have a much smaller contact area.

On first pumping the system down no problems occurred, but the vacuum was not held overnight. After re-torquing the seal clamping screws and two further pump downs a leak rate of 6 mb per day was obtained. This is still not good enough, but the vacuum test was temporarily suspended while tests on trolley motion in the pipe were carried out.

The joint over the most badly scored section of pipe was moved to allow mechanical tests on joint separation to be done, and the worst score was partially polished out. After re-assembly, again without grease the test was continued, and after a loose co-axial connector had been tightened a leak rate of 1.3 mb per day was achieved. This is still not entirely satisfactory even allowing for the fact that we have three seals in a 7 m pipe run whereas the real pipe will have one seal in 5 or 6 m.

It must be stressed however that these results were obtaind with *no* prior preparation, or even inspection, of the pipe ends except that mentioned above, and no grease was used on the seals which would undoubtedly make a substantial improvement.

2.3.4 Electrical Continuity

A simple test of the electical conductivity of the pipe joints was carried out by passing a current along the pipe run and measuring the voltage drop across the joints. The resistance of the joints was less than 0.5 milliohm which is very satisfactory.

2.4 Conclusions

We have demonstrated that the proposed pipe jointing concept produces joints in commercially available pipe satisfactory in all respects for the MROI delay line system, while requiring only a moderate amount of simple machining work on the pipe ends.

Chapter 3

[002-02] Pipe Support

Principal risks:

That it may be difficult to design and fabricate a suitable pipe support system in a cost effective manner.

That building a suitable system within a sensible space envelope may be difficult.

That the proposed supporting mechanism may lead to the possibility of undamped oscillations of the delay line pipes.

3.1 Aim

To design a pipe support scheme for the delay line vacuum pipes which is easy to install, is easy and quick to align, provides adequate support and constraint for the pipe while fitting in the required space envelope, and allows for the expected range of thermal and vacuum induced movement without being unduly susceptible to vibration.

To build a "test rig" consisting of short run of delay line pipes with the proposed supports, verify ease of installation and alignment, and measure the test rig's vibration properties.

To use the test rig results to validate dynamical modelling of the vibration properties of a 200 m pipe run.

The specific steps involved in realising the latter two aims are:

- Measure the vibration spectrum of the test rig and where possible estimate the damping of the significant modes.
- Develop an initial FEA model of the delay line test rig, assess the longitudinal and lateral resonance features and compare them to the measured performance of the test rig.
- Extrapolate these results to a longer sequence of jointed pipe.
- Develop a simple model for the delay line pipe to be included as part of the overall model for the delay line trolley used in Chapter 8.

3.2 Support Design

Consideration of various support schemes such as rigid mounting, rollers or sliding pads showed that either very large forces would have to be contained, or that quite large forces plus probable stick-slip

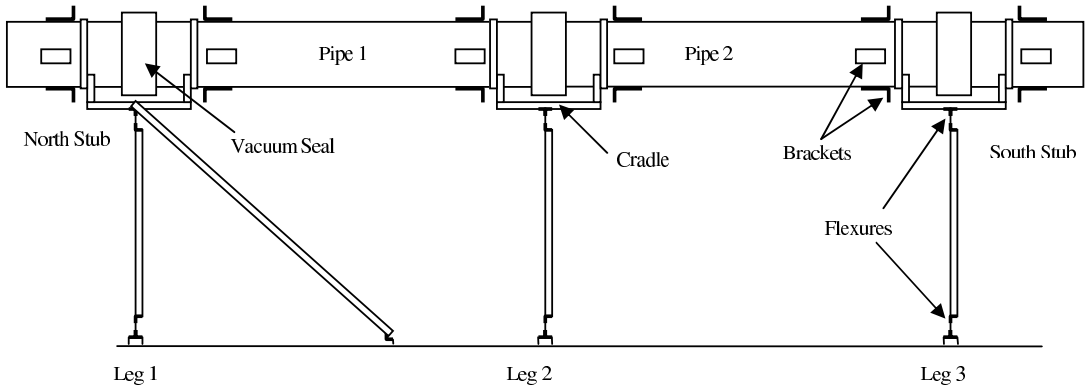

Figure 3.1: Side view of the test rig showing the pipes, flexure mountings and pipe cradles.

motion would result. The only sensible method is to use flexure legs, and these have to be quite long – 1 m or so – to avoid excessive height changes at the "free" end of the pipes. However the flexibility at the joints of our proposed system of pipe jointing means that the pipe does not have to be forced to lie straight as it would with flanged joints if there was any build up of tolerances. Also the weight of the pipe sections is such that gravity is sufficient to cope with vacuum forces. The pipes are however strapped down on the support cradles to make sure that there is no creep between the pipes and the legs.

Absence of large sideways forces (see Chapter 2) means that the legs do not need a wide base for stability, so that the legs and cradles are only the same width – 16" – as the pipes, and the bases are 22" wide so easily fitting into the 24" centre spacing proposed for the whole delay system.

The trial supports – 3 for 2 pipe sections and 2 ends – are identical, except that one of them has diagonal struts added in the longitudinal direction of the pipe to simulate a fixed end. With the flexures used in the initial trials the system would be unstable for large longitudinal deflections if not constrained (as shown in Figures 3.1 and 3.3). The flexures are intentionally made soft to reduce the force required to deflect the large number of legs on each pipe in the final system, and to reduce the shear load on the pipe alignment dowels necessary to bend the upper flexures (see Figures 3.1 and 3.2).

The legs are made of RHS mild steel, and the flexures, two at the top and two at the bottom of each leg, are made of steel plate bolted between clamping plates so they can be changed easily if need be.

The legs for the trial system are installed in the COAST building on studs bonded into holes drilled in the existing floor. No grout is used under the leg bases so the height can be adjusted both up and down. No specific provision was made for lateral adjustment, as this is such a short run, but small sideways movements of the top of the legs could be made by very slight transverse out of vertical setting of the legs. The resulting sideways movement when flexed longitudinally would be only second order and likely to be less than the first order effect of not getting the rest plane of the flexures perpendicular to the length of the pipe. In the final system it would be prudent to elongate the mounting holes in the bases transversely to allow for poor placement of the studs.

The pipe support cradle on top of the legs is fitted with oversize bolt holes so that it can rotate slightly in azimuth if need be when the pipe sections are installed.

It should be noted that whilst the two sections of pipe resting on each cradle balance each other so that small relative vertical movements are easy to make while lining up the dowels with their holes, the flexures are not stiff enough to support one pipe by itself. Measures to restrict the cradle movement during assembly must therefore be taken (for the test rig assembly ropes were used).

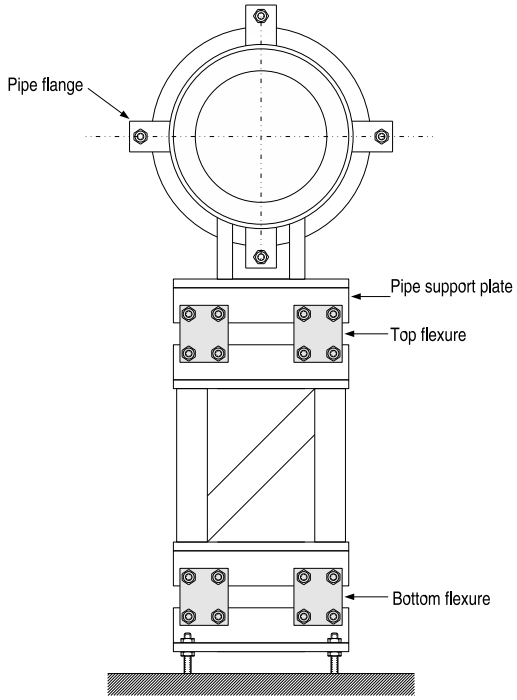

Figure 3.2: Schematic end view of the pipe supports, showing the flexures.

Figure 3.3: Photo of the test rig from the north end showing the longitudinal restraint (behind the northernmost flexure).

3.2.1 Support Installation

The layout of the bolt holes in the floor was marked out by reference to a stretched wire, using one of the leg bases as a template, and all the holes were drilled and the bolts fixed by two people in one morning. No problems were encountered in fitting the leg bases which were left in place as jigs while the bolt bonding cement set. The three legs were then assembled piecemeal by one person in the afternoon and the alignment checked visually. Small adjustments were then made in height and level as the floor itself was not quite flat. If the legs were to be assembled first it would help to have oversized bolt holes, and to use the small crane used for the pipes to lift them in place.

3.3 Vibration modelling and tests

A basic structural FEA package called CadrePro V was used to develop a 3D model of the test rig. The package provides the modes and visualised mode shapes together with nodal forces, accelerations and displacements, effective mass and participation factors etc. This is sufficient to compare with actual measurements but it is also possible to assemble a modal model which, together with observed damping data, can be manipulated to produce a state-space modal model of suitably reduced order for inclusion into a simulation study, as was done for the OPD analysis in Chapter 8.

The test rig frequencies and damping were measured using accelerometers to obtain the response to simple impulse disturbances. The accelerometer data was processed to produce power spectral densities which formed the basis of the comparison with the FEA results.

3.3.1 FEA model

The FEA model based on the test rig is shown in Figure 3.4. The model is represented by a single tube 7.2 m long, 0.406 m diameter, composed of 12.5 mm thick aluminium plate elements and resting on three identical cradle assemblies. The cradles and legs are formed of steel angle and tube to the dimensions used for manufacture. The flexures are represented by steel plates attached at the appropriate nodal positions. The points representing connection of the stand to the floor are simply zero displacement nodal constraints. The longitudinal constraint at one end of the pipe was accomplished using appropriate boundary conditions at the fixed cradle which provided the observed first longitudinal resonance. These approximations resulted in somewhat higher frequency predictions than would be realised in practice but are adequate for this particular task. The influence of the floor and the anchor bolts that the stands are attached to was not taken into account and so there is likely to be an additional low frequency mode in the lateral and vertical directions which the model does not predict. This is not of particular significance unless the actual frequency is very low due to a poor quality floor. The MROI delay line foundations are likely to be much better than the non-structural floor on which the test rig is fixed.

The output from the FEA was examined and the frequencies with the largest contribution to vibration amplitude in each direction (axial, lateral and vertical) were identified. These frequencies are presented in Table 3.1 in the results section for comparison with the actual frequencies determined in the vibration tests.

3.3.2 Vibration test method

The equipment used for these tests included two Bruel & Kjaer DeltaTron internally amplified piezo accelerometers suited to modal analysis. They have a bandwidth from 0.4 Hz to 6 kHz. ICS piezo-

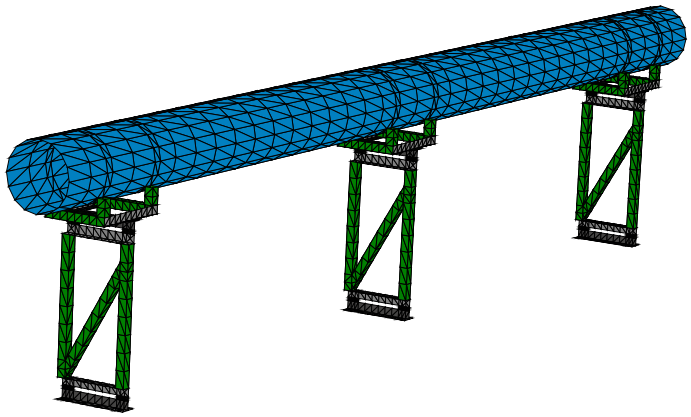

Figure 3.4: FEA model of test rig, including pipe supports.

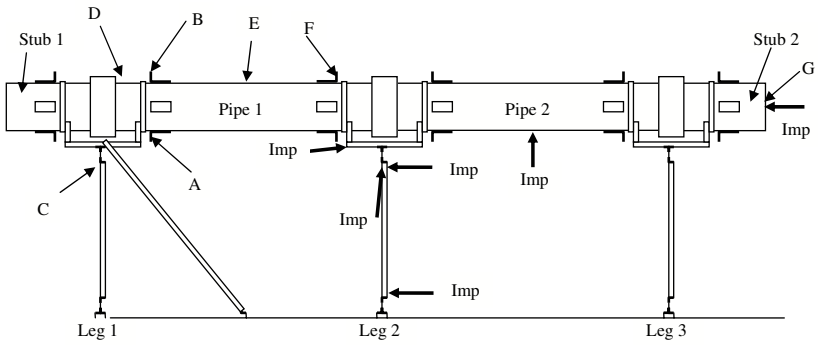

Figure 3.5: Locations for accelerometers and excitation on test rig: accelerometer locations A to G and impulse locations marked “Imp” can refer to all three legs and both pipes.

resistive silicon accelerometers were also used but these had a bandwidth of 0 Hz to only 800 Hz. A two-channel Siglab unit connected to a portable PC running MATLAB and configured for spectral analysis mode provided data acquisition facilities and real-time spectral analysis.

A number of locations were identified for placement of the accelerometers and the application of impulse loads; these are shown in the sketch in Figure 3.5.

About 45 tests were undertaken to identify the various modes in the assembly so that they could be compared to the results from the FEA model. Damping ratios for the fundamental modes were calculated from the impulse response using the logarithmic decrement method and those for the significant but well separated higher frequency modes were estimated using the “peak-picking” method. This uses the

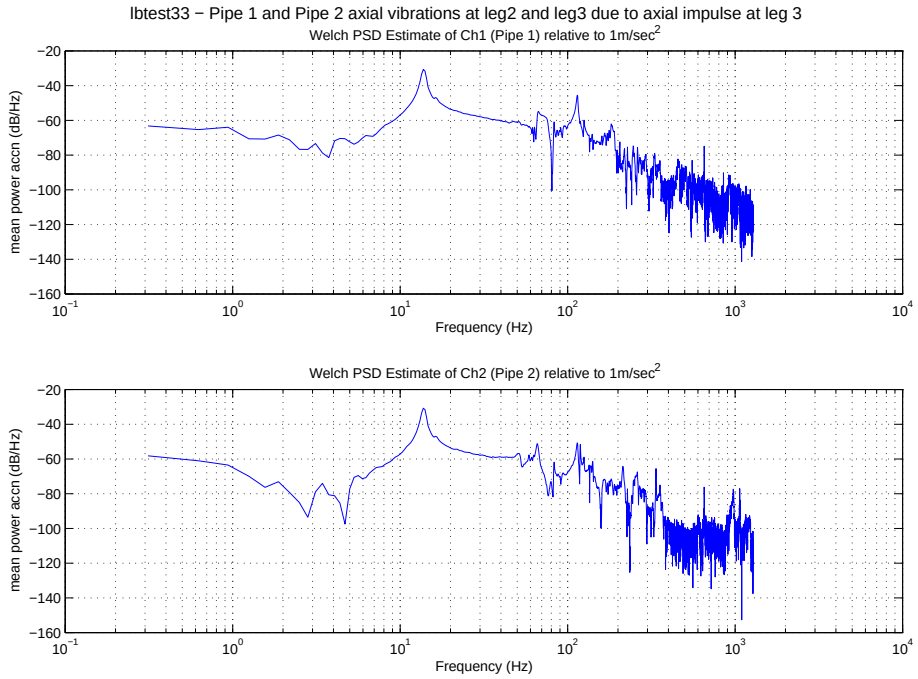

Figure 3.6: Power spectral densities of axial vibration response to an axial impulse applied at leg3. The top trace is the response monitored at position F of pipe 1 and the bottom trace is the response monitored at position F of pipe 2.

relationship between the frequencies of the half-power points and the peak. That is:

$$\zeta_r \approx \frac{\omega_b - \omega_a}{2\omega_r}, \tag{3.1}$$

where ζ_r is the damping ratio and ω_a and ω_b are the frequencies either side of the resonance where the power spectral density has dropped by 3 dB from the peak value.

3.3.3 Vibration test results

Examples of power spectral density obtained from test rig impulse responses are shown in Figure 3.6 and Figure 3.7 below. In Figure 3.6 the simultaneous axial response of each pipe to an axial impulse at leg 3 is shown. The axial response near the end of each pipe is identical at the first resonance of 14 Hz. The next significant peak, at 118 Hz, is the first piston mode of the stand framework due to the top and bottom flexures. At higher frequencies there are reduced magnitudes at pipe 1 compared to pipe 2, which is supported by the leg to which the impulse was applied.

The implication of these results is that there is unlikely to be increased damping for an increased number of sections for the lowest modes but there may be a reduction in transmission of vibration from one section to the next at higher frequencies. In particular, the sectioned pipe behaves as if it is a continuous piece of pipe for the lowest modes of vibration and this justifies modelling the delay line pipe as a continuous pipe.

The magnitude of the second peak at 118 Hz may look alarming but it should be remembered that:

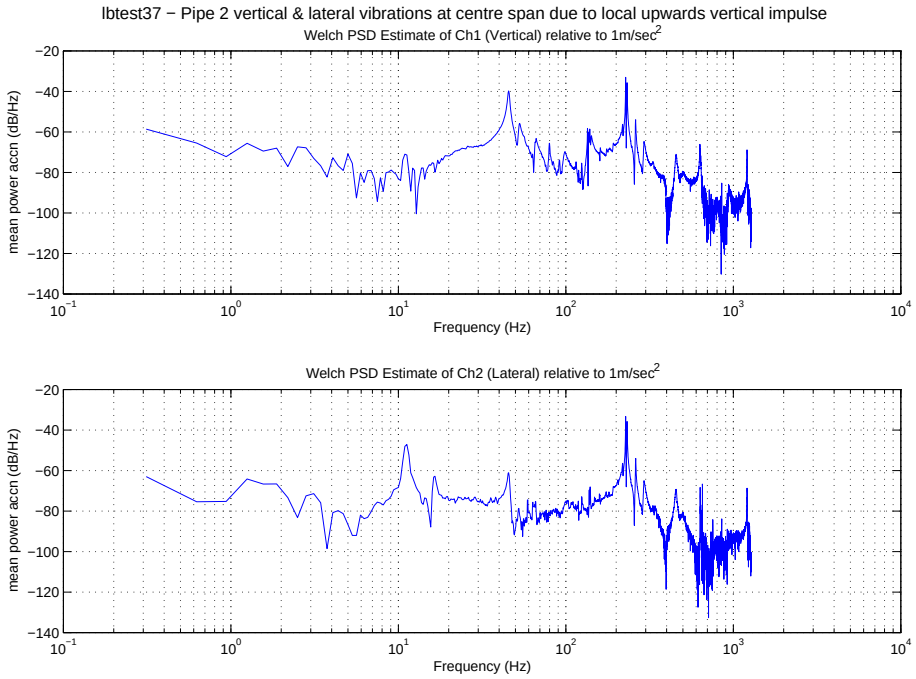

Figure 3.7: Power spectral density of the response to a vertical impulse applied close to the accelerometer positions at the centre span of pipe 2. The top trace is the vertical response measured at the top of the pipe and the bottom trace is the lateral response measured at the side.

1. An impulse is a broad band excitation specifically applied to excite the higher frequency modes and is of a magnitude unlikely to be encountered in normal operation.
2. The amplitude is 16 dB below the major axial resonance which is shown later in this section not to be a problem.
3. The displacement is proportional to $1/\omega^2$ so at this frequency it is going to be extremely small (10 nm RMS in this case) which if it got past the trolley wheels at all would face a further 55 dB of passive rejection from the cats-eye/flexure arrangement.

Figure 3.7 shows the vertical and lateral response at the centre span of pipe 2 due to a local vertical impulse.

The first vertical mode at 45 Hz is clear and is the first rigid body mode of the whole pipe in that direction. The strong resonance at 227/232 Hz is identical in the lateral and vertical directions and is possibly a combination of vertical and lateral bending modes of a single length of pipe. Lateral modes from 17 Hz to 66 Hz are lower than the FEA prediction by about 30% which is not far outside the 25% acceptability criterion. The mode at 11 Hz is not predicted at all. These lowered frequencies and an unpredicted mode are a typical result of an un-modelled but substantial compliance somewhere in the pipe support and is probably due to un-modelled connection details at the floor fixings, the floor itself or both. However, this is not a serious problem as this mode can be incorporated into the model now that we know it exists. It is also unlikely to present a problem for the MROI design since (a) the piston mode of the pipe will have the lowest frequency and is shown in Section 3.4 not to present a problem and (b) stands would be mounted on a structural foundation.

The mode at 230 Hz produces a vertical displacement amplitude of 10.7 nm RMS due to the impulse.

Table 3.1: Significant observed frequencies and identifiable FEA modes of the test rig.

Actual Freq. (Hz)	**Damp. ζ_r (%)**	**Comments**	**FEA Pred. (Hz)**
		Axial modes:	
13.7	2.5	Main piston mode of the test rig	14
83	0.5	Piston mode of stand associated with 1st vertical pipe mode	85
118	0.9	The piston mode of the support stand (legs)	116
125	0.3	Coupling of 2nd vertical bending mode of pipe	137
196	0.5	Axial mode of the support stands (legs Z)	192/193
337		Piston of pipe on flexures (350 Hz is theoretical free axial mode)	353
		Vertical modes:	
45/49	1.3	Rigid body vertical mode of the test rig	58
83	0.8	1st vertical bending mode of pipe	88
125	0.3	2nd vertical mode of pipe not seen at leg 2 (i.e. is a node)	137
216	0.4	Vertical pipe mode observable at support locations	233
220	0.3	Bending mode of the pipe at centre span of each length	226
230	0.3	Vertical bending mode of single pipe as is 630 Hz and 1150 Hz	263
		Lateral modes:	
11	2.0	Possibly a mode due to floor and fixings	-
17	2.0	Lateral rigid body mode of whole test rig	22
22	1.8	Affects pipe 1 & stand 2 but not pipe 2. Lateral mode of test rig	33
37/39	0.9	1st lateral bending mode of pipe	59
60	1.2	Lateral stand mode associated with stand 1	94
66	1.2	Lateral stand mode associated with stand 2	94
105		2nd lateral bending mode of pipe	135
230		Lateral bending mode of the pipe as is 630 Hz and 1150 Hz	257

This faces 20 dB of isolation due to the trolley wheels and then a large amount of rejection due to the trolley mass. Only some very small fraction of what is transmitted would couple into the OPD direction at the cats-eye. So the effect is $\ll 1$ nm.

The observed frequencies, the associated damping estimates, where available, and the FEA modes most likely to be identified with them are presented in Table 3.1. The higher frequency modes will have extremely small amplitudes as has been explained.

3.3.4 Effect of moving trolley on pipe vibration

An approximation of the peak magnitude of axial displacement can be made by taking the peak acceleration from the time response to an impulse at the end of the pipe and dividing by the square of the frequency. For the principal axial mode at 14 Hz a specific test yielded an acceleration of 0.08 m/sec^2 and hence a peak displacement of 10.3 μm. The force applied can be estimated from the relationship

$$v = \frac{F \times \Delta t}{m}, \tag{3.2}$$

where v is the resulting maximum velocity, $F \times \Delta t$ is the area under the impulse function and m is the mass of the object receiving the impulse. Δt is estimated from the initial impulse response hence the force can be obtained.

For this specific test the velocity was obtained from the peak acceleration, the effective mass of the pipe

in the test rig is 330 kg and Δt is 10 msec. Hence

$$F = \frac{v \times m}{\Delta t} = \frac{9.1 \times 10^{-4} \times 330}{0.01} = 30\,\text{N}. \tag{3.3}$$

So for an applied axial impulse force of 30 N the displacement is 10.3 μm, i.e. 0.3 μm/N.

It is not expected that variable forces imparted by the trolley during tracking would be more than 1 N RMS and therefore the axial displacement of the pipe from this source would be only 0.3 μm RMS. Even if the trolley were able to follow all of this motion of the pipe the passive rejection alone of the MROI trolley cats-eye would reduce the OPD displacement by 55 dB, i.e to 0.53 nm RMS. The closed loop cat's eye servo could be expected to provide around 17 dB of rejection at 14 Hz for a servo bandwidth of 180 Hz, and hence the residual cats-eye displacement would be reduced from 0.53 nm to about 0.07 nm RMS.

A specific test was carried out on the test rig to assess the vibration induced by the embryo trolley driving at slewing velocities. Accelerometers were placed on the pipe to monitor axial and vertical vibrations at the centre span of pipe 1. The reaction of the pipe was recorded while the cart was driven along it at 11 mm/s, 55 mm/s and 110 mm/s. The axial mode of the test rig at 14 Hz is evident in the background spectrum at -75 dB. This increased slightly to -74 dB for a trolley velocity of 11 mm/s, to -58 dB at 55 mm/s and to -52 dB for 110 mm/s. This last result corresponds to an axial displacement of the pipe of only 0.44 μm RMS. There was much less of an increase in vibration of the pipe in the vertical direction when the trolley was in motion. At the first pipe resonance at 45 Hz the background level increased from -85 dB to -80 dB at 50 mm/sec and to -72 dB at 100 mm/sec. These tests confirm that trolley induced vibration in the pipe is insignificant in the modes that are most easily excited.

3.4 Extension of model to 200 m

The results from these tests show that the FEA model is sufficiently representative to justify extending it to a long delay line model. The individual modes of a single pipe length and the stands that support it are not greatly modified by extensions to greater lengths. Slight material, manufacturing and assembly differences produce slightly different frequencies and the effect of vibration on one pipe is to excite the modes of the next with some dissipation of energy in the process. So at any one point along the pipe the vibration characteristics will be those of that particular section plus those of the overall length of the delay line.

The method chosen for modelling the whole length was to calculate a representative stiffness for each orthogonal degree of freedom of a support stand and to treat the pipe-line as a single beam with 40 5 m sections, sprung at 40 nodes and an anchor point with assumed rigidity. To retain the most significant modes of each pipe section the 5 m sections are represented by 10 beam elements. To validate this approach the scheme was applied to a 7.2 m length beam split into sixteen elements to represent the test rig model. The output of the FEA for the beam model was then compared to the detailed model to ensure that the modal frequencies were preserved to within 10%. This was the case for the low flexure modes under consideration except those connected with sub-modes of the stand e.g. the piston of the legs. Axial rigid body modes were accurately predicted as expected but vertical and lateral rigid body modes were not and this is probably due to a modelling error or oversimplification. Hence some further work needs to be done to ensure these modes are captured.

The 200 m beam model was assessed for bending modes and the first piston mode since the modelling of the 7.2 m beam did agree well with the detailed model for these modes. The qualitative results are:

1. For an infinitely stiff anchor at one end of the pipe line the first piston mode is 6.4 Hz so any realistic implementation will result in a lower frequency than this. Does it matter? Based on the disturbance amplitudes calculated for the test rig in Section 3.3.4, if we allowed 1 nm OPD error instead of 0.07 this gives a factor of 14 by which we could shift ω^2. But there is an additional factor of 27 because the mass of the pipeline is increased by this much. Hence we could allow ω^2 to change by a factor of 378 hence f could drop from 14 Hz to 0.72 Hz. If we were to increase the mass of the test rig by a factor of 27 then the frequency would drop by the square root of 27, that is to $14/5.2 = 2.7$ Hz. So we know there is no problem in providing sufficient anchor stiffness.
2. The first 3 modes are piston modes, 6.4 Hz, 19.1 Hz and 31.8 Hz. Modes 6 (44.5 Hz) and 42 (57.3 Hz) are also piston modes.
3. Many lateral modes and mode shapes exist from 46 Hz upwards with the principal mode being 46 Hz. This means that if the pipe is disturbed the amplitude of this frequency would dominate all other lateral frequencies by a factor of at least 10:1.
4. There are many vertical modes and mode shapes from 44 Hz upwards and the dominant is at 78 Hz.
5. Observation of the dominant modes leads to the conclusion that they are based on the first bending mode of the pipe section, 88 Hz for the vertical mode and 59 Hz for the lateral. The amplitudes of these modes dominate all the others by a factor of 10 or more and therefore one need only include these modes to obtain a sufficiently representative model.
6. The amplitude of the axial mode dominates that of the vertical and lateral modes and for the same reasoning as presented in point 3 in Section 3.3.3, these modes will provide only extremely small displacement amplitudes which would be easily rejected by the carriage and subsequent cats-eye passive isolation.

Although the 200 m beam FEA model is not fully representative in the lateral direction, applying a load spectrum using the shock spectrum tool available in the software is instructive. A flat spectrum of amplitude 0.01g over bandwidth 0.01 Hz to 2 kHz was applied through each restrained node hence each of the 41 support locations received this acceleration. The program calculates the resulting displacements over all the included modes and provides an RMS displacement. Scaling the result to provide the RMS displacement for 1 N produces 0.11 μm in the axial direction, 0.04 μm in the vertical direction and 0.08 μm in the lateral direction. The axial result is consistent with that presented in Section 3.3.4 and the lateral and vertical results are expected to be less because of the higher frequencies.

These results quantify the expected deflections due to excitation of the first 100 modes which include the most significant modes of the structure except for the lateral rigid body mode. The displacement contribution from this can be estimated from the relationship

$$d = \frac{F}{m\omega^2}, \tag{3.4}$$

where F is 1 N RMS, m is 330 kg (one length of pipe plus 50% of stand) and ω is 22 Hz. This gives 0.16 μm RMS which can be added in quadrature with 0.08 μm from the other modes to give 0.18 μm RMS. This result is also consistent with other modal deflections and, for reasons already discussed, presents no significant contribution to the OPD error.

3.5 Conclusions

The pipe supports as used for the test rig are quick and easy to install and align. More tolerance for lateral alignment on a long run could easily be provided by elongating the bolt holes in the bases.

Comparison with the measured performance of the test rig has shown the finite element modelling to be representative for the frequency range considered. Hence the FEA technique can be used to develop a general model for the support of a 200 m pipe.

The damping ratios are within the range expected for structural damping (0.2% to 2%) and vary with frequency, as expected. Damping associated with the stands, including vertical and lateral motion of the pipe is generally 1% to 2% for the low order modes so a general value of 1.5% could be assumed in a development of a damped model. Damping of the major modes is unaffected by the joint but there is some indication that transmission of vibration is reduced from one section to the next.

Not all low frequency modes of the test rig are predicted by the model but this is almost certainly because the floor and the connection to it is assumed to be infinitely stiff. There should be little impact from this given the low lateral frequency that persists in any case but it would be wise to include some detailing in future analyses.

The lowest mode of vibration in the OPD direction is determined by the compliance of the anchor at on end of the pipe. In this case a simple anchor is shown to be sufficiently stiff that the expected OPD error due to the pipe vibrations would be less than 1 nm RMS.

The method of supporting the pipe does not introduce any significant excitation of modes due to cart motion. Displacement amplitudes are extremely low, less than 0.3 μm in the most sensitive direction at tracking velocities. High frequency modes of the pipe produce extremely small displacements and would be substantially rejected by the passive isolation that the trolley design possesses.

The extension of the model to 200 m using beam elements is mostly successful but needs further work to ensure that the lateral rigid body mode is captured. Shock spectrum analysis confirms amplitudes of vibration with this model that are consistent with the measurements on the test rig. Therefore the proposed scheme for supporting the pipe in a 200 m delay line more than adequately meets the requirements.

Chapter 4

[002-03] Carriage Trajectory

Principal risks:

That the carriage trajectory defined by the inner surface of jointed aluminum pipe may not be uniform enough to allow the top-level system requirements to be met. In particular that the rate and amplitude of the pupil shifts and wavefront aberrations introduced by a non-ideal carriage trajectory will be larger than can be accommodated by the proposed delay line trolley.

4.1 Aim

There is a risk that the cart trajectory cannot be made sufficiently straight to comply with MROI requirements (from the introduction, a catseye displacement less than $\pm$5mm and a cart tilt less than 3.3mrad if the catseye primary mirror focal length is 1.2m). Here we aim to establish whether the amplitudes of beam shear and cart tilt caused by imperfections of the prototype delay line pipe and cart are within those limits. If they are, then the risk associated with this part of the design is mitigated.

4.2 Method

4.2.1 Description of apparatus

An overview of the test is shown in Figure 4.1. It makes use of a retroreflecting corner-cube mounted on the "embryo" cart inside the pipe test rig and an optical table that supports a laser, various optical components and a camera. The apparatus measures variations in beam shear as the cart is moved from one end of the pipe to the other.

Considering the components in the order of optical traversal:

- 633nm coherent light from a helium neon laser passes through a 10$\times$ beam expander and is then reflected off two mirrors, M1 and M2, that raise the beam height to that of the pipe test rig axis and direct the light towards the corner cube on the cart. The beam expander reduces the change in beam diameter due to diffraction over the total optical path (10–20m). The mirrors provide sufficient degrees of freedom to trim both the beam offset and its launch direction to match the average trajectory of the cart and corner cube.

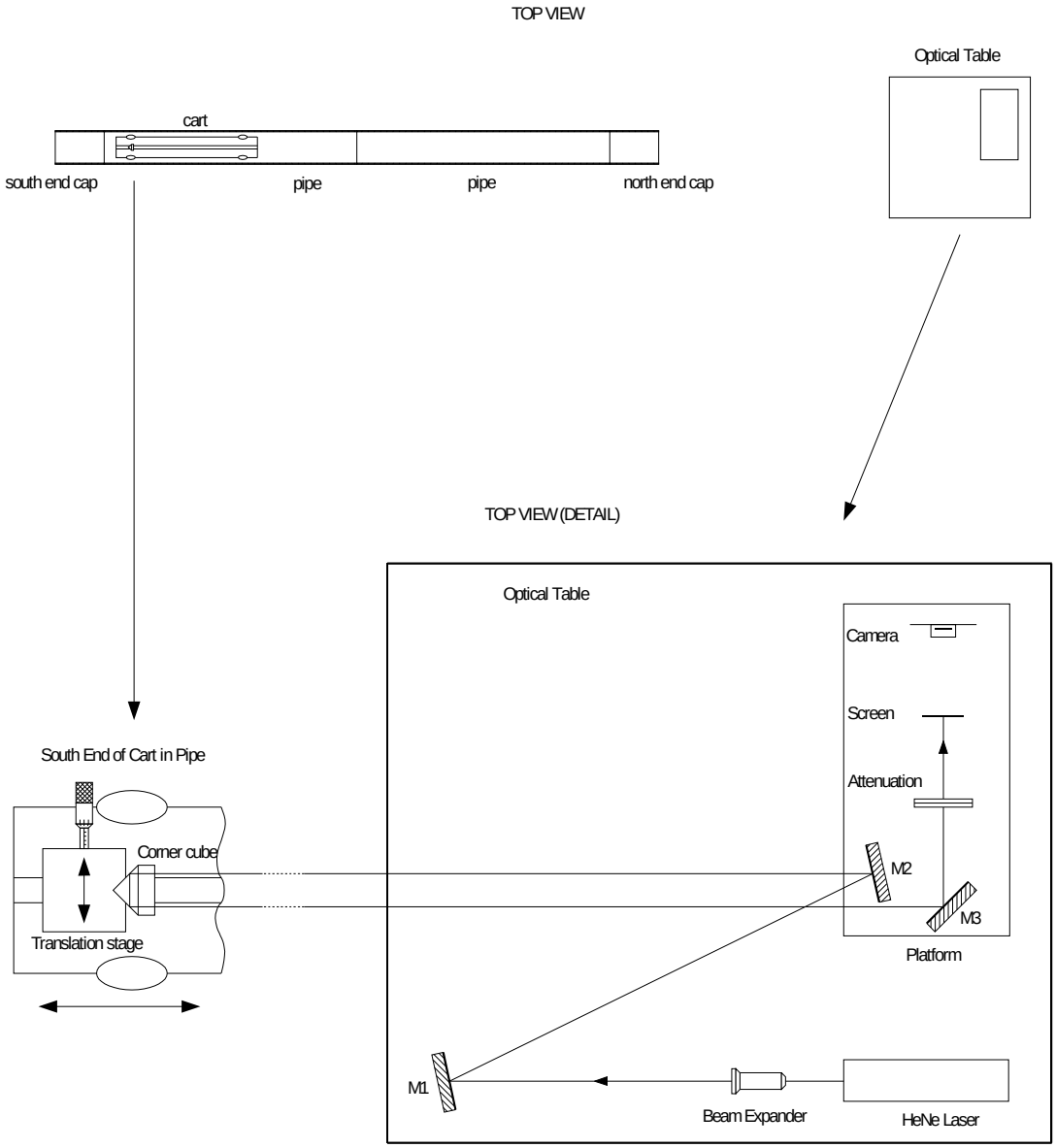

Figure 4.1: Top view of the trajectory experiment hardware. A corner cube is mounted above a wheel pair of the cart, which is then placed inside the pipe test rig. The rig is oriented north-south. An optical table is located to the north of the rig and supports a laser and optical and electronic components for beam shear measurement.

- The light is returned by the corner cube, which is mounted on a translation stage above one wheel pair of the cart (Figure 4.2). At the time these tests were done, the cart was simply pulled through the pipe using string attached to either end. String was also used to construct buffers at each end of the pipe to prevent accidental overruns.

  Lateral translation of the corner cube causes the return beam shear to change by exactly twice the corner cube displacement, so as the cart is moved along the pipe, variations in its lateral displacement with respect to the incoming beam axis can be determined. The translation stage can also be shifted laterally using a micrometer gauge and this is used to calibrate a shear sensor.
- The return beam from the corner cube is reflected off mirror M3 and is attenuated by a pair of polarisers before landing on a screen. The spot position on the screen changes according to the

Figure 4.2: The corner cube on its translating stage (left) which in turn is mounted above a wheel pair at one end of the cart in the pipe (right). The corner cube overhangs the stage so that its optical centre is as close to the centre of the pipe as possible – this reduces the effect of cart clocking on the beam shear measurement.

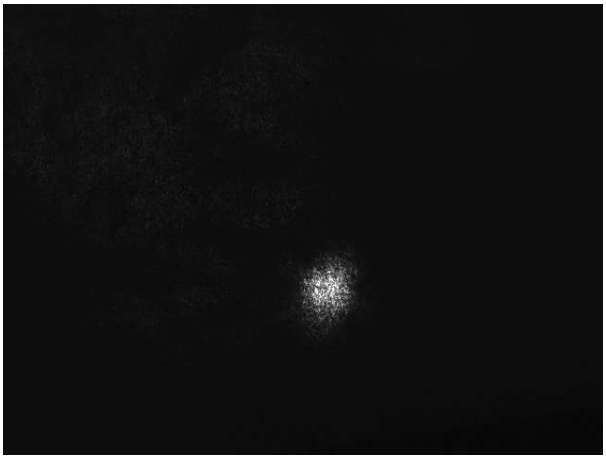

Figure 4.3: An example of a laser spot imaged by the camera. The "graininess" in the image is due to laser speckle.

beam shear induced by lateral movement of the corner cube.

- A camera and computer software calculate and record the centroid of the spot for future processing. They constitute a "shear sensor" that potentially could be used in the MROI delay line shear minimisation feedback loop. The camera is an IEEE-1394 digital video device (Unibrain Fire-i BBW 1.3) with a 640×480 pixel 8 bit monochrome output at 30Hz and a lens focused on the screen. An example of a laser spot imaged with the detector appears in Figure 4.3.

The laser beam could have been sent through a reversed beam expander directly onto the camera CCD rather than being reimaged via a screen, but the screen allowed the image size to be changed simply by adjusting the distance to the camera and refocusing. It also may have assisted in reducing the effects of laser speckle.

Custom software in Linux performs display of each incoming frame and real-time calculation and recording of the spot centroid. The program uses a simple "centre of gravity" algorithm with the modification that the lower half of the range of intensities is set to zero to eliminate the noise floor. This method was chosen for its simplicity of calculation and immunity from effects likely to be encountered by an MROI shear sensor, such as variable spot size and intensity as well as diffraction rings with diameters dependent on optical path distance. It was found to work very well and also proved to be immune

to the effects of laser speckle.

The output of the program is the centroid position in pixels from the corner of the sensor calculated at 30Hz (the camera frame rate). This is well in excess of the 2Hz bandwidth that the MROI cart secondary mirror servo is expected to require.

4.2.2 Experimental Procedure

The experimental procedure consisted firstly of establishing a pixel scale for the beam shear and then recording the shear as the cart was manually drawn along the pipe.

- To make measurements of the physical cart displacement it was necessary to calibrate the pixel scale of the camera. The cart was held at the south end of the pipe (as far as possible from the optical table) and the micrometer was used to move the corner cube in 0.25mm steps. The centroid position as measured by the camera and computer was noted for each step.

  The procedure was repeated with the cart at the north end of the pipe as a check that the beam shear calibration was independent of the optical path distance used. However, the micrometer was not accessible in this configuration so it became necessary to send the cart back to the south end each time a micrometer adjustment was required. Hence there was potential for the north measurements to be affected by clocking of the cart during transit, although the corner cube axis was intentionally placed as close as possible to the pipe axis to minimise this. Clocking was indetectable by visual inspection of the cart wheel positions (certainly less than a millimetre) and was reduced by a factor of ten or more at the corner cube.

  Once the readings were completed, lines were fitted to the results to calculate the pixel scale, in millimetres per pixel, at each end of the pipe.

- Having calibrated the detector and set up the apparatus for recording of centroid positions, two experiments were performed:

  1. The shear sensor was set to record centroids at 30Hz and the cart was pulled through the pipe at as constant a velocity as could be managed by hand. The readings could not be associated with distances along the pipe due to the uncertain velocity, but measurement of the range of shear deviations along the pipe length could be achieved. Furthermore, the high sampling rate allowed fine details in the trajectory structure to be seen.
  2. To provide more certainty as to the spatial distribution of the shear along the pipe, one of the strings used to pull the cart was marked in 5cm intervals. The cart was then pulled through to each mark, stopped, and a centroid reading taken, until the cart had traversed the length of the pipe. A second, trailing, string was routed through a retort stand to provide retarding friction so that the measuring string tension was approximately constant. Hence the markings were evenly spaced throughout the pullthrough and the results could be scaled to fit the length of the pipe. A more accurate distance measurement than the one in experiment 1 could be achieved this way at the cost of reduced resolution. Comparison of the two datasets could be used to achieve a more complete view of the beam shear, and the second dataset could also be used to calculate the pitch and yaw of a hypothetical MROI cart with an assumed wheelbase of 1.8m (the cart length is expected to be about 2m).

An attempt was also made to collect data with the cart at a constant roll angle of 5° to the horizontal to discover the effect of cart clocking on shear. However, on retrieval the cart was found to have rotated to a horizontal position during transit. Hence it was not possible to make this measurement, but the

tendency of the cart to move to a horizontal position without active steering is encouraging in terms of overall cart dynamics.

4.3 Definition of Success

From the introduction, the MROI cart trajectory can deviate from a straight line by up to $\pm$5mm if the secondary is active. A cart tilt (a pitch or a yaw) of up to 3.3mrad can also be tolerated (for a 1.2m focal length catseye primary mirror).

Recalling that the deviation of the spot centre on the screen (the shear) is twice the axial displacement of the corner cube, if the envelope of return spot positions over the entire pipe length fits within a circle of radius 10mm then the shear criterion is met. Assuming a 1.2m focal length catseye primary mirror, if the cart tilt does not exceed 3.3mrad then the tilt criterion is met. If both criteria are met, the optical fidelity is sufficient to allow us to proceed with the "cart in pipe" concept.

4.4 Results

4.4.1 Calibration

The pixel scale of the cart was determined for both the southernmost and northernmost positions of its travel. In both cases, the corner cube was translated over a total of 3mm in 0.25mm increments and the centroid position was recorded. Although the change in shear was mainly in the horizontal as intended, there was also some vertical motion which indicates that the camera was not perfectly aligned with the plane of the corner cube motion. Accounting for the vertical as well as the horizontal displacement and making use of the fact that the detector has square pixels, these data yielded a pixel scale of 0.0267mm/pixel at the south end and 0.0269mm/pixel at the north end — that is, the shear measurement was essentially independent of longitudinal cart position as it should be, and there were no obvious effects due to cart clocking. These values are based on corner cube displacement and must be doubled to calculate beam shear.

4.4.2 Manual Cart Movement

Two manual tests were undertaken. The first involved centroid recording at 30Hz during an approximately constant-velocity cart pullthrough and the results are shown in Figure 4.4. This chart shows the raw data. It is tempting to subtract a line of best fit so that only the deviations from some ideal physical line are shown, but this requires knowledge of the cart position at each sample time — information that can only be guessed at due to the uncertain cart velocity.

The second test used centroid measurement at each of many equally spaced cart positions (nominally 5cm apart) along the pipe and is summarised in Figure 4.5. In this case, the cart and corner cube positions are well known and lines of best fit have been subtracted from the data to reveal the deviations from an ideal line. The corner cube position on the cart cannot be moved closer than 100mm to the south end of the pipe or closer than 1.6m to the north end because the cart is confined within the pipe and hence shear measurements have only been made between those two bounds.

Finally, the data used to produce Figure 4.5 were used to calculate how a hypothetical MROI cart with a wheelbase of 1.8m would tilt (pitch and yaw) if it were to run along this pipe. The results are plotted as a function of the midpoint position of such a cart in Figure 4.6.

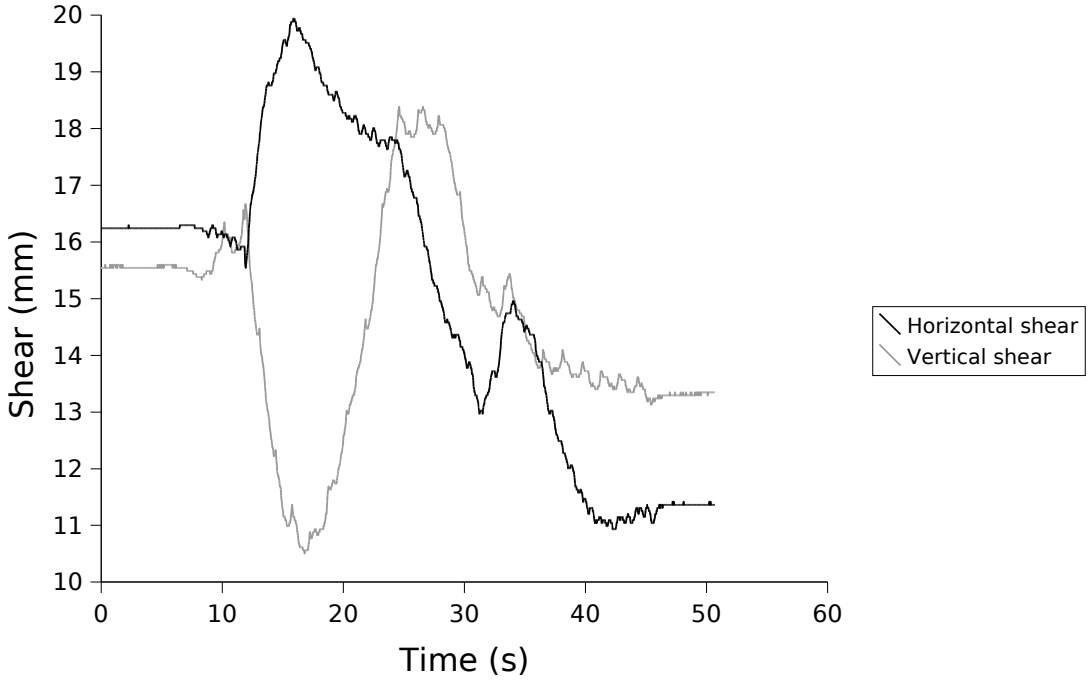

Figure 4.4: Measured beam shear deviation as a function of time during a manual cart pullthrough. The data has not had a line of best fit subtracted.

4.5 Discussion

4.5.1 Cart Trajectory

Figure 4.5 shows that the horizontal and vertical shear ranges are 6mm and 8mm respectively. These figures are well within the MROI specification of $\pm$10mm maximum beam shear with an active secondary, so *a cart with an active secondary using industrial aluminium pipe as an enclosing support mechanism meets the shear requirement*. Furthermore, the data overestimate the shear as no attempt has been made to optimise the cart trajectory by straightening the pipes with respect to each other. Even in Figure 4.4, where there are still residual slopes in the data, the deviation in both axes is $\pm$5mm and the MROI specification is still not exceeded.

Looking further into the data, there are slowly varying shear deviations, attributable to pipe deviations, of several millimetres along the run. The change in pipe gradient at joins is also obvious in Figure 4.5 — the cart's shear-minimising servo will need to have sufficient bandwidth to deal with such changes.

In terms of higher spatial frequency data, Figure 4.4 shows periodic spikes of magnitude $1/4$ to $1/3$ of a millimetre in the vertical. These are caused by the cart wheels, which were flat on part of the rim due to the cart having been left in one position for several days before the tests were done (the inline skate wheels were the ones used). The total introduced shear is small, but could be reduced further by:

- introducing a mechanical scheme where the cart does not rest on its wheels when it is not in use.
- exercising the cart continuously so that flat spots do not develop.
- using a different material for the cart wheels.

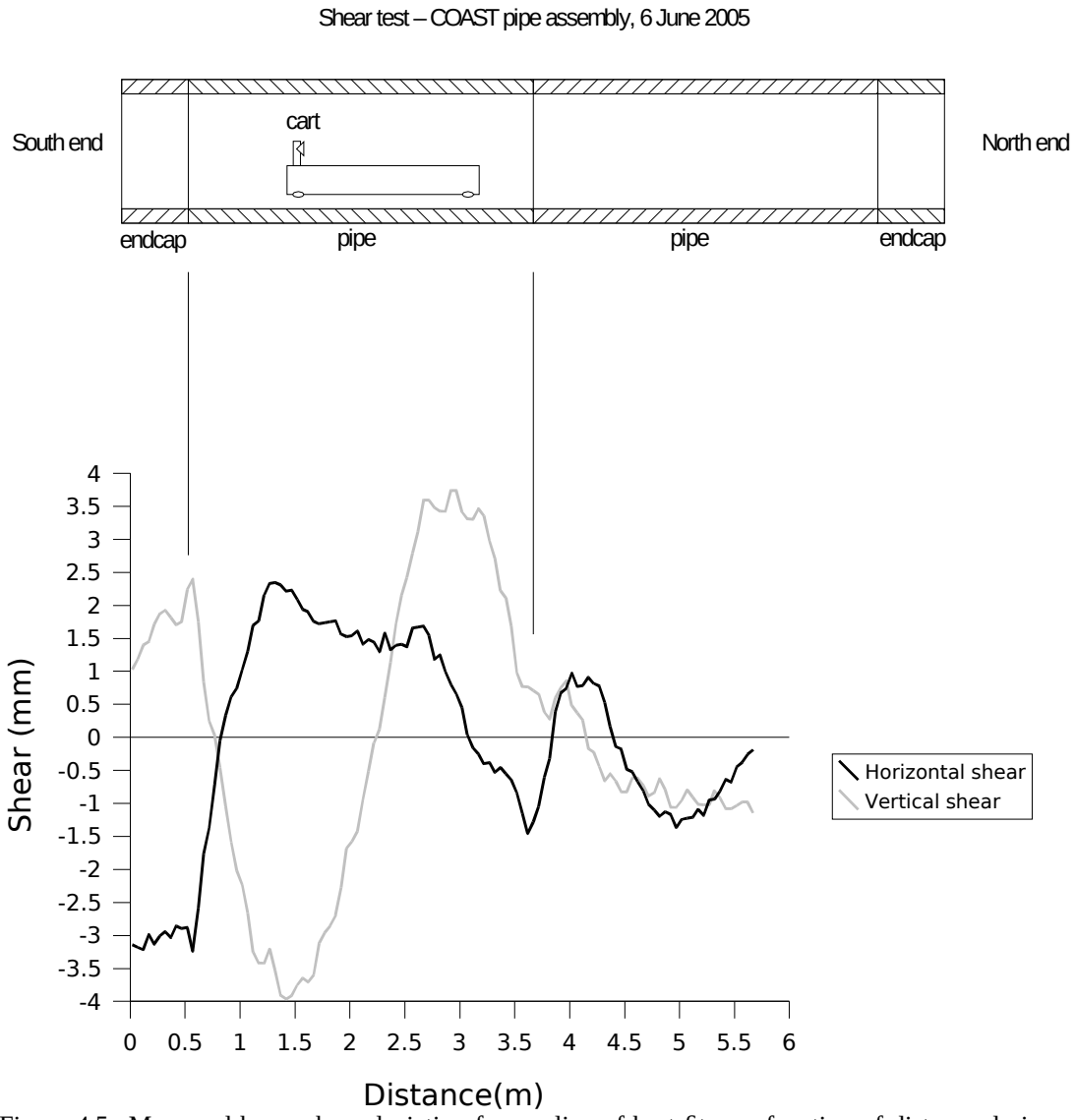

Figure 4.5: Measured beam shear deviation from a line of best fit as a function of distance during a manual cart pullthrough, with a drawing of the cart in the pipe so that physical test rig features can be referenced to features in the data (the horizontal scales have been matched).

4.5.2 Cart Tilt

It can be seen from Figure 4.6 that for a cart with a wheelbase of 1.8m, the yaw is always less than 1.4mrad and the pitch is always less than 2.1mrad. These are both within the requirement of 3.3mrad for a cart with a 1.2m focal length primary. So *a cart with an active secondary using industrial aluminium pipe as an enclosing support mechanism meets the tilt requirement.*

4.5.3 Comparison with Mechanical Data

It is also instructive (and a useful validation) to compare the shear measurements with measurements made of the exterior pipe surface. When the pipes were sent to an industrial firm for machining, the deviation of the exterior surfaces was measured by mounting the pipes on a machining bed and tracking a gauge along the lengths in two orthogonal directions. The gauge readings were marked on the pipe in

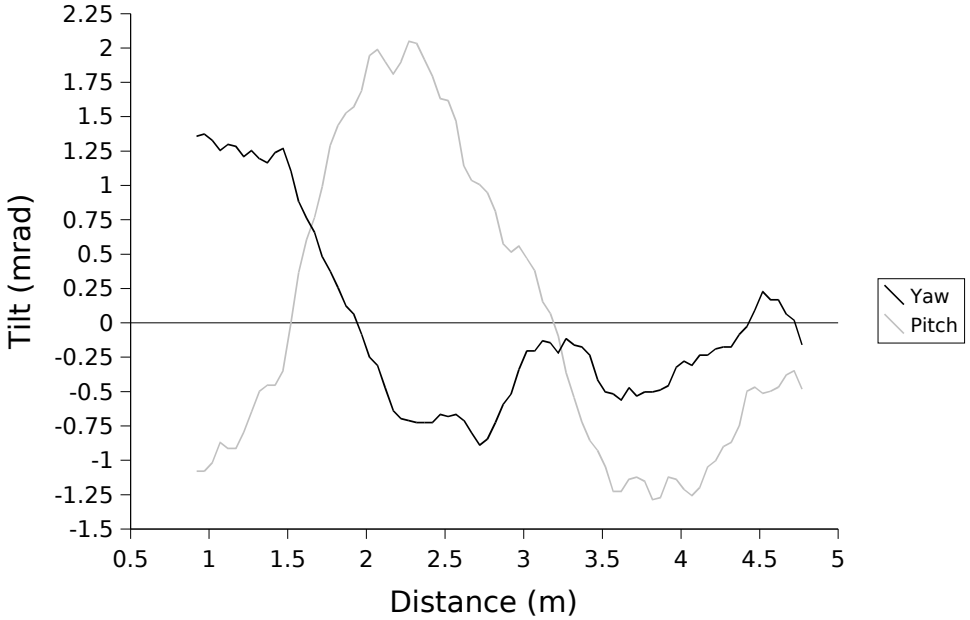

Figure 4.6: Pitch and yaw of a hypothetical MROI cart with a wheelbase of 1.8m as a function of the cart midpoint position, if it were to run along a pipe with deviations as measured in Figure 4.5.

the positions where they were made and are still visible on the test rig. The values and positions in the current pipe orientation are summarised in the top part of Figure 4.7.

The bottom part of Figure 4.7 compares these mechanical readings with the beam shear measurements. Because the mechanical and optical data most likely are referenced with respect to slightly different measurement axes, for comparison the mechanical data and extracts from the shear data spanning each pipe have again had linear best fits subtracted from them. This allows the deviations from straightness to be compared. Also, the mechanical data for the southernmost pipe are oriented at approximately 45° to the horizontal and vertical and have been interpolated assuming a perfectly round pipe. Finally, the mechanical deviations have been doubled to produce a "prediction" of the shear measurements.

For the externally measured mechanical data and the internally measured optical data to agree, the pipes should be perfectly round and of constant cross-section along the length. The data show that this condition is approached but not met – the mechanical measurements are good predictors of the overall cart trajectory to within about a millimetre (the discrepancy is most likely a result of the pipe extrusion process and subsequent handling). Provided that this variation is allowed for, such mechanical measurements might be useful during the MROI construction for rejecting excessively bent pipes or for orienting the remainder so as to minimise cart deviations from a straight trajectory.

4.5.4 Shear Sensor Performance

The aim of these tests has been to evaluate the cart trajectory, but the collected data can also be used to evaluate the feasibility of the digital video aquisition method when applied to MROI metrology shear detection.

Calculations for the MROI metrology beam (Chapter 9) show that the diameter of the region in which the intensity is greater than $1/e^2$ of the maximum will be $\sim$20mm. The tolerance on the actively compensated metrology shear is $\pm$1mm, so the sensor precision must be better than $\pm$5% of the beam diameter.

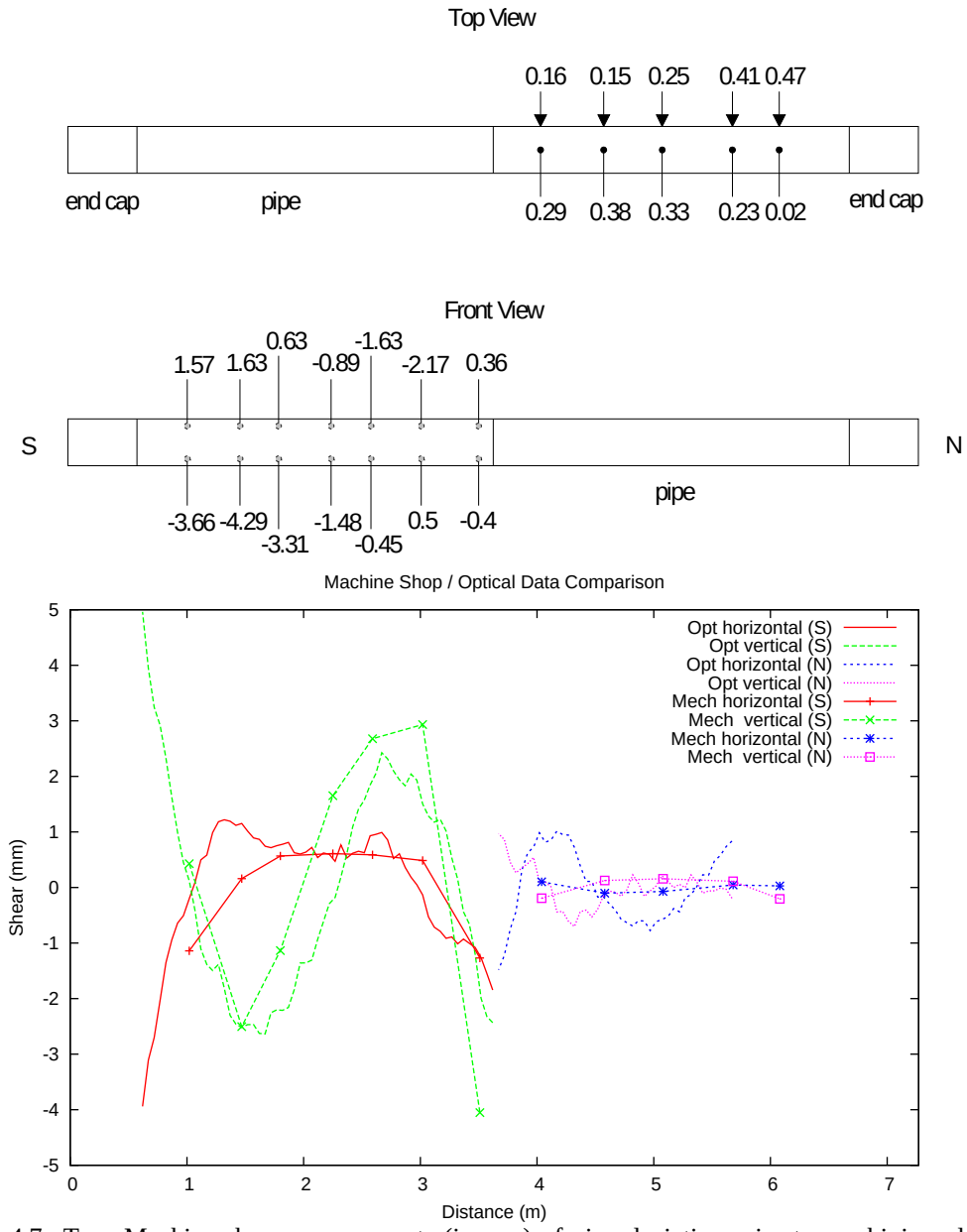

Figure 4.7: Top: Machine-shop measurements (in mm) of pipe deviation prior to machining, drawn in their measurement positions and to scale so that they can be compared with the beam shear measurements. The arrows designate measurements made on the side of the pipe. In the front view, the measurements are all made on the far wall of the pipe. Bottom: The machine-shop measurements compared with extracts from the shear data spanning each pipe. All datasets plotted here have had the linear best fit subtracted and the machine-shop measurements have been doubled to allow comparison with the shear measurements.

Inspection of Figure 4.4 shows that for those periods when the cart is not in motion (when the time is less than 8 seconds or more than 47 seconds) the noise in the centroiding measurement is roughly ± 1 pixel. The beam diameter in Figure 4.3 is approximately 50 pixels, which implies a precision of $\pm 2\%$, already better than the MROI requirement. Furthermore, the sensor used for these trials is an array of 640×480 pixels, so one might imagine choosing optics at the MROI which map the spot onto the central 400×400 pixels of the array (the servo could then be started even when the open-loop beam shear was the specified maximum of 10mm, as part of the beam would still be in the field). The expected precision then becomes $\pm 0.25\%$, comfortably exeeding what is required. If further precision proves necessary there are many IEEE-1394 cameras with larger pixel arrays (but often at a reduced frame rate).

4.6 Conclusion

These experiments have established that the beam shear in the pipe sections under test at COAST is much less than ± 10mm and the cart tilt is less than 3.3mrad (for a 1.8m wheel base), within the MROI requirements if the MROI carts have active secondaries. Therefore *it appears that the cart trajectory and tilt will be within MROI tolerances using the "cart within an evacuated pipe" concept provided that an active secondary mirror is used.*

Furthermore, in the course of development of this experiment a cheap and effective technique for monitoring beam shear (the use of digital video) has been found which can be scaled to the detection section of the MROI beam shear servo itself. The flexibility of this method could also make it useful in many other parts of the MROI where low bandwidth alignment feedback is required.

Chapter 5

[002-04] Control and Communication

Principal risks:

That it may prove difficult to implement suitable high bandwidth links to communicate with and control the delay line trolley over a distance of 656 feet in an evacuated pipe.

5.1 Aim

To establish the feasibility of RF links both to close the cat's eye servo loop and the general cart control.

The cat's eye servo loop requires a low latency link to maintain the necessary loop bandwidth.

5.2 Method

Three separate experiments were carried out:

1. To replace the hardwired servo link for the COAST trolley with an RF link.
2. To investigate commercial devices for the cart control loop.
3. To measure the characteristics of RF signals in our proposed delay line pipes.

5.2.1 Description of apparatus

Servo loop tests

The core of the experiment are Radiometrix transmitter and receiver modules, TX3A and RX3. These are miniature FM UHFradio transmitter and receiver designed for PCB mounting. The transmitter is 12mm×32mm×3.8mm and the receiver is 17.5mm×48mm×4.5mm. Both require less than 0.1 watt power. They are intended for for data links up to 64kbps but have DC coupled inputs and outputs, unlike many other devices on the market, intended for FM radio/audio links. There is a European version at 869.64 MHz and a USA version at 914.64 MHz, both licence free.

The modules (European versions) were mounted on PCB together with other components and mounted in die cast boxes, the connectors and cabling designed so that they could simply be inserted either end of the existing ribbon cable that is used on COAST to carry both the control and analogue servo loop signal from the control computer to the moving trolley.

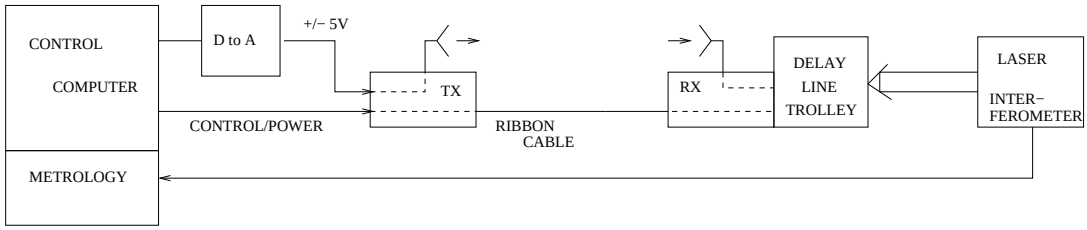

Figure 5.1: Diagram of COAST trolley servo loop.

Cart Control

In view of the need to keep cart power to a minimum, an Arcom Viper PV/104 single board computer was chosen. This is ultra low power (2 Watts) and is based on an Intel 400MHz PXA255 XScale processor. It includes 10/100BaseTX Ethernet, USB, Digital I/O, 5 Serial ports and a Type I/II CompactFLASH socket. Arcom supply an embedded Linux which is a space optimized distribution that includes many standard Linux features such as ssh, telnet and ftp. It also includes wireless support for the popular PRISM chip set and a Linksys Wireless CompactFlash card (WCF12) was installed as one end of the RF link. The "sending" end of the RF link was a D-Link Ethernet wireless bridge (DWL-810+).

These devices operate at 2.4 GHz and conform to the standard 802.11b and were configured to work in the "ad-hoc" mode (single point-to-point).

Pipe attenuation

This was measured using a HP signal generator sending a known signal to aerials mounted on the end plate of the pipe and using a spectrum analyser connected via a long coax to similar aerials mounted on our embryo cart.

5.3 Experimental Procedure and Results

5.3.1 Servo Loop Test

The experiments were mostly conducted on trolley 3 at COAST using internal fringes.

The procedure was to set up trolleys 1 and 3 to obtain internal fringes with both trolley servos hard-wired as normal (internal fringes are obtained by changing the path length of one arm of the interferometer. This is done by applying a saw tooth waveform to the trolley servo). The fringe amplitude was recorded together with the trolley position (metrology data). The RF link was then inserted and similar data recorded together with DC levels at the output of the RF link.

Figure 5.2 contains plots of the fringe data with and without the RF link, both with trolley 3 sweeping and stationary. The width of the power spectrum fringe peak is the same in both cases, but there is a slight increase in the power in the wings. Apart from this, the COAST trolley behaved exactly the same with and without the RF link.

Figure 5.3 shows plots of the servo loop error output based on the metrology data. The top two plots are without the RF link and the bottom two are with the RF link. These show that the loop noise is three times that for the hard wired system and further investigation showed that this increase is due to noise in the receiver discriminator output. The noise level depends on the limiting characteristics of the receiver

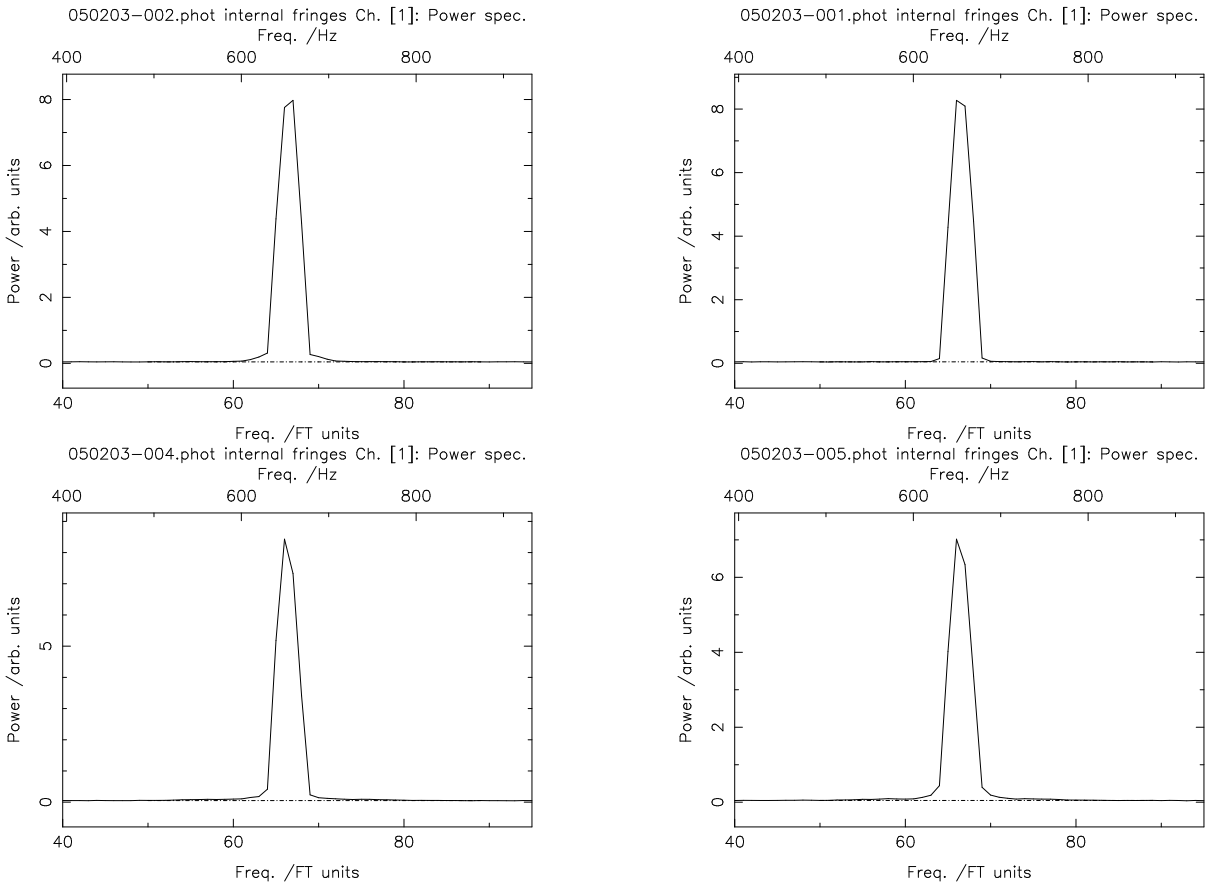

Figure 5.2: Averaged fringe power spectra with (bottom) and without (top) the RF link, both with trolley 3 sweeping (left) and stationary (right).

and generally does not change greatly providing the signal power is adequate. Figure 5.4 shows a typical noise power plot of discriminator output with a signal power level of -45 dBm. Reducing power level by 10dBs only increased RMS noise level by 0.1 mV. Providing the input signal level is kept between -20 and -50 dBm the peak to peak noise level in a 5kHz bandwidth will be less than 5 mV, equivalent to 20 interferometer counts peak-peak or 0.05 microns trolley displacement. (c.f. hardwired figures of 7 counts p-p and 0.017 microns) Note that the nominal power output of the transmitter is 0 dBm and the overload power level for the receiver is -10 dBm.

Loop Stability

The data sheets for the receiver state that the discriminator output is nominally 200 millivolts peak-peak requiring a following amplifier gain of 25 to give the same output as at COAST (5 volts p-p). However measurements of the discriminator output showed that the linear range was 500 millivolts p-p requiring a gain of 10. Any drifts in frequency with time or temperature will produce a DC offset at the discriminator output and cause a shift in trolley position and reduce the range of the servo loop. During the various servo tests the DC offset was noted. At switch on the output was adjusted to zero and after 20 mains the offset was 0.5 V (5 % of the total servo loop range and an offset of 0.25 micron) and thereafter drifts were less than 0.1 V.

A separate test was carried out to check drifts against temperature and the results are shown in Table 5.1.

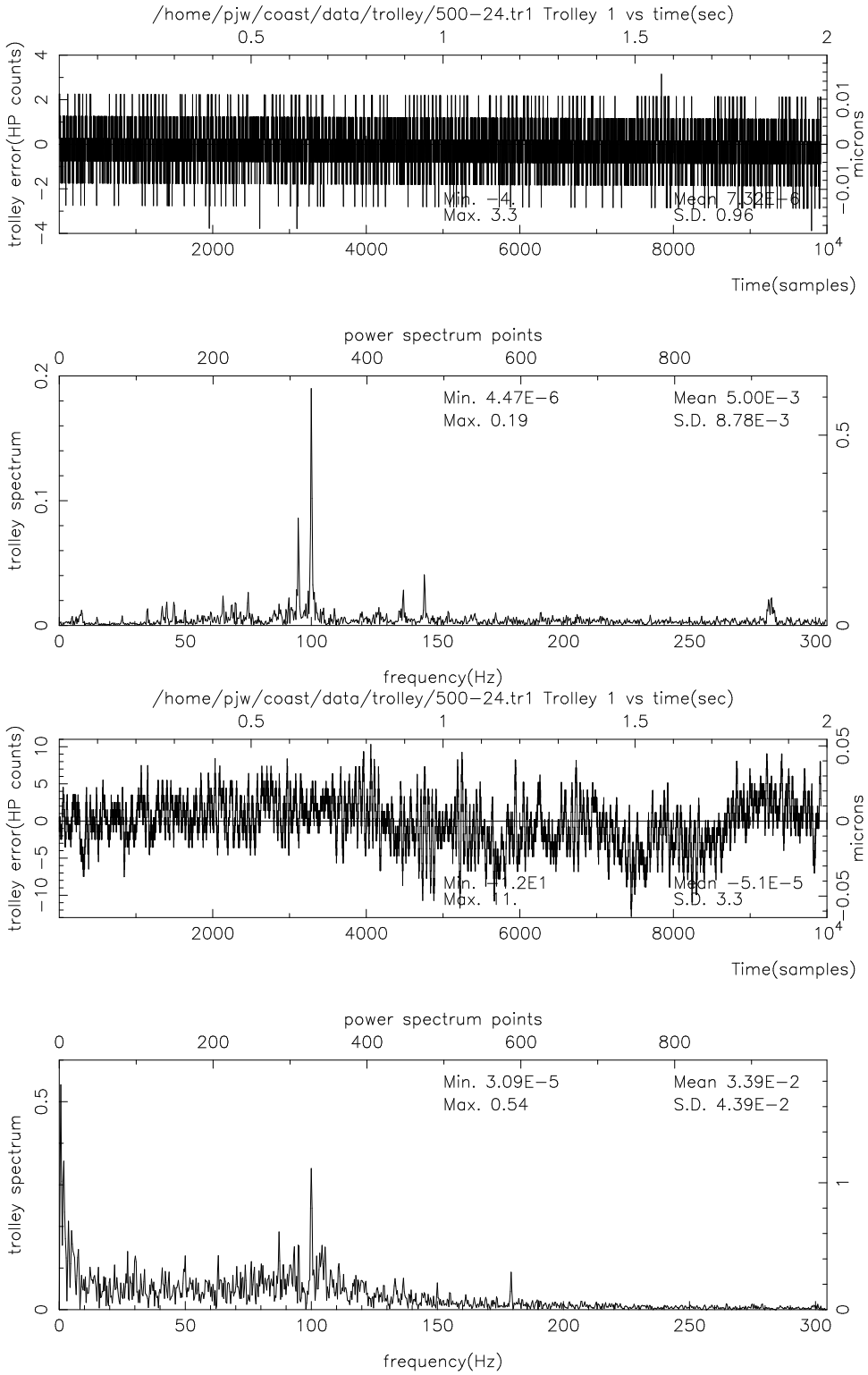

Figure 5.3: Plots of COAST trolley servo loop errors and derived power spectra, from metrology data. The top two plots are without the RF link and the bottom two are with the RF link.

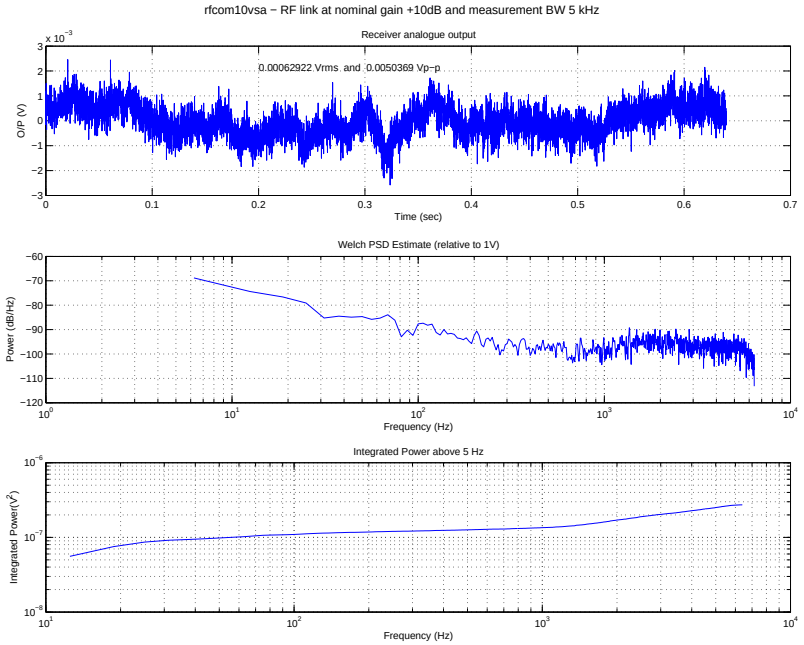

Figure 5.4: Noise power plot of RF receiver discriminator output, with a signal power level of -45dBm.

Table 5.1: Drifts Against Temperature.

Temperature	Offset voltage
11.3	0.05
12.8	0.2
13.8	0.316
17.7	0.6

The variation of offset with temperature is approximately 0.1 volt (0.05 microns) per degree change.

5.3.2 Cart Control

The embedded Linux software for the wireless link was straightforward to configure and started automatically when the embedded micro booted. Telnet and FTP all worked as expected. If the RF link was lost for a time it recovered automatically when restored.

5.3.3 Pipe attenuation

The pipe ($D = 0.37\,\text{m}$) can be considered as a circular waveguide and the cut off wavelengths and frequencies for various modes are shown in Table 5.2.

In fact the TE_{01} mode is easy to generate with a simple 1/4 stub aerial at the end of the pipe and a similar aerial on the cart. For the TE_{01} mode, minimum attenuation occurs when wavelength is 0.58 of critical wavelength. At 900 MHz (0.68 critical wavelength) the attenuation is 4×10^{-3} dB/m for copper waveguide.

A diagram of the aerial arrangement is shown in Figure 5.5.

Table 5.2: Cutoff wavelength and frequencies in a circular waveguide of diameter $D = 0.37$ m.

Mode	Wavelength	Frequency
TM_{11}	$1.71D$	472 MHz
TE_{01}	$1.31D$	617 MHz
TM_{01}	$0.82D$	986 MHz

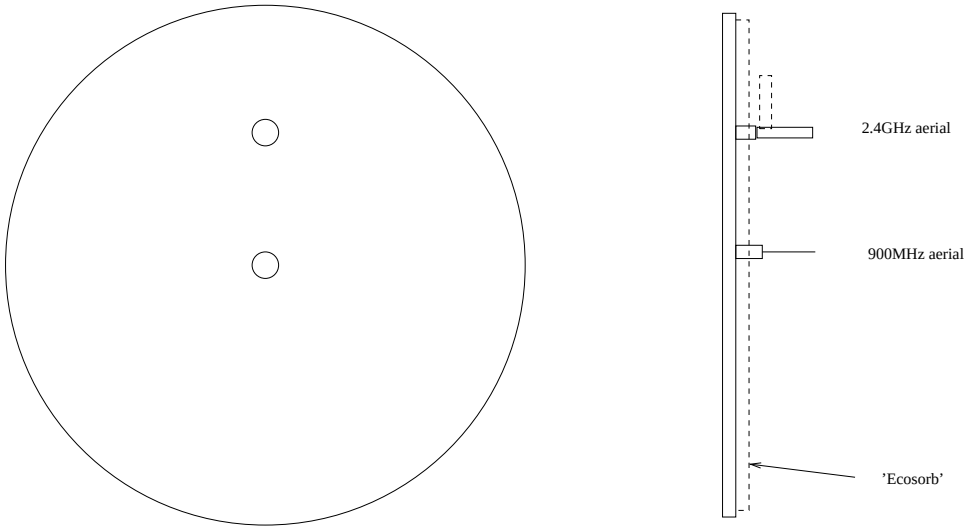

Figure 5.5: Arrangement of aerials on both end plate and plate attached to cart.

The match of the aerials was checked on a network analyzer. Return losses are shown in Table 5.3. Note that return loss is a measure of the efficiency of the aerial — the lower the return loss the better the efficiency.

The attenuation at 900MHz varied between 0.4 dB and 8 dB in a regular pattern as the cart was moved along the total length of the pipe indicating that there was a standing wave present but there is no measurable attenuation over the 7 m of the pipe. The receiver's dynamic range would easily cope with this variation but a better designed and matched aerial would reduce the standing wave.

At 2.4 GHz there was a pattern of reflections (attenuation varied between 9 dB and 27 dB) and Ecosorb was used at both the pipe end and on the cart to reduce reflections. The variation in loss was then only 2 dB and the overall loss over 7 m of pipe was 4 dB. These tests were carried out at one fixed frequency but the standard 802.11b system uses direct spread spectrum sequence (DSSS) which spreads the transmission signal over a broad band of frequencies and will reduce the effect of any signal nulls.

Table 5.3: Return losses for two aerials.

Frequency	Loss
900 MHz	-10 dB
2.4 GHz	-33 dB (right angle to plate)
2.4 GHz	-22 dB (parallel to plate)

5.4 Discussion

The tests on COAST have established that the servo control of the cats eye mirror can be closed using a UHF transmitter and receiver at around 900 MHz and maintain the necessary bandwidth. The devices used in this experiment do introduce some noise into the loop which alters the shape of the "wings" in the power spectrum of the fringes. However, this does not significantly affect the signal-to-noise ratio of the fringe measurement. It should be noted that these are cheap devices and better devices/systems may be available.

Stability does not seem to be a problem as the reduction in servo range is less than 5% and any DC drifts, which alter the catseye position, are much less than the expected variation in path length from night to night.

As a fallback option, we also considered closing the servo loop with a digital link. The problem with most commercial systems is the latency involved in sending packets. We did find a Chipcon device CC2400 (a 2.4GHz digital transceiver IC) and a pair of demonstration boards were purchased (each containing a CC2400, a programmable microprocessor and sample code). They were programmed so that four data bytes and a two byte cyclic redundancy check could be sent over the link as a data packet at 1MHz. The latency was found to be 160μs which coupled with the metrology calculation on COAST of 22μs would not be satisfactory on COAST without considerable reduction in the loop gain. However, the MRO delay line cart will not be required to modulate the OPD (this will be done elsewhere) so a lower bandwidth would be acceptable. We are continuing to investigate using these devices in an unbuffered mode where latency would only be 24μs for a 16-bit data byte.

The attenuation measurements show that at 900 MHz the loss is low as predicted by waveguide formula (the 0.4 dB attenuation is probably due to poor aerials) The variation in attenuation would be reduced with better matched aerials.

With the rapid advance of WiFi there will be no problem with commercial devices using Ethernet/TCPIP to communicate. The free space range for these devices is in the range of 350 m (for a 1 Mbit data rate) and the dynamic range is 100 dBs. It is not realistic to extrapolate the 4 dB attenuation measured over 7 m to 200 m as this figure includes aerial losses and lack of forward gain. In any case there are many modes of propagation in a pipe of this size at 2.4 GHz. There have been studies carried out to demonstrate the feasibility of using heating and ventilation ducting in buildings to broadcast 2.4 GHz for WiFi and these systems use multiple transmitting and receiving aerials. This would be a fall back option if single high gain aerials were insufficient.

Chapter 6

[002-05] Power Transmission

Principal risks:

That it may prove difficult to deliver power to the delay line trolley over its expected 656 foot travel for two reasons:

1. *The power delivered may not be stable, leading to unreliable operation*
2. *That losses in the power transmission mechanism may lead to failure to meet an overall power budget.*

6.1 Aim

To demonstrate that adequate power can be transferred inductively to the moving trolley from an insulated induction wire via a slim transformer which will fit under the trolley and cause minimum mechanical drag and wear with no risk of snagging.

6.2 Method

A simple trial system following the diagram in Fig. 6.1 was constructed to fit on one of the existing COAST PC trolleys as shown in Fig. 6.2.

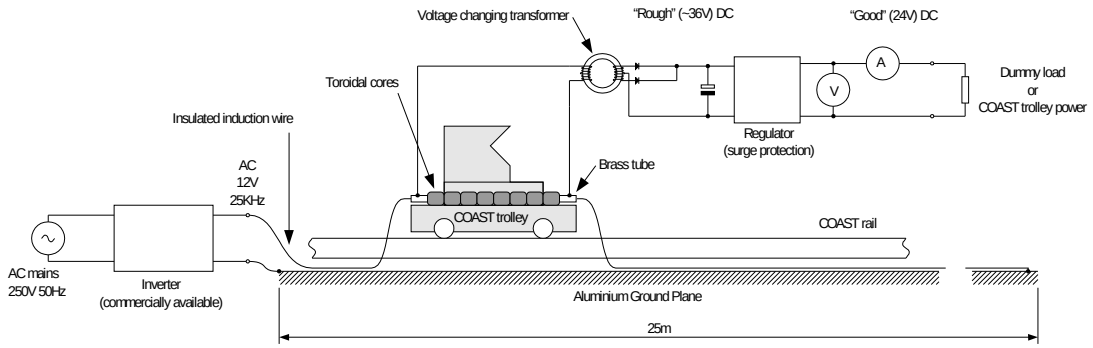

Figure 6.1: Schematic of trial inductive power system for COAST trolley.

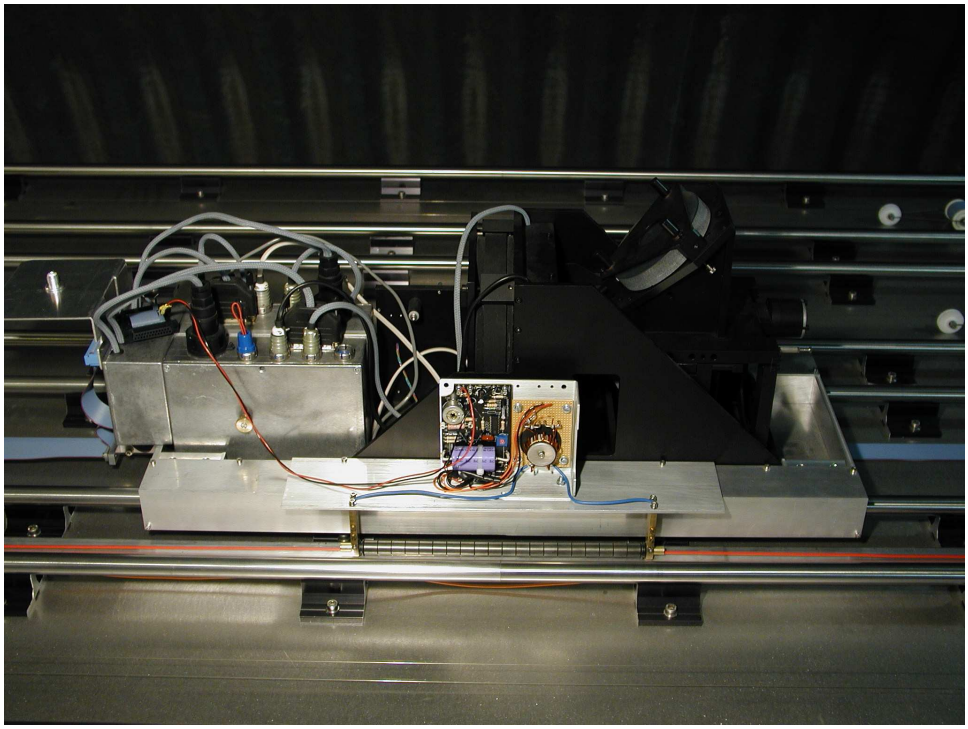

Figure 6.2: Photograph of COAST trolley with inductive power transfer pick-up fitted.

The induction wire is the orange wire visible above the nearest rail in the picture. It normally rests on the aluminium substrate beneath, but a short length is raised a small distance by the passage of the trolley mounted pick-up transformer, which consists of a series of 20 ferrite toroids mounted on a thin brass tube. The tube supports the cores, guides the wire and also serves as the single secondary turn of the transformer.

Above the mounting plate can be seen the toroidal voltage changing transformer and rectifier diodes, and the (linear) output voltage regulator.

The performance of this system was tested electrically and mechanically as follows.

6.3 Tests

6.3.1 Mechanical

The drag effect of the system on the trolley was assessed in two ways, firstly by attempting to measure the actual drag by towing the trolley with a spring balance. The extra drag was almost impossible to measure as it was less than the variation in drag without it (without the inductive pick-up a force of $1.00 \pm 0.05\,\mathrm{N}$ is required to overcome rolling resistance, with the pick-up fitted $1.10 \pm 0.05\,\mathrm{N}$ is needed). Secondly the trolley was used in the normal way to follow moving fringes and no change in performance was detectable.

6.3.2 Electrical

The electrical performance of the system was also tested in two ways. Firstly dummy loads were connected to the output until ripple and voltage drop (of $\sim 0.1\,\mathrm{V}$) became apparent which occurred at a load

of 17 W, independently of the trolley position along the rails. This is more than the COAST trolleys need (they require ~ 2.5 W when stationary or tracking, and ~ 5 W when slewing). Secondly the system was used to supply the trolley while it was tracking at about 1.4mm/s, and no change in performance was detectable in the COAST metrology data (Figure 6.3).

We anticipate that the MROI trolleys will each need < 5 W, except for slewing which will require at least 15 W. Hence the 17 W achieved with the trial inductive system will be sufficient for the MROI trolleys, except possibly for slewing. As explained in Section 6.5, it would be straightforward to modify the trial system to deliver 24 W.

6.4 Limitations

These trials used a very simple inverter (a standard electronic low-voltage lighting transformer) to drive the induction wire, with no attempt to vary its output according to the load or remove 100 Hz ripple, Only a linear regulator (from a modified mains power module) was used on the output, so marked improvements in efficiency and power output should easily be obtainable.

The trials were carried out with the induction wire lying on a $\frac{1}{2}$ inch thick aluminium substrate to simulate the bottom of the proposed vacuum pipe. If the wire lay instead on the (magnetic) stainless steel top of the COAST PC table its impedance was far too high and lossy to transmit useful amounts of power.

6.5 Extrapolation

The test track at COAST is only 24 m long, whereas the track at MROI will be 200 m long. The major limiting factor to the power transfer is the impedance of the induction wire which will be over 8 times as high, but this can easily be overcome by using a higher voltage system. The trial system uses a nominal 12 V and increasing this to the still safe value of 36 V would allow for an impedance 9 times higher. This would only involve using a pick-up transformer 3 times as long as the trial one and changing the other tranformer ratios. The suggested changes would have no system-level impact.

The inverter used produces nominal 12 V r.m.s. running on unsmoothed rectified 50 Hz. If a DC powered inverter was used the power output would be increased by 40%, bringing the 17 W achieved in the trials up to 24 W.

As these tests were carried out using a 1/2” thick aluminium substrate to simulate the pipe bottom, and as the magnetic field due to the induction wire is contained in a very small volume round it as a result, it was decided that there was no point in going on with the other proposed test of actually delivering 24 W to a trolley in our rather short test pipe run.

6.6 Conclusions

We have demonstrated that adequate power for the MROI PC trolleys can be safely and reliably transmitted by means of a non-contacting inductive transfer system which causes very little friction (and hence little wear), and is not susceptible to looping or snagging of trailing cables. This presupposes a high conductivity non-magnetic vacuum pipe (e.g. aluminium) unless a substrate was laid in the pipe.

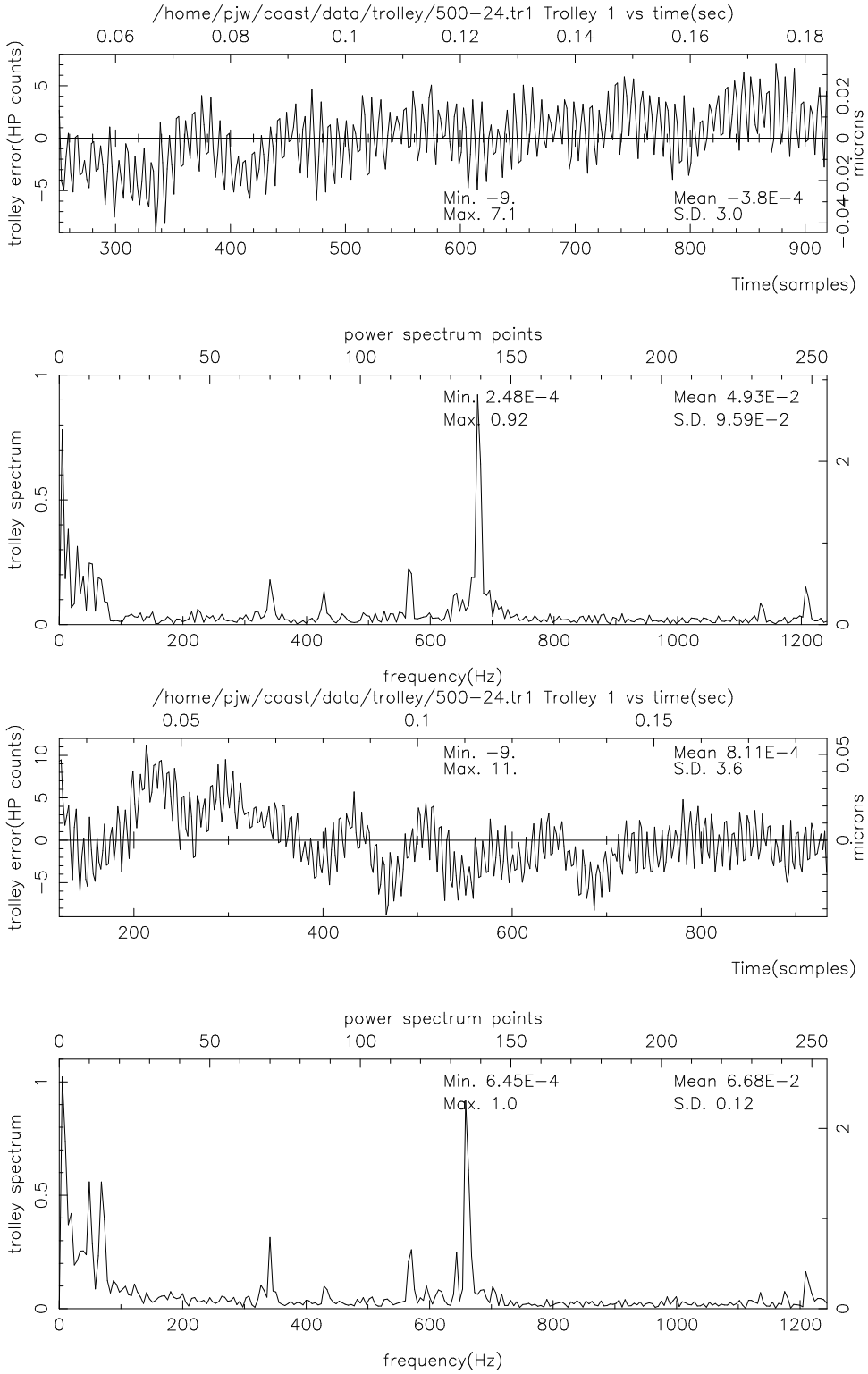

Figure 6.3: Metrology data time series and power spectra from the COAST trolley powered normally (top) and inductively (bottom) while it was tracking at about 1.4mm/s. The use of inductive power does not appear to affect the trolley behaviour.

6.7 Comments

These comments relate to some features of the scheme which may not be obvious without explanation.

6.7.1 Pick-up transformer

For a given frequency and ferrite a certain cross-sectional area of core is needed to run at a particular voltage. This would make high frequencies seem desirable, but the induction wire reactance is also proportional to frequency, so really high frequencies are not suitable. The trials we have carried out have been at about 25 KHz which seems to be a sensible compromise.

In order not to have to lift a long length of wire – it has to be tight, see below – it must not be lifted very far, and to fit the transformer below the trolley means that the transformer core should be thin in section, consequently it has to be long to achieve the necessary area.

The transformer has only a single turn primary – the induction wire – so it is easier to have only a single turn secondary and correct the voltage in another transformer than to have a multiple turn secondary. This means that the core support tube can double as the secondary, leaving all the centre clear for the easy passage of the induction wire.

6.7.2 Wire tension

To avoid any possibility of the induction wire forming loops or kinks, due either to thermal effects or the passage of the trolley it needs to be under a steady maintained tension. This needs to be enough to slide the *whole length* of the wire along the bottom of the pipe, but not too high or the catenaries (unsupported lengths of wire) either side of the transformer will be longer than need be, and more friction will arise because of the unnecessary weight being carried.

The friction coefficient of the wire and the pipe can be made sensibly small by careful choice of the wire covering, so the tension should not need to be more than $\frac{1}{3}$ of the weight of the wire.

The tension should be maintained by a spring or similar device, so that it is not affected by thermal expansion etc.

6.7.3 Slewing power

Depending on the rolling resistance of the trolley it may be desirable to make more power available for slewing than for tracking. This could be done without increasing the continuous rating of the supply system by using an on board energy store.

At present the best solution would appear to be ‘super-capacitors’ rather than batteries: batteries are good for long term storage and moderate power outputs, but may release gasses, have a limited life, and may lose capacity through “memory effect”. Super-capacitors are good for short bursts of high power, are probably less likely to leak gas, and are reputed to have an indefinite life. However, super-capacitors are likely to be heavier and more expensive than batteries in this application. The relative merits of the two approaches are still being investigated, and will be considered in more detail when the slewing power requirement has been refined.

Chapter 7

[002-06] Trolley Steering

Principal risks:

That it may be difficult to design a suitable steering mechanism for the delay line trolley to counteract the tendency of the trolley to rotate about its optical axis — hereafter we shall refer to this as "clocking".

That control of the delay line trolley steering may interact unfavorably with control of the longitudinal motion of the trolley.

7.1 Aim

- To determine what factors produce or affect the rotation of the trolley about the pipe axis and the sensitivity of the trolley to such influences at various speeds.
- To determine if steering would be necessary at all.
- To investigate the properties of candidate steering options.

7.2 Definitions and useful constants

Clocking: the angular motion of the trolley about the pipe axis

Average clocking rate: the observed clocking angle divided by the distance over which it occurs.

CofG: Centre of Gravity

The inner diameter of the pipe is 381mm, so 1mm at circumference is 5.25 milliradians i.e. 0.3°/mm.

7.3 Method

The test trolley was placed in the pipe and pulled through the pipe using a string. The string was attached to a point close to level with the centre of gravity of the trolley so as to minimise any applied couple which could affect the clocking of the trolley. Because it was difficult to get the trolley to clock significantly, tests were repeated by pulling the trolley back and forward through the pipe multiple times, while carefully checking that reversing the direction of the trolley's motion did not cause the clocking to "unwind".

Tests were repeated with different weights attached to the trolley to move the centre of gravity (CofG) either upwards or sideways, in order to simulate a trolley whose CofG was closer to the axis of the pipe and/or a trolley which was unbalanced laterally with respect to the centre of the wheels.

7.4 Results

7.4.1 General observations

The test trolley was stable to clocking in the pipe at all velocities including some in excess of 1m/s. This is due in part to the centre of gravity of the cart being lower than the pipe axis. Any external force which causes the trolley to begin to clock is eventually countered by an opposing torque about the pipe axis and the trolley will continue at a constant angle.

7.4.2 Repeatability in clocking

This test addresses how repeatable the trolley clocking angle is when run repeatedly backwards and forwards the full length of the pipe at different velocities. Eighteen tests were carried out, six at each estimated velocity of 50mm/s, 200mm/s and up to 1m/s. The trolley was pulled through the pipe for the full length from each end and the angular deviation from a fiducial mark on the pipe checked. In all cases the angular deviation was less than 1mm, that is, within 0.3°.

7.4.3 Response to a clocking offset

The trolley was not unbalanced about its long axis but was given an initial rotation from the horizontal position and then pulled through the pipe to see how quickly it returned to the horizontal position.

It was found that an offset in rotation of 15mm (4.5deg) from the stable position was restored to within 1mm within a single traverse of 5.5m, and remained stable thereafter. This implies an average clocking rate of 0.836°/m. The trolley weight was approximately 20kg and the CofG was estimated to be 83mm below the axis of the pipe and so this can be seen as the response of the trolley to a restoring couple of 1.35Nm.

7.4.4 Response to a weight imbalance

A mass of 0.96kg was attached to the trolley at 125mm radius from its long axis and ∼60mm above trolley CoG. The cart was pulled through the pipe to see how quickly and ultimately how far it deviated. The rotational offset produced was 13 mm (3.9°) in 3m of travel, i.e. an average clocking rate of 1.3°/m, and thereafter the offset remained stable.

7.4.5 Response to a driving force imbalance

The trolley was balanced about its long axis but was pulled from one side close to the wheel to simulate being driven by one wheel. The offset achieved was small but repeatable and reversible (by switching string to other wheel location). The measured clocking was 1mm (0.3°) in 5.5m of travel. The offset is only measured at the end of travel and so was assumed to occur at a constant rate over the travel, leading to an inferred clocking rate of 0.055°/m.

7.4.6 Response to a misaligned wheel

One wheel was misaligned by introducing a 0.3mm shim between the two washers that are used to help space the wheel from the side flange to which it is attached. This cants the wheel by approximately 0.3mm/10mm or 1.8°. The wheel was at the front LHS, facing the cart, was canted such that it produced 'toe-out' orientation.

When the trolley was pulled through the pipe, this induced 13 mm (3.9deg) clocking over a 3m run, after which the clocking stabilised. The trolley was then pulled back through the pipe, causing the trolley to clock the opposite way, passing through the nominal zero of clocking angle and stabilising at -3.9deg after 3m of travel. It seems likely that this limiting angle is largely independent of the steering angle (misalignment) of the wheel because the same limit was reached when the wheel was aligned but the trolley is out of balance. The average clocking rate in this case was 2.6°/m, i.e. significantly faster than most other clocking deviations measured, indicating that steering one wheel by a maximum of 1.8° would be effective at counteracting any other forces causing the trolley to clock.

In a second test, a significantly greater wheel misalignment was introduced. During trolley vibration testing with the motor driven cart a wheel misalignment of 4.6° (far greater than any angle that would be required for steering) was introduced using the same method as before but with a thicker shim. No evidence was found of any increase in vibration levels or other adverse effects. The test results are reported in section 8.10.

7.4.7 Tests with heavier trolley and higher CofG

Additional mass was added to the trolley to raise the centre of gravity closer to the pipe axis, about 15mm–17mm below the axis as opposed to 83mm in the previous tests. The 0.96kg unbalanced load at 125mm radius from the trolley axis was also added. With the heavier trolley, all disturbances took much longer distances to reach their full effect, and so the trolley was run through the pipe multiple times to give enough distance over which to see all of the behaviour. It was found that the trolley had an initial clocking rate of 1.64°/m for the first 16.5m of travel, after which the clocking rate decreased, eventually becoming negligible after 50m of travel, when the total clocking angle was 36°.

7.5 Discussion

In all the tests, the clocking rate of the trolley was typically at rates of less than 2°/m. The most stringent requirement on trolley clocking is that the wheels run over the pipe join within about $\pm$1cm of the nominal wheel track, i.e. with an accuracy of about $\pm 3°$. With the trolley moving at a maximum speed 1 m/s, this means that, very roughly speaking, the trolley may need steering corrections which are updated once every 1.5 seconds.

When the CofG of the trolley was low, the trolley was essentially self-correcting. It may be desirable to raise the trolley CofG in order to provide an aligned reaction mass for the catseye voice-coil, so that applying forces to the voice-coil does not induce a "rocking" motion of the trolley. In this case a servo correction scheme is likely to be needed. The closer to the pipe axis the CofG of the trolley was, the more the equilibrium position of the trolley was influenced by external forces but the *rate* of clocking was not significantly changed, implying similar servo update rates would be adequate for most trolley configurations.

It was shown that an off-axis weight or steering one wheel can be used to provide the correction force, without compromising the OPD performance. Steering offsets of order one or two degrees are sufficient

to overcome any perturbations encountered, so linear behaviour can be assumed in any form of control or compensation.

Providing the CofG is below the centre of the pipe, a faulty trolley can be pulled back through the pipe without fear of it rotating more than a certain amount. This is a highly desirable safety feature for the trolley and for the inductive power cable that runs underneath it.

Chapter 8

[002-07] OPD Disturbance Tests

Principal risks:

That the OPD disturbance spectrum expected for the proposed delay line concept will be considerably larger than that expected (and managed) by a trolley running on precision rails, for example the COAST delay lines.

8.1 Aim

There are four specific aims:

1. To measure the actual disturbance rejection of the COAST trolleys in the direction of the OPD and compare this with the predicted rejection based on a MATLAB and Simulink model so as to validate our modelling capability.
2. To compare the vibrational noise spectrum on the COAST trolley which uses precision rails and hard wheels and compare that with the spectrum obtained from the MROI Embryo trolley running on compliant wheels inside a standard pipe.
3. To estimate the expected OPD noise spectrum for the MROI trolleys, by propagating the measured disturbance spectrum through a dynamical model of the MROI delay lines.
4. To measure the effect of a gap between pipes on the OPD noise spectrum and determine the maximum allowed gap that still permits sucessful metrology measurements.

8.2 Overall Method

The COAST-related parts of Aims 1 and 2 were realised by measurement of acceleration disturbances of a COAST trolley whilst tracking at different rates, passing the information through a suitable model of the trolley to obtain estimates of OPD displacement and comparing the results to contemporary data from the metrology system (which directly measures the OPD displacement, i.e. the position of the voice-coil-driven trolley optics). Other ancillary tests were undertaken to confirm trolley and delay line table characteristics).

Similar acceleration measurements were made on the embryo MROI trolley travelling in the test rig (described in Chapter 3). These were compared with the COAST measurements to realise Aim 2, and passed through a similar model but based on the proposed MROI trolley design in order to satisfy Aim 3.

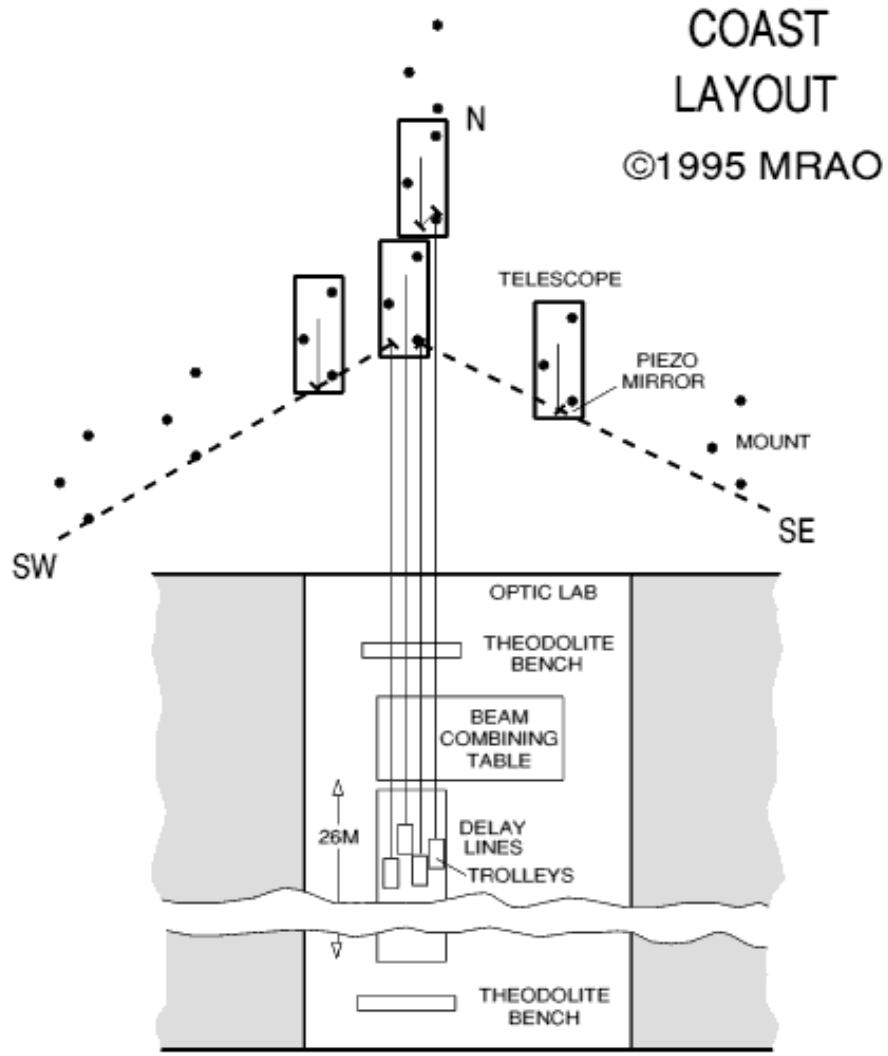

Figure 8.1: COAST array layout. The delay line trolleys are numbered 1 to 4 from left to right.

Aim 4 was realised by making acceleration measurements as the embryo trolley travelled over a gap introduced between two pipe sections.

8.3 Modelling of COAST trolley

8.3.1 COAST System

The COAST system is shown in Figure 8.1. The delay line trolleys are shown and are numbered 1 to 4 from left to right. The tests were conducted on trolley 3, using trolley 2 as a reference for reasons explained in Section 8.4.3. The delay line table is composed of optical benches mounted end to end on flexures to accommodate thermal expansion. The laser metrology system is mounted at the end of the delay line table and so is common to all four trolleys.

A schematic of the COAST trolley system is shown in Figure 8.2. The roof mirror assembly (henceforth

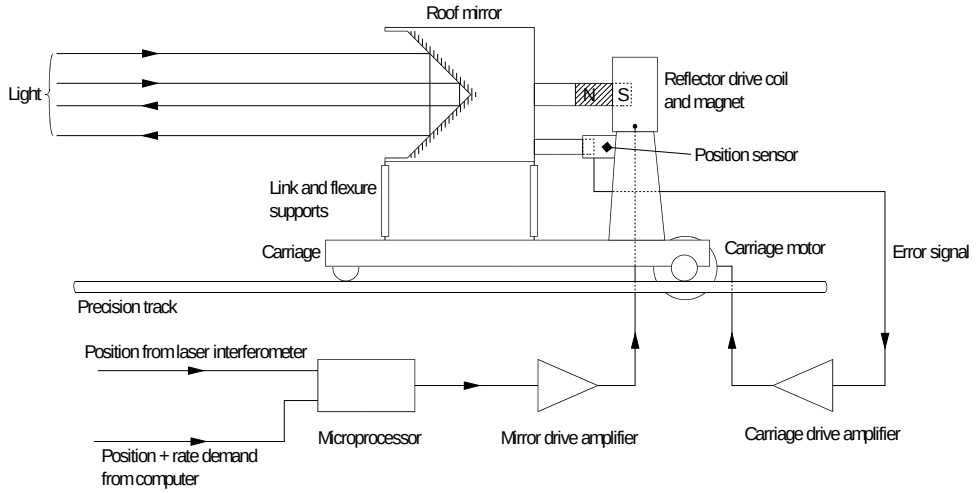

Figure 8.2: Schematic of COAST trolley.

referred to as the reflector) is mounted on flexures attached to the carriage and is driven axially by a voice coil. The carriage is driven by a DC motor connected directly to the drive wheel running on one of the tracks and a velocity loop is formed using an encoder on the motor shaft. The principal control loop is through the metrology signal driving the voice coil to maintain the commanded position. A position sensor mounted on the carriage provides differential position between the reflector and the carriage. This position signal is used for two purposes: firstly to command the motor velocity so as to "off-load" the deflection of the optics thus maintaining the carriage under the reflector with minimal flexure deviation; secondly, the differential position is fed back to the voice coil drive stage to achieve an active reduction of flexure stiffness. This has the effect of increasing the natural isolation of the flexures in the OPD direction but has little or no effect on damping. To achieve closed loop stability and provide sufficient phase margin a phase lead filter is incorporated into the forward path of the loop.

8.3.2 The COAST model

The COAST system model is based on the general model developed for the MROI system. It addresses only axial dynamics, i.e. in the OPD direction, and includes linear features that are known or deducible from the design or through simple tests. The only non-linearity included in the model is the resolution of the metrology system and a delay representing latency in deriving the metrology signal.

The COAST model as implemented in Simulink is shown in Figure 8.3. The servo loop which provides the active rejection comprises:

1. The metrology link (includes the loop delay, quantisation and D/A conversion)
2. The phase lead filter (provides gain and frequency/phase compensation)
3. The voice coil and amplifier (converts voltage to current and hence to force)
4. The carriage and reflector dynamics (models the reflector on a motor driven carriage)

The position of the reflector is measured by the metrology system and is differenced with the commanded position to produce the error signal which corrects the reflector position. The loop gain parameters in this servo loop were provided from the design but also verified by test, as was the resonant frequency and damping of the reflector assembly.

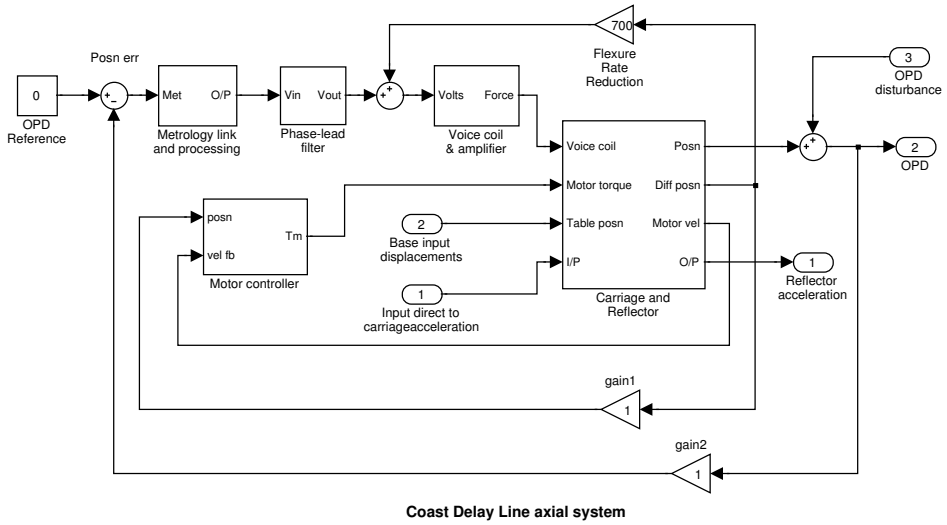

Figure 8.3: Top-level simulink model of COAST trolley.

The model provides for various disturbance inputs but the principal measurement to be made for these rejection tests is acceleration of the carriage and therefore this input is specifically provided. The combined position of carriage and reflector is output for the OPD together with output acceleration of the reflector. The differential position between the carriage and the reflector is passed to the motor controller which commands the velocity of the carriage in order to minimise the difference. This “off-loading” of the reflector motion to the carriage is done to keep the carriage positioned under the reflector with near zero deflection of the flexures.

A summary of the important parameters and characteristics of this model is given in Table 8.1. These are typical values for such a system but the most important parameter is the loop gain which determines the disturbance rejection and the bandwidth characteristics. The forward path DC gain is increased as much as is feasible, without compromising stability, so as to provide as high a loop gain as possible.

8.3.3 Model behaviour

The disturbance rejection characteristics predicted by the COAST model, together with some informative loop transfer functions are shown in Figure 8.4. The reflector mechanical transfer function, which is determined by the reflector mass and the spring constant of the flexures, is shown peaking at the “reflector natural frequency” of 2 Hz. The effect of the feedback loop employed to reduce the apparent stiffness of the flexure is shown in the transfer function marked “reflector reduced frequency”. This transfer function is effectively raised by the low frequency loop gain to become the “Open loop TF” marked. The intersection of the Open loop transfer function with the zero dB axis is called the gain cross-over frequency and determines the zone where the closed loop transfer function starts to decrease, defining the bandwidth of the servo.

Table 8.1: Parameters of Simulink trolley models. Values for both the COAST model (described in Section 8.3.2) and the MROI model from which it was adapted (Section 8.6) are given.

Trolley/Servo Parameter	**COAST Value**	**MROI Value**	**Units**
Forward Path dc Gain	92	117	dB
Reflector assembly mass	1	30	kg
Carriage Mass	19	50	kg
Flexure stiffness	158	1185	N/m
Damping	1	1	%
Reflector natural frequency	2.2	1	Hz
Reflector reduced natural frequency	0.7	0.6	Hz
Gain cross over frequency	90	97	Hz
3dB Bandwidth	163	177	Hz
Low frequency loop gain (G_L)	67	68	dB

There are two disturbance transfer functions or "sensitivity functions", also plotted in Figure 8.4, that are useful to assess:

- The **OPD sensitivity function** determines the rejection of disturbances to path length between the reflector and the laser metrology mount, irrespective of the source of those changes.
- The **reflector acceleration sensitivity function** is a measure of the rejection of the reflector assembly to disturbances of the carriage which supports it. This is meaningful because it can be used to predict the OPD performance due to carriage motion from acceleration measurements of the carriage itself.

The value of the OPD sensitivity function is approximately the inverse of the loop gain, i.e. $1/G_L$, up to the reflector resonance and then increases to around 0 dB at the gain crossover frequency.

Although influenced by the carriage servo, the rejection described by the reflector acceleration sensitivity function is composed of the natural isolation of the flexures and the closed loop metrology servo. It is essentially flat, at the level of OPD rejection, but continues up to the closed loop bandwidth of the system, peaks, and then becomes asymptotic to the "mass-spring line" defined by the reflector parameters. The rejection is thus approximately $1/G_L$ up to the system bandwidth and then falls off to 20 dB per decade.

The rejection performance of the system to given OPD direction acceleration disturbances at the trolley is calculated by multiplying the power spectral density (PSD) of the carriage acceleration by the square of the acceleration sensitivity function. This function is obtained in state-space form from the model by using the *dlinmod* function in MATLAB. The resulting PSD is then processed for comparison with laser metrology results.

8.4 Acceleration and Metrology Measurements

8.4.1 Data recording

The equipment used for the acceleration measurements included three ICS piezoresistive silicon accelerometers and two Bruel & Kjaer miniature modal analysis internally amplified piezo accelerometers. A two-channel Siglab unit connected to a portable PC running MATLAB and configured for spectral analysis mode provided data acquisition facilities and real-time spectral analysis.

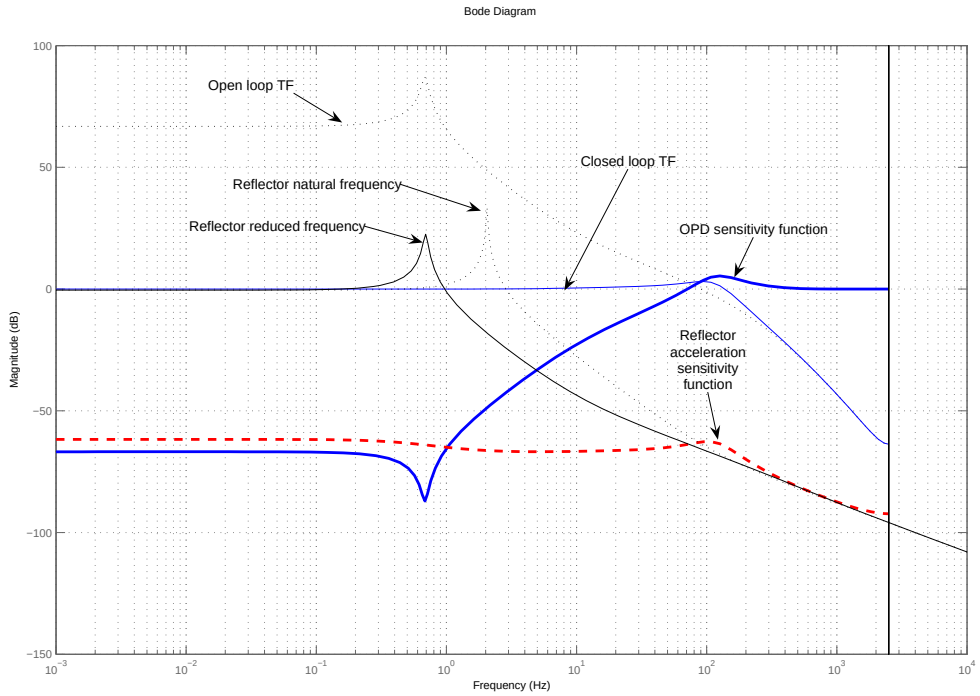

Figure 8.4: COAST trolley transfer functions predicted by Simulink model. See text for details.

The accelerometers were usually sampled at 2560 Hz for 3.2 seconds, giving a frequency resolution of 0.3125 Hz. Delay line metrology data were recorded, at a sample rate of 5000 Hz for 2 seconds, using a facility built into the control software for the COAST delay lines.

8.4.2 Delay line table

To identify any signals in the trolley tests which are due to delay line table axial modes or local vibration sources accelerometers were mounted on the table in pairs, in turn, in two of the three orthogonal axes and near the area of the trolleys under test. A set of background vibration tests and impulse tests provided the information to be used in assessment of OPD tests.

8.4.3 Arrangement for main OPD test

The laser metrology system is mounted at the end of the delay line table which also supports the four trolleys and is mounted on flexures to accommodate thermal expansion. At low frequencies the axial vibration of the system will be common on all components, including the metrology system which will cause the cats-eye servo to follow. Consequently vibration will be evident on accelerometer signals which will not appear in the metrology results.

To remove a substantial amount of this common mode acceleration either the low frequency data (everything below 10 Hz, including the first axial mode of the table) could be simply ignored or another reference could be used which effectively allows subtraction of the metrology laser motion. The latter method was chosen and the reference used is the acceleration of the cats-eye of another trolley, commanded to be stationary, which is also servoed using the metrology laser. This method also has limitations:

1. Higher frequencies may or may not be common to both delay lines.
2. OPD fluctuations due to the atmosphere will not appear on the test carriage accelerometer data but may appear on the reference trolley reflector accelerometer as the metrology system attempts to servo them out.
3. OPD fluctuations due to the atmosphere which are above the servo bandwidth will appear on the metrology data but not accelerometer data.

As outlined in Section 8.2, the objective of the test is to compare the performance indicated by the metrology data with the performance obtained from the output of the trolley model, taking into account the limitations above. The input to the trolley model is the differential acceleration of the test trolley with respect to the reference trolley.

Of the four available trolleys, Trolley 2 (T2) was used as the reference and Trolley 3 (T3) was the trolley under test. For the OPD tests a small piezo accelerometer was fitted to the reflector optics of T2 with its measurement axis aligned in the OPD direction. A second accelerometer was fitted to the rigid base of the optics mount, attached to the carriage of T3, with its axis also aligned in the OPD direction. Velocity tests were conducted by carrying out a virtual observation, keeping Trolley 2 on station while Trolley 3 tracked. Two tracking velocities were tested: 0.1 mm/second and 1.4 mm/second which was the maximum available.

8.4.4 Data processing

Time series accelerometer data were usually saved, but auto-spectrum data were exported for some of the tests, where spectra were averaged for three or five 3.2 second frames. The time series data were processed to produce acceleration power spectral densities. There was found to be some scatter in consecutive measurements, suggesting small changes in conditions on timescales $\sim$ 10 seconds. Wherever possible the results taken in auto-spectrum mode were used, as being more representative of the average conditions.

For each test the reference trolley PSD was subtracted from the test trolley PSD. The difference PSD was then multiplied by the magnitude squared of the acceleration sensitivity function obtained from the model and the resulting output PSD processed to produce the displacement spectrum of the reflector.

Contemporary laser metrology data was processed to produce the displacement spectrum of the metrology error.

The data extracted using these processes were used to compare the expected rejection performance derived from the model with the actual performance provided from the laser metrology system (Aim 1) and are presented in Section 8.5.2.

8.5 COAST Results

8.5.1 Delay line table

Background tests show a mostly uniform acceleration power spectrum rolling off at 20 dB per decade initially, to 10 Hz and then at 10 dB/decade. There is only one feature, at 41 Hz, corresponding to a lateral mode of the table.

Impulse tests show that the first axial mode of the table is 9.1 Hz with damping of 1%. Nine other modes (including the 41 Hz lateral mode) were identified, with frequencies between 17 and 120 Hz.

Table 8.2: Comparison of metrology data and COAST model output. An asterisk indicates that the acceleration measurement used as input to the model is the average of three PSDs in Siglabs averaging mode (see text in Section 8.4.4). For the reasons explained in the text, the model output should be compared to the metrology results in the < 40 Hz band.

Test	Velocity (mm/s)	Output model displacement (nm RMS)	Metrology results	
			T3 < 40 Hz (nm RMS)	T3 Full BW (nm RMS)
LBtest84*	0.1	0.7	0.5	5.6
LBtest85*	1.4	4.5	3.6	8
LBtest92	Standstill	0.6	0.2	6

Most of these modes are visible in the accelerometer data and the metrology data but their contribution in the OPD direction is generally less than 1nm RMS. Hence table modes do not significantly pollute the measurements of vibrations of the COAST trolley travelling on its tracks, nor affect the comparison of measured and model-predicted OPD rejection.

8.5.2 COAST trolley results

Tests were undertaken at standstill, 0.1 mm/s and 1.4 mm/s. The results are presented in Table 8.2, which shows the output of the model (the computed RMS displacement of the reflector), given the measured (differential) input accelerations. Also shown are the contemporaneous metrology results for each trolley but separated into two bands; the displacement for frequencies up to 40 Hz and the full bandwidth displacement (up to 2.5 kHz).

Subtraction of the reference trolley reflector acceleration PSD removes common mode OPD error from the test trolley acceleration PSD leaving an estimate of the error due to the motion of the trolley. This is why the comparison is made up to 40 Hz, because after that the common mode OPD error dominates any accelerations of the test trolley.

There is good agreement between the < 40 Hz model output and the metrology data, given the problems inherent in subtracting the motion of the reference trolley.

8.5.3 Conclusions

Because the metrology error is due to a number of sources and the need to establish some form of inertial reference it is not possible to measure all the contributory factors directly. However the method described addresses the substance of the issue which is the motion of the COAST cart and the inherent rejection in the OPD direction due to the flexures and the closed loop laser metrology servo.

The COAST model developed adequately predicts the performance of the trolley in this respect, to within 1 nm for averaged power spectra. This validates our adoption of a similar model for the MROI trolley and its use in predicting performance from accelerometer measurements of the embryo trolley running on compliant wheels inside the delay line pipe.

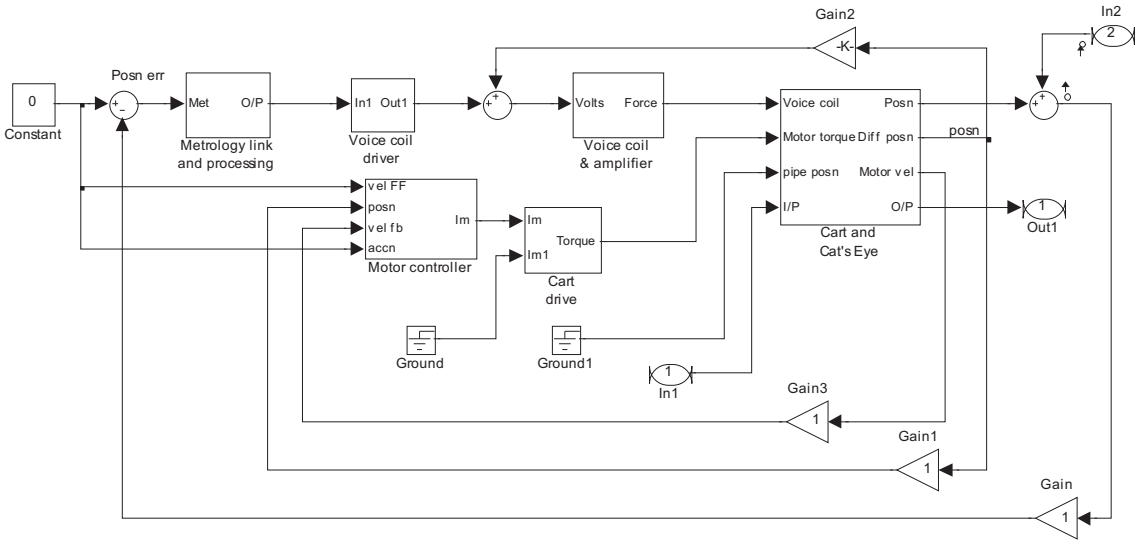

Figure 8.5: MROI trolley axial simulation.

8.6 Modelling of proposed MROI trolley

8.6.1 The MROI Model

The MROI model (Figure 8.5) is similar to the COAST model presented earlier (the COAST model was actually developed from this model). The features are essentially the same but the parameters for the wheels, drive system, mass of carriage and cat's eye are significantly different — see Table 8.1. Again, this is a linear model except for quantisation and a nominal 50 ms metrology servo latency. A two-stage lead network was required to obtain sufficient gain and phase margin at the bandwidth of 177 Hz (similar to that of COAST).

The loop gain was chosen to be similar to that of the COAST trolley system. This resulted in a gain margin of 14 dB and a phase margin of 57°.

The mechanical resonance of the cats-eye is expected to be around 1 Hz and is reduced to 0.6 Hz by feedback as described for COAST.

8.6.2 Model behaviour

Transfer functions predicted by this model are shown in Figure 8.6. These are the equivalents of those derived from the COAST model plotted in Figure 8.4.

However, there is a significant difference in the cats-eye acceleration rejection transfer function because the carriage-cats-eye differential position loop is closed in this model. This reflects a difference in the experimental setups (the COAST measurements were made on a carriage being actively servoed), rather than a difference between the servo system implemented at COAST and that proposed for MROI. In the setup for the MROI tests, unlike the COAST tests, there is no control of the carriage velocity because there is no cats-eye to feedback position information. Hence the measured acceleration disturbance spectra are not exactly equivalent, so the models must take this into account to generate comparable outputs.

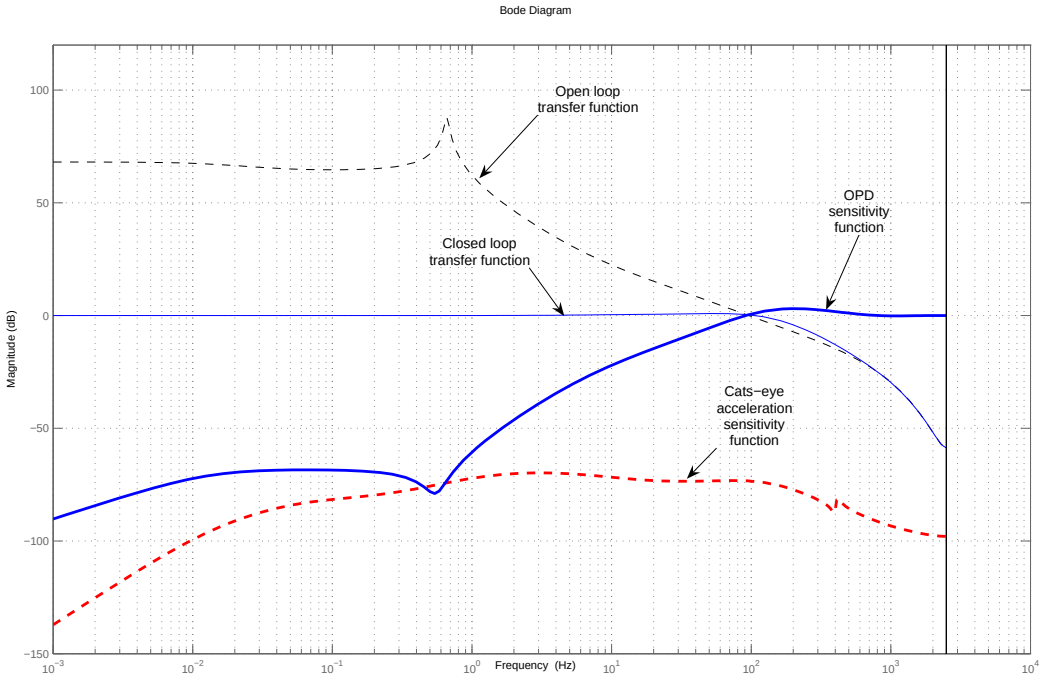

Figure 8.6: Prospective MROI trolley transfer functions.

The trolley acceleration sensitivity function is between -70 dB and -80 dB over the range 0.1 Hz to 300 Hz, some 5dB better than COAST because the velocity control loop is effective. The OPD sensitivity function is much the same as COAST, providing 50 dB of rejection at 2 Hz.

8.7 Tests of Embryo Trolley in Test Rig

8.7.1 Test arrangement

The embryo trolley used for tests in the pipe test rig is a piece of aluminium angle section approximately 1.7 metres long with sides of 150 mm and a thickness of 12.5 mm. A steel platform approximately 330 mm wide and 500 mm long is mounted on top of the angle, half way down its length, and this holds motor drive electronics and counter weights as required. Provision is made to move the centre of mass up and down by adding weight to two rods which are secured to the trolley near the front and rear. The trolley runs on 75 mm diameter wheels mounted to the flanges of the angle such that the longitudinal wheel base is 1.5 m. To drive the trolley a brushless motor is mounted so that its shaft is sprung-loaded onto one of the wheels providing a friction drive with a gear ratio of approximately 12:1. Most of these features can be seen in the photograph (Figure 8.7).

The data recording equipment and procedure were the same as described in Section 8.4.1 for the COAST tests. The accelerometers were generally mounted at one end of the trolley, one axially at the apex of the angle and one either vertically or at 45° to vertical on one of the flanges.

8.7.2 Vibration modes of embryo trolley

A basic finite element analysis (FEA) of the embryo trolley was carried out to predict the significant modes, especially those due to the compliant wheels. The results for the first few modes are shown in

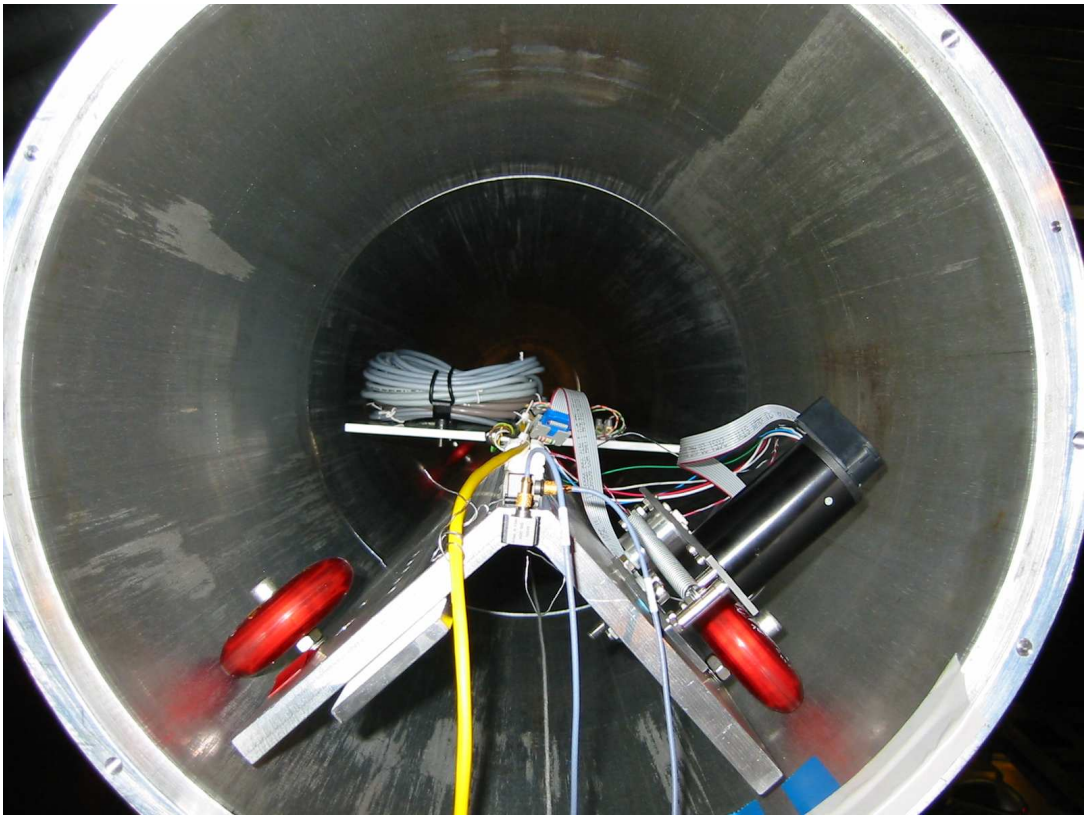

Figure 8.7: Photograph of embryo trolley in pipe test rig.

Mode No.	Freq. (Hz)	Description of mode	Actual Freq. (Hz)
1	20	Lateral rocking about longitudinal (X) axis	17
2	23	Vertical displacement (Y)	21
3	33	Rocking (about Z) combined with axial displacement (X)	31
5	33	Rotation about Y	-
6	37	Rocking about Z	31
7	107	1st twisting mode of chassis	110
8	156	2nd twisting mode of chassis	130
9	204	1st vertical bending mode (longitudinal)	168
14	440	2nd vertical bending (longitudinal)	415

Table 8.3: Embryo trolley predicted and actual vibration modes.

Table 8.3 below. Coordinates are: X is longitudinal (axial); Y is vertical; Z is orthogonal to X and Y, i.e. sideways, and rotations are generally about the centre of gravity (CoG) of the trolley.

To validate the FEA results, a set of simple impulse tests were carried out in the axial and vertical directions with the accelerometers monitoring the response in those directions. An example of the trolley response to a vertical impulse is shown in Figure 8.8.

The impulse tests were performed with the trolley loaded with some equipment, not accounted for in the FEA, and also without the motor fitted. The measured frequencies of the identified modes are shown Table 8.3, for comparison with the FEA results.

The FEA predicts the important modes sufficiently well and so can be used to provide the basis for a

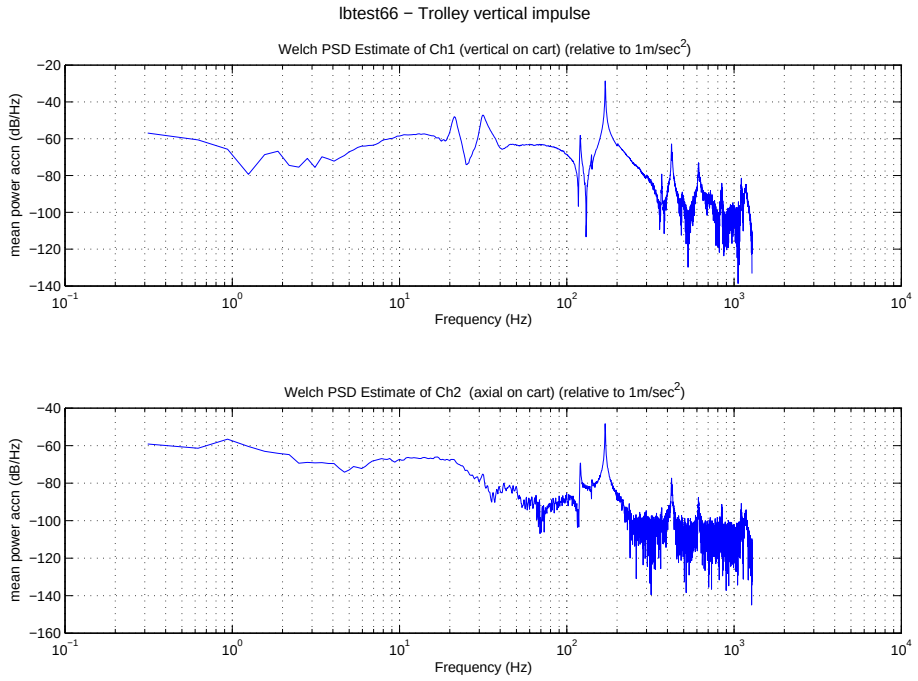

Figure 8.8: Response of trolley to a vertical impulse at one end.

more comprehensive dynamic model of the embryo trolley.

8.7.3 Isolation tests

There is considerable benefit gained from the soft wheel approach in the reduction of rolling disturbances, i.e. vibration introduced through the wheels from roughness of the track, as the velocity tests will show. There is also some benefit from isolation of external disturbances above a few tens of Hz in exchange for resonances due to the low-frequency rigid body modes. This is demonstrated in the vertical direction by measuring the vibration of the pipe under the trolley and comparing it to the vibration of the trolley.

Two measurements of the isolation were conducted, one showing the suppression of background levels and one showing the response to a vertical impulse to the pipe. The latter result is shown in Figure 8.9. In the bottom trace the pipe resonances are clear, clustered around 50 Hz, 125 Hz, 220 Hz and 630 Hz. The resonant response of the trolley at 21 Hz and 31 Hz is clear but with suppression of the pipe frequencies by at least 15 dB at 50Hz, 30 dB at 125 Hz and 50 dB at 220Hz. The general level of rejection from 70 Hz upwards is 20dB. This effective shift of power to the lower frequencies together with the higher damping available may be beneficial in reducing excitation of higher modes of the trolley which may couple into the OPD direction. Damping of the pipe frequencies around 50 Hz is about 1% and at 220Hz is 0.3% whereas damping of the trolley vibrations at 21 Hz and 31 Hz is estimated to be 4% (using the half-power bandwidths).

The mass of the embryo trolley used for all tests is between one quarter and one third of the expected mass of the MROI trolley so one could expect rigid body modes of the prospective MROI trolley to be lower in frequency and the higher mass to reject more of the high frequency disturbance. This is evident in the velocity tests which were undertaken with higher loads on the trolley.

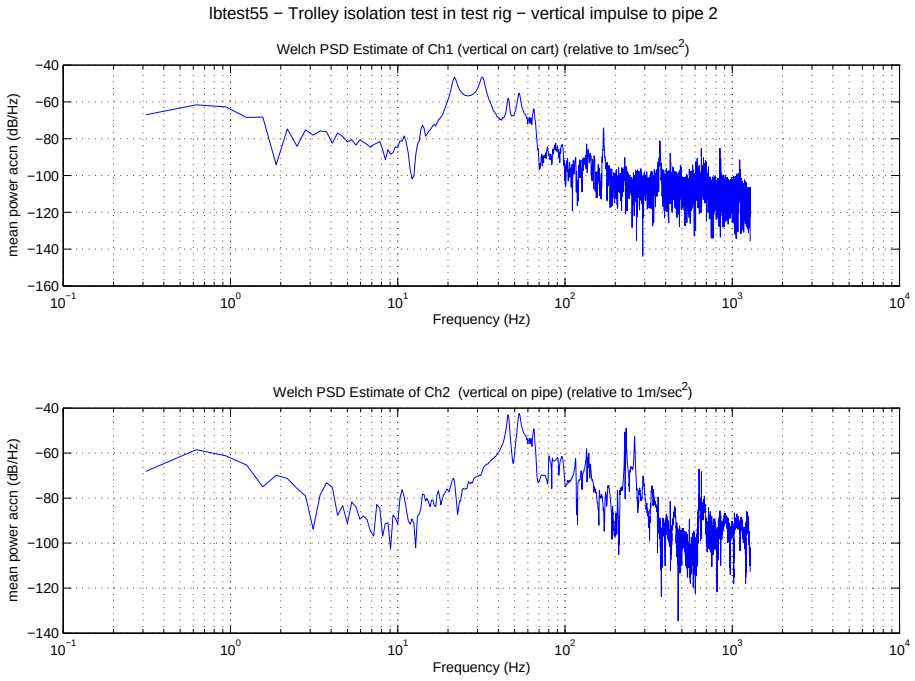

Figure 8.9: Vertical response of trolley to a vertical impulse to the pipe.

8.7.4 Measurement of disturbance spectra

The principal measurement made with the embryo trolley and test rig was to obtain power spectra of the axial and vertical acceleration of the trolley at different velocities. These will be compared directly with the equivalent measurements of the COAST trolley (Aim 2) and also put through a model of the proposed MROI trolley to assess the residual disturbance spectrum (Aim 3).

Some initial velocity tests were carried out by simply pulling the trolley along using a length of string. This was particularly useful for higher velocity tests where care had to be taken that the trolley would not overshoot the pipe. Tests with the motor drive varied from 1 mm per second to 550 mm per second though most were kept below 100 mm/s for practical reasons (cable feeding in and out and reducing the influence of cable dragging).

The tests were carried out with two load configurations; with a load of ~ 25 kg, and with a further 8 kg mounted above to give a higher centre of mass (between 15 mm and 20 mm below the nominal axis) for the steering tests described in Chapter 7. In the second configuration, the additional mass created additional resonances around 40 Hz and 65 Hz but this did not impinge on the trolley results which, as with the COAST tests are necessarily focussed on the low frequency range from 0.1 Hz to 40 Hz.

The analysis of the acceleration data is identical to that for the COAST tests except for the model used. The results are presented in Section 8.8.

8.7.5 Effect of slewing trolley on pipe vibration

The apparatus was also used to investigate the risk that the moving trolley might induce large vibrations in the flexure-supported pipe when slewing. These results are presented in Section 3.3.4 in the chapter on pipe supports.

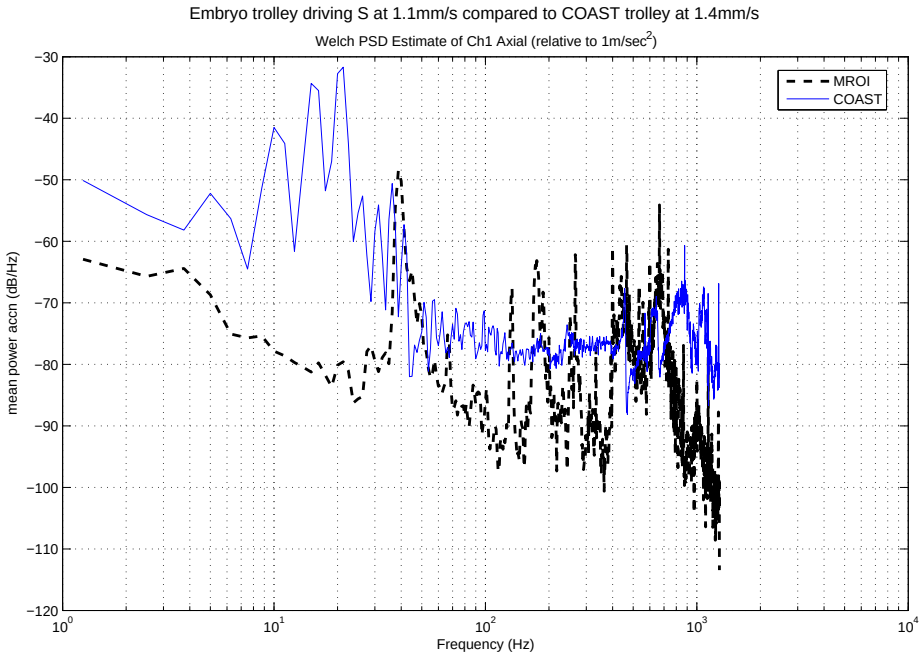

Figure 8.10: Comparison of COAST and embryo trolley axial acceleration PSD.

8.8 MROI OPD Results

8.8.1 Comparison with COAST vibration measurements

A comparison of axial vibration of a COAST trolley and the embryo trolley is shown in Figure 8.10. The velocity of the COAST trolley is 1.4 mm/s and the acceleration power spectrum is dominated by motor commutation and encoder interpolation error between 10 Hz and 20 Hz. The velocity of the embryo trolley is 1.1 mm/s and the acceleration power spectrum is generally 20 dB lower but with motor disturbances at frequencies beyond 100 Hz. The peak at 40 Hz is due to the mounting of the additional mass.

This result demonstrates that the softer wheels running on a relatively rough surface have significant isolation due to the greater contact area of the wheel and the ability of the wheel to deform easily on a small scale. Hence the risk that the vibration of the MROI trolley will be larger than that experienced with precision rails proves to be unfounded.

8.8.2 Results from MROI model

The result of passing the acceleration measurements for the embryo trolley through the MROI model are presented in Table 8.4. Note that there is no subtraction of power spectra here to remove common mode vibration so the accelerometer results contain all the low frequency motion of the test rig, unlike the COAST tests.

There is little to choose between results from the light or heavier trolley suggesting that a substantial amount of acceleration power is at low frequency and corresponds to vibrations of the whole test rig. There is also very little correspondence between velocity and RMS OPD error although the largest error does occur at the largest velocity in the table.

Test	Light /Heavy	Velocity (mm/s)	Cats-eye Piston (nm RMS)
42	L	2.2	4.6
41	L	5.5	4.9
39	L	5.5	6.3
40	L	11	8.2
51	L	2.2	6.6
54	L	11	4
55	L	22	4.5
67	H	1.1	2.8
69	H	5.5	5.0
70	H	11	3.6
73	H	22	9.1
74	H	22	5.6
80	H	55	15

Table 8.4: Predicted RMS OPD error as output from MROI model.

Several tests were conducted at 55 mm/s and 110 mm/s and these were clearly worse, between 15 nm and 60 nm RMS for 50 mm/s but it is clear that the worse results are due to the resonance caused by the compliance in the friction drive system. The results do show that, even with a crude embryo trolley, the axial disturbances induced by the interior surface of the pipe are rejected sufficiently by the combination of soft wheels and a conventional cats-eye servo (with a modest bandwidth of approximately 180 Hz) for the OPD stability requirement to be met comfortably.

8.9 Effect of a gap between pipes

The effect of driving a trolley over a gap between pipe sections was investigated (Aim 4), to assess the impact on OPD performance at tracking speeds, and to investigate the likelihood of losing the metrology signal at slewing velocity.

8.9.1 Effect at tracking velocities

The pipe ends have a small chamfer on them of about 0.25 mm so there is always some effective gap of order 0.5 mm. In the tests that were conducted this gap was virtually unnoticeable, it could not be detected directly in either vertical or axial acceleration data. The best measure was to monitor the power spectra for increased contribution at 4 Hz in the axial direction, which is the resonance of the friction drive system caused by the compliance of the driven wheel.

To obtain some indication of how much gap could be tolerated before tracking becomes unduly affected and also to determine the maximum size of gap that would still enable a laser metrology signal to maintain lock the joint between two pipes was deliberately widened. This was accomplished between the stub pipe and pipe 1 (see Figure 3.1) at the North end of the test rig by drawing the pipes apart, introducing a shim between the pipes at the bottom, and then clamping the pipes back together. The results of driving the embryo trolley over gaps of various sizes were as follows:

- With a 0.8 mm shim between the pipes the gap becomes at least 1.2 mm including the chamfer. A number of velocity tests were carried out between 2.2 mm/s and 50 mm/s to see if any disturbance

Test	Light/ Heavy	Velocity (mm/s)	Axial V max (m/s)	Vertical V max (m/s)
25	L	+10	1.5×10^{-3}	4×10^{-4}
26	L	-10	2×10^{-3}	3×10^{-4}
24	L	-22	3×10^{-3}	1×10^{-3}
27	L	+22	4.2×10^{-3}	1×10^{-3}
28	L	-55	7×10^{-3}	2.2×10^{-3}
29	L	+55	6.8×10^{-3}	2.5×10^{-3}
30	L	-100	5×10^{-3}	4×10^{-3}

Table 8.5: Maximum trolley disturbance velocities associated with a 3.7mm gap.

could be detected. There was none detectable in the vertical direction and only some evidence of a 4 Hz disturbance in the axial direction. However this level of disturbance could be seen anywhere down the pipe (due to a resonance in the servo loop) and so the join was not of particular influence.

- With a 1.6 mm shim it was still difficult to discern the join in the accelerometer data for speeds up to 50 mm/s but it was clearer in the increase in the 4 Hz contribution in the power spectrum over the level when the trolley does not pass over the join.
- With a 3.2 mm shim the join becomes obvious in the axial accelerometer data. At a speed of 1.1 mm/s the cart can be brought to a halt with the wheel sitting in the gap. At 2.2 mm/s it continues over the gap. Even with this "huge gap" the OPD error is not particularly large, being 11.8 nm RMS at 2.2 mm/s.

8.9.2 Effect at slewing velocity

The velocity in the axial and vertical direction is computed from the integration of the accelerometer data for tests where the trolley passed over the 3.7 mm gap. The maximum values associated with the gap event are presented in Table 8.5. The results suggest that the maximum disturbance velocity is proportional to cart velocity up to around 50 mm/s for both axial and vertical directions and then remains constant, at least for the axial direction. Further tests at higher velocity are required to confirm this. Given that these results are for a large gap and apply to the trolley (so would be smaller in the axial direction when referred to the cats-eye because of the inherent isolation) it is not thought that a practical gap of the order of 1 mm to 2 mm to allow for alignment of pipes and a small internal edge chamfer would cause the metrology laser system to lose lock.

A higher velocity test ($\sim$ 300 mm/s) was conducted by hand at the opposite end of the pipe where the effective gap is approximately 0.5 mm. This produced a vertical velocity maximum of 5×10^{-3} m/s and an axial velocity of only 2×10^{-3} m/s. This discrepancy occurs is due to a slight change of level in the pipe at one side.

8.10 Effect of misaligned wheel

One of the trolley wheels was deliberately misaligned and a set of tests conducted under these conditions to compare with normal conditions. A 0.8 mm shim was introduced between the trolley side and the wheel securing nut so that the shaft was tilted towards the rear of the trolley by an angle of 0.08 rad i.e. 4.6° (larger than any misalignment that would be used to "steer" the trolley — see Chapter 7). There was no obvious deleterious effect and tests were conducted at 2.2 mm/s, 11 mm/s and 50 mm/s.

Test	Light/ Heavy	Velocity (mm/s)	Cats-eye Piston (nm RMS)
33	L	2.2	5.9
34	L	2.2	3.7
35	L	2.2	2.6
31	L	11	2.3
32	L	11	5.1

Table 8.6: Effect of a misaligned wheel on OPD.

The results for tracking velocities are presented in Table 8.6 and should be compared to the results for correctly-aligned wheels in Table 8.4. There is no discernable effect on the trolley acceleration data and no change in the effective OPD performance.

These results show that alignment of compliant wheels is not critical. There are no measurable effects on the vibration of the trolley for a substantial misalignment and furthermore, the deliberate small misalignment of a single wheel can be contemplated for “steering” the trolley, that is, for introducing a bias to counteract forces which may tend to rotate the trolley about the pipe axis. This is addressed further in Chapter 7.

Chapter 9

[002-08] Metrology

Principal risks:

That there may not exist a cost-effective solution that meets the requirements on the frequency stability and maximum permissible diffraction losses of the metrology laser.

That it may be difficult for the metrology beam to be suitably expanded prior to propagation and for the opto-mechanical stability requirements of the beam expansion system to be met in a cost-effective manner.

9.1 Aim

To find a cost-effective solution that meets the requirements on the frequency stability and maximum permissible diffraction losses of the metrology laser.

To determine whether the metrology beam can be suitably expanded prior to propagation and whether the opto-mechanical stability requitements of the beam expansion system can be met in a cost-effective manner.

9.2 Method

This experiment was conducted in the following stages:

1. Diffraction calculations were performed to assess power and fringe visibility losses in different diameter metrology beams after propagation through the delay line system.
2. Calculations were performed to assess the tilt and shear stability required to guarantee successful operation of the metrology system. These were compared these with expected performance of potential stages and mounts.
3. The frequency stability criteria needed on timescales from 1-100ms for the metrology laser were calculated. The frequency stability of an in-house Zygo laser head was then evaluated by beating the beam against the beam from an iodine-stabilized laser (this work was contracted out to National Physical Laboratories). The measured frequency stability was then compared with the requirements.

9.2.1 Laser stability

The metrology system measures distance in terms of the laser wavelength, so variation of the MROI metrology laser frequency will cause corresponding errors in optical delay measurement. If this measurement is used in a servo loop to control the optical delay, then laser frequency jitter will transform into optical pathlength jitter. The current specification for the pathlength jitter over a 400m pathlength is 15nm rms over a 10ms interval, 41nm over 35ms and 55nm over 50ms. This corresponds to laser frequency stabilities of 3.75×10^{-11}, 1.0×10^{-10} and 1.37×10^{-10} respectively on these timescales.

Discussion with manufacturers of metrology lasers led us to believe that Zygo lasers might be sufficiently stable, but Zygo was unable to provide data on short-term stability. However, as the COAST group owns a Zygo laser it was possible for us to do this test ourselves. It was originally planned to beat the beam against that of a similar laser on a high speed photodiode in our laboratory. However, after a lengthy search a similar laser could not be procured and it was decided to contract the work out to National Physical Laboratories, who have a laser testing and calibration service which beats lasers against an iodine stabilised reference and can produce Allan deviation measurements for the timescales of interest. NPL's system has a claimed frequency stability noise floor of 1.5×10^{-11}.

9.3 Definition of Success

Success is achieved if a suitable solution in terms of diffraction and mechanical stability can be found for the metrology beam expansion, and if a cost-effective metrology laser can also be found that is sufficiently stable.

9.4 Results

9.4.1 Metrology power error budget

We assume that the metrology is accomplished using a Zygo ZMI7702 laser head and associated fringe detection systems. The laser head emits 425μW of power and the fringe detection systems require a fringe signal equivalent to 10μW of power at the nomimal working fringe contrast. Assuming that one laser is used for every 6 delay lines, and we assume a total optical system throughput of 50%, we have at total power of 35μW per delay line. The total losses due to diffraction and misalignment can therefore be a factor of no more than 3.5 in effective power loss.

9.4.2 Diffraction calculations

The schematic optical setup to be used for the metrology system is shown in figure 9.1 where the nominally 6mm diameter metrology beam from the Zygo is expanded before being injected into the delay line and is recontracted to 6mm after propagation through the delay line.

We assume here a Gaussian-profile metrology laser beam at wavelength $\lambda = 632.8$nm. The profile of the beam *amplitude* is given by

$$A(r,z) = A(z)\exp(-r^2/\rho(z)^2)$$

where r is the transverse radial distance from the optical axis and $\rho(z)$ is the radius to the $1/e$ contour of the beam at a distance z along the propagation direction. Note that the beam intensity is proportional

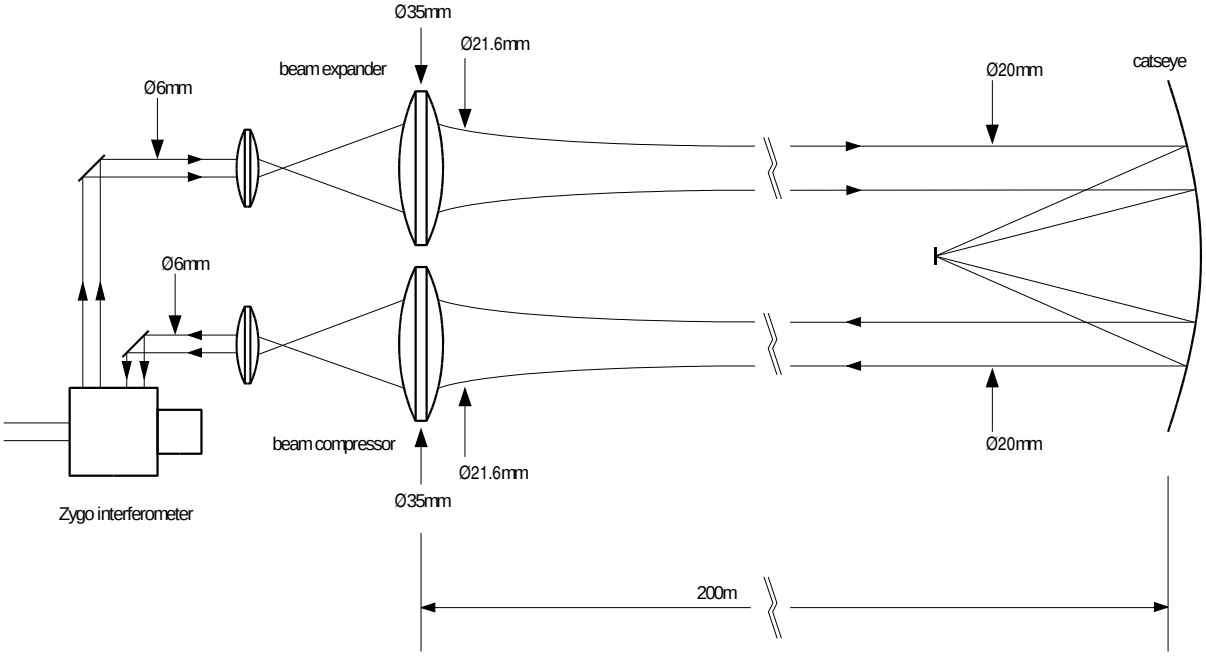

Figure 9.1: Schematic layout of the optical metrology using the Zygo laser metrology system showing the beam expansion and compression.

to the square of the amplitude, so that $\rho(z)$ is the radius of the $1/e^2$ intensity contour. By convention we call $d(z) = 2\rho(z)$ the beam diameter.

A Gaussian beam propagating over an infinite distance in free space will always have a waist where the beam diameter is minimised and there is zero wavefront curvature. We choose the zero of the z axis to be at this point, so that the beam waist diameter is $d(0)$. To minimise beam spreading for a fixed-focus beam expander, we choose the focus of the beam expander so that the beam waist is at the delay-line catseye when the trolley is the maximum distance from the laser, i.e. 200m away. The value for $d(0)$ which minimises the maximum beam diameter over a propagation path of $\pm z_{\max}$ from the waist is then given by $d_{\mathrm{opt}}(0) = 2\sqrt{\frac{\lambda z_{\max}}{\pi}}$ which has a value of 12.6mm for $z_{\max} = 200$m. However, making the beam larger than this will reduce the beam divergence due to diffraction and increase the tolerance for beam shear and so we choose instead a beam waist diameter of $d(0) = 20$mm. The maximum beam diameter is given by

$$d(z_{\max}) = d(0)\sqrt{1 + \left(\frac{\lambda z_{\max}}{\pi\rho(0)^2}\right)^2}$$

which evaluates to 21.6mm in this case.

The beam intensity profile is given by

$$I(r) = I_0 \exp(-2r^2/\rho^2)$$

and so the fraction of the total power accepted by a circular optic of diameter D is given by

$$\frac{\int_0^{D/2} I(r) 2\pi r\, dr}{\int_0^{\infty} I(r) 2\pi r\, dr} = 1 - \exp(-D^2/2\rho^2)$$

Subsituting the worst-case value of $\rho = 21.6$mm we find that if the clear aperture of the optics is 33mm, then 99% of the light in the Gaussian beam is captured, i.e. only 1% of the light has the potential to be scattered into the stellar beam. We have chosen a clear aperture of 35mm everywhere.

The losses in the metrology signal due to beam spreading are twofold: first there is a reduction in the amplitude matching of the interfering beams because one beam is spread over a larger or smaller area than the other, and secondly there is a loss in contrast due to the mismatch in the radii of curvature of the interfering beams. By choosing the focus of the beam reducing telescope appropriately, we can arrange for the worst mismatch of beam intensity to occur when the beam curvatures are perfectly matched, and vice versa. In any case the magnitude of these effects are both of less than or of the order of the fractional diameter mismatch i.e about 7% or less. Thus the beam diameter and curvature change effects are tolerable.

9.4.3 Shear stability calculation

If the shear of the metrology beam varies as the trolley moves along the delay line, or due to drifts in the beam launch optics, this will cause the overlap of the return beam with the metrology reference beam to vary. For two Gaussian beams of radius ρ the fractional change in the strength of the interference signal for a differential shear of δ is given by $\exp(-\delta^2/2\rho^2)$ so for $\delta = 5$mm and $\rho = 10$mm we get a change in the interference signal by a factor of 0.88.

Thus when the beam shear is equal to the maximum variation expected due to imperfection in the pipes, the metrology signal loss due to misalignment is well within the power budget. Thus even with the beam shear correction servo switched off, the metrology will not lose lock.

The drift in the beam launch direction which would cause 5mm of misalignment is equal to 5mm/400m, i.e. 12.5μrad. This is a much less tight drift tolerance than most of the rest of the optics in the array, and so should be easily achieved.

9.4.4 Metrology error due to shear correction servo

In order to reduce the possibility of metrology laser light leaking into the astronomical beam, we plan to introduce wedges on the front of the catseye as shown in figure 9.2 (this idea was used on the PTI delay lines). These deviate the metrology beam so that it lands on the catseye secondary mirror at a different point from the starlight beam. Thus any light scattered from the metrology beam appears, when seen from the starlight beam combiners, to come from a different direction than the starlight and therefore can be removed by spatial filtering.

However, as shown in the figure, this also means that when the secondary mirror is tilted to compensate for shear errors, the optical pathlength travelled by the metrology beam and the starlight will differ. If the focal spots of the metrology light and starlight are separated by a distance d, then a mirror tilt of θ will cause the metrology beam to travel an extra distance of approximately $z = 2d\theta$. What is most important is the change in this differential pathlength with time, and since d is approximately fixed, then changes in θ are important.

For a primary mirror with focal length f then to correct an optical shear variation of y requires a mirror motion of $\theta = y/2f$. Thus we have $z = yd/f$. We will normally choose the focal spot from the metrology beam to be many spot diameters from the starlight beam. For a metrology beam with diameter D, the focal spot diameter will be approximately $2f\lambda/D$. We choose to put the spot 10 spot diameters away from the starlight, so $d = 20f\lambda/D$. Combining these we get $z = 20\lambda y/D$, and substituting $\lambda = 632.8$nm, $y = 5$mm, and $D = 20$mm we get $z = 3.1\mu$m. We note that this is small in comparison to the allowed defocus error for the catseye and so differential defocus between the metrology and the starlight is not a concern.

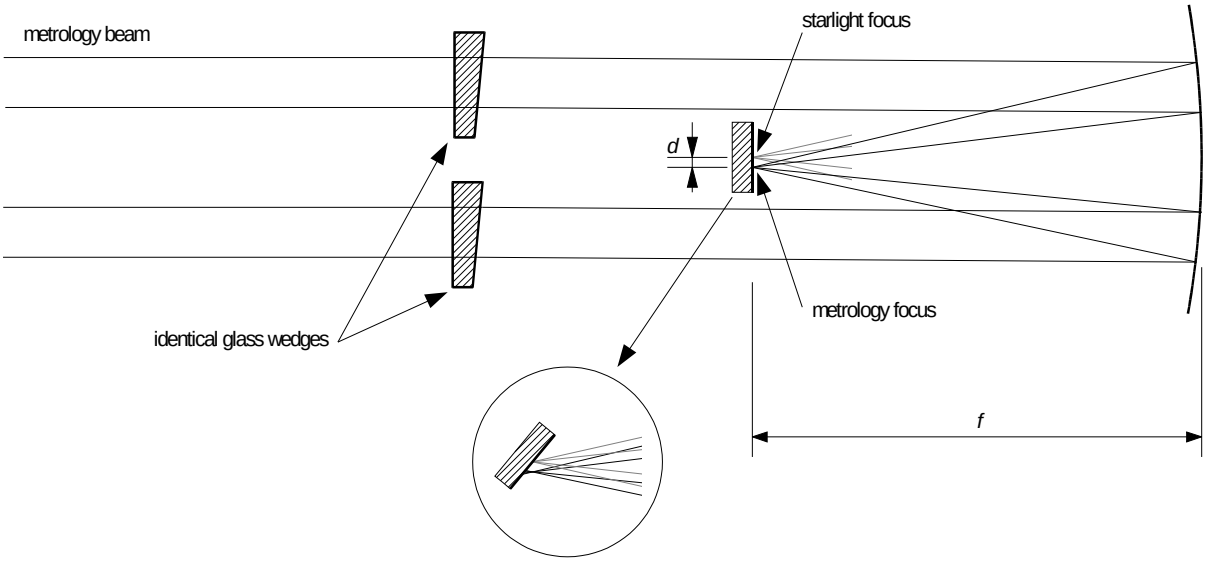

Figure 9.2: Schematic optical diagram showing the use of optical wedges to displace the metrology beam on the catseye secondary with respect to the starlight. The inset diagram shows the effect of secondary mirror tilt on the differential pathlength between starlight and the metrology beam.

The above change in differential optical path is much larger than the allowable fringe jitter on short timescales, but the stated level mirror motion will generally occur on much longer timescales than are of concern for fringe jitter. The maximum rate of change of the shear correction is of order 5mm/m of pipe. With the trolley moving at its maximum tracking speed of 15mm/sec, this translates to $dy/dt = 75\mu$m/s i.e. $dz/dt = 47$nm/sec, which is well within the allowed range (15nm over 10msec, 55nm over 50msec).

9.4.5 Laser stability

The results from National Physical Laboratories are plotted in Figure 9.3. NPL describes the results between 10ms and 100ms as being "variable" and provides both best and worst readings for those timescales. They ascribe the problem to suspected "mains-locked frequency modulation" in their test laser but think that the "best" results are probably also the most representative.

9.5 Discussion

The calculations indicate that providing the correct amount of beam expansion is used, diffraction is not a problem and the effects of shear errors of the metrology beam are easily kept within an acceptable range. The differential path errors due to the combined effects of the deliberately-introduced metrology beam angular offset and dynamic shear correction using the catseye secondary are small, but the calculation does indicate that any shear correction system should be smooth.

The results from the laser testing are ambiguous due to the uncertainty in measurement from 10 to 100ms. If the "best" results in this range are representative then the Zygo 7702 meets the requirement and is certainly a feasible solution, although the laser is marginal at 10ms. This may be mitigated if the closed-loop bandwidth of the feedback loop using the metrology signal is less than about 100Hz, since laser frequency jitter at higher frequencies will then not feed through to jitter in the delay line. If the "worst" results are more typical then the 7702 does not meet the requirements and it will be necessary to look elsewhere for our metrology needs.

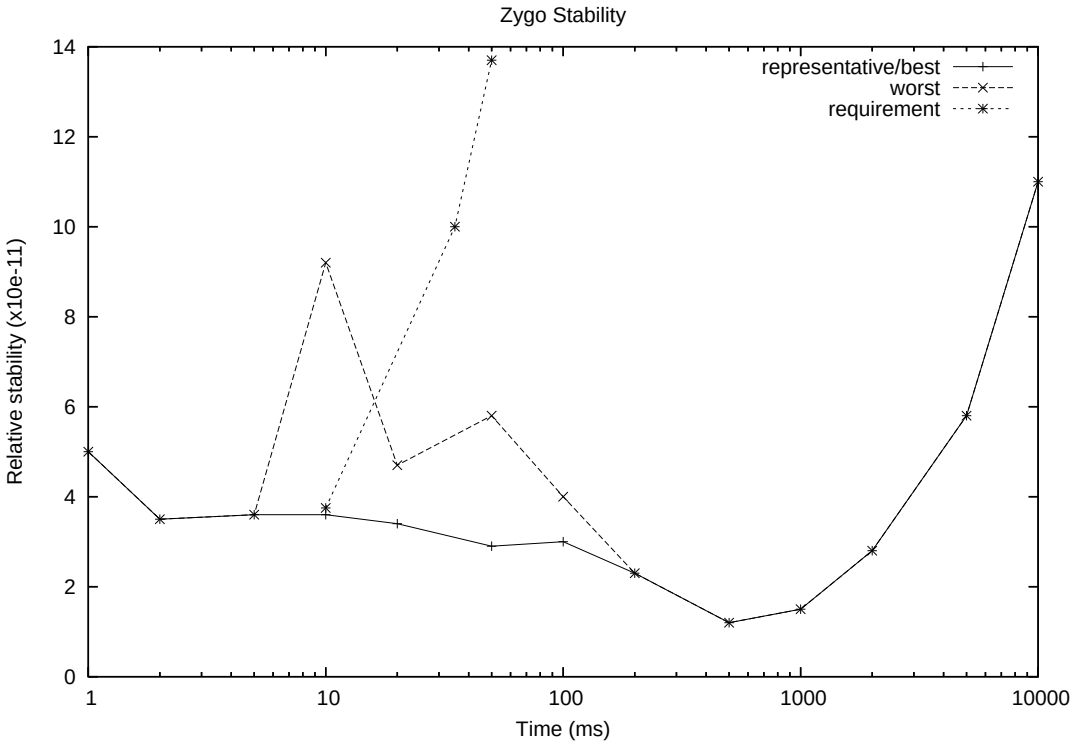

Figure 9.3: Allan deviation measurements for the Zygo laser. Measurements were variable in the range 10–100ms, for which the best and worst case measurements are plotted. The stability requirement for the MROI is also shown.

9.5.1 Fallback Options

The laser tested by NPL was a Zygo 7702. If this model proves to be inadequate, Zygo manufactures another lasers with improved specifications (the 7712), although it is unclear if the short-term stability of these products is also improved, so such lasers would also have to be tested.

If such a laser also falls short of our requirements, we have sourced a manufacturer of green Nd-Yag frequency doubled NPRO lasers who claims a stability of 1kHz over a 100ms interval, or 2×10^{-12}. This comfortably exceeds our stability requirements. However, the use of such a laser at MROI would require custom design of the entire metrology system, whereas all parts for the Zygo equivalent can be bought “off the shelf”.

Chapter 10

Conclusions

The results from the analyses and experiments can be summarised briefly by saying that, in general, the experiments confirmed the low-risk nature of the proposed delay line concept. In some cases, the experiments did not result in the requirements for the final design being met by the apparatus available at the current stage of development, but in all cases the experiments demonstrated that the risks associated with meeting the requirements would be both low and manageable.

Below we summarise the conclusions that can be drawn from the experiments, specifically with respect to any changes that might need to be made to the design, the potential programmatic impact of such changes, and any possible future tests that it might be advantageous to make.

Pipe coupling scheme The coupling design involving the use of dowels to align the pipe ends was problem-free, and allowed the trolley tracks to be aligned to a level of accuracy such that no discernible "bump" was seen in accelerometer measurments when going over the join at tracking speed. Millimetre-sized gaps between pipes were found to be acceptable, and this means that the squareness requirements of the pipe are substantially reduced compared to a scheme involving flanges. A limited amount of "production engineering" aimed at making sure that the demonstrated dowel-hole drilling accuracy can be reliably reproduced on all the pipe joints would help to avoid pipe wastage.

The vacuum integrity of the test rig demonstrates that there are no substantial problems in achieving a joint which is both flexible (to remove error build-up from pipe to pipe) and acceptably vacuum-tight. The currently measured leak rates are marginal with respect to maintaining the required vaccuum overnight without pumping, but it should be noted that the stated requirements have a substantial engineering margin of safety already built in, and also that the current experiments have been performed with little preparation of the pipe surface or vacuum grease in the seals. Further work is required to determine the major contributing factors to the current leak rate, but in the worst case this will mean that additional finishing of the pipe ends would be needed to allow more infrequent pumping of the vacuum system. As a worst-case estimate, the cost impact of this extra finishing would be at most \$500 per joint, i.e. a total of \$75k for 6×100m pipes (assuming 4m pipe lengths), in comparison to an originally estimated cost for the pipe, joints, and supports (excluding installation) of \$435k.

Pipe supports The current design incorporating steel flexure legs with cradles for the pipes have been shown to be easy to set up and to allow straightforward installation of the pipes. The finite-element model for the support system was validated and predicts that extrapolation of the pipe and support system to 200m length should pose no particular problems with undamped resonances.

The support system as designed fits easily into the allowable space envelope, but there is scope for re-engineering of the design to allow manufacture and installation costs to be minimised.

Carriage trajectory Direct tests of a trolley with a retroreflector showed that the samples of pipe purchased "off-the-shelf" met all the straightness requirements consistent with an active shear-control system. The straightness parameter which was most stringent, that for trolley pitch and yaw, still had a 50% margin of safety in the worst case. Since these pipes were not specially selected or handled, this indicates that it is unlikely that a bulk order of standard aluminium pipes will require significant amounts of selection or processing (apart from cleaning to remove grease etc) to be acceptable for use in the delay lines. A better idea of the amount of pipe selection (if any) that might be needed may be derived by talking in detail with pipe manufacturers about the uniformity of their manufacturing processes.

The scheme used to measure the pipes showed that optical measurement of the beam shear using a laser is straightforward, and this can serve as a prototype for the sensor in the shear-correction servo.

Control and communication The use of RF communications inside cylindrical conducting pipes was never a high-risk item, but the risk that there might be nulls in the radiation pattern due to reflections in the pipe which could not be controlled by standard waveguide techniques was demonstrated to be low. The noise performance of the initial analogue RF transceiver was shown to be not adequate for communicating the voice-coil drive signal, but many off-the-shelf alternatives exist, including digital links or higher-quality FM links. In the worst case, there may be some increased engineering cost associated with adopting a less off-the-shelf commercial solution for this link, perhaps commissioning an RF design firm to adapt an existing transceiver design to our needs. An estimated upper limit to this cost approximately $50k, but we judge the probability of needing this fallback as being very low.

Power transmission A simple inductive power transmission system was shown to be superior in terms of friction performance to conventional dragged-cable solutions, providing adequate power and power stability such that it had no discernible effect on the performance of the COAST trolley when compared with a wired supply. The mechanical effects of the inductive scheme scale to 200m of travel much more favourably than dragged-cable solutions, and extrapolation of the electrical performance to this length of travel was shown to present no serious obstacles.

Trolley steering Tests with a trolley with a low centre of gravity show that it was self-correcting with respect to "clocking". Should a higher-centre-of-gravity design be adopted, the tests show that any forces tending to make the trolley clock only have a discernible effect over many trolley lengths of travel, and therefore designing a low-bandwidth servo to achieve adequate stability should present few problems. Simple actuation schemes for such a servo, either by steering one wheel or by shifting a weight, were shown to be feasible and have no discernible impact on the level of trolley vibration and hence pose no risk of additional OPD jitter.

OPD disturbance tests The use of compliant wheels was shown to give the expected isolation from vibrations of the pipe and support. More importantly, the use of compliant wheels gave a lower level of trolley vibration when running on the unfinished inner surface of the test rig pipes than seen on the COAST trolley when running on polished steel rails. A preliminary model of the disturbance rejection of the MROI catseye servo, validated using the COAST trolley, shows that all the OPD stability requirements can be met with more than adequate margins.

Metrology Analyses showed that with a suitably expanded metrology laser beam, there is little risk of loss of the metrology signal due to diffraction or alignment drifts, and that even without an active beam shear correction system, the level of beam shear arising from non-straightness of

pipes would not cause metrology signal loss. The wavelength stability of a commercial Zygo laser was shown to be adequate for correction over a full 200m path, although it may be worth doing stability tests on a more expensive Zygo laser to see if greater performance margins are available on the shortest timescales.

In most cases the results of the experiments met expectations, and any surprises that occurred during the performance of the experiments were almost entirely positive. For example, the test trolley running on compliant wheels on an unfinished pipe surface exhibited generally lower vibrations than the COAST trolley running on polished rails, the trolley turned out to be remarkably resistant to attempts to make it “clock” inside the circular pipe, and little increase in vibration levels was seen when the trolley wheels rolled over gaps of many millimetres between the pipes.

In conclusion it can be said that that any remaining technical risks in the design have been demonstrated to be manageable, and the programmatic impact of any changes in the concept that may be needed as the design progresses are likely to be small.